NON-GPS NAVIGATION USING VISION-AIDING
AND
ACTIVE RADIO RANGE MEASUREMENTS

THESIS

Erich Lichtfuss, Second Lieutenant, USAF

AFIT/GE/ENG/11-23

DEPARTMENT OF THE AIR FORCE
AIR UNIVERSITY

AIR FORCE INSTITUTE OF TECHNOLOGY

Wright-Patterson Air Force Base, Ohio

AFIT/GE/ENG/11-23

Non-GPS Navigation Using Vision-Aiding
and
Active Radio Range Measurements

THESIS

Presented to the Faculty

Department of Electrical and Computer Engineering

Graduate School of Engineering and Management

Air Force Institute of Technology

Air University

Air Education and Training Command

In Partial Fulfillment of the Requirements for the

Degree of Master of Science in Electrical Engineering
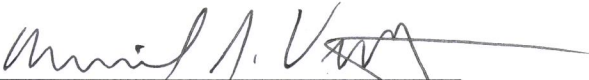
Erich Lichtfuss, B.S.E.E.
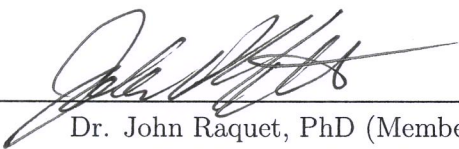
Second Lieutenant, USAF

March 2011

AFIT/GE/ENG/11-23

NON-GPS NAVIGATION USING VISION-AIDING
AND
ACTIVE RADIO RANGE MEASUREMENTS

Erich Lichtfuss, B.S.E.E.
Second Lieutenant, USAF

Approved:

_____   ___3 MAR 11_____
Lt Col Michael Veth, PhD (Chairman)   date

_____   ___9 Mar 2011_____
Maj Kenneth Fisher, PhD (Member)   date

_____   ___9 MAR 11_____
Dr. John Raquet, PhD (Member)   date

AFIT/GE/ENG/11-23

Abstract

The military depends on the Global Positioning System (GPS) for a wide array of advanced weaponry guidance and precision navigation systems. Increased numbers of military operations are conducted in GPS degraded or denied environments (e.g., urban canyons or inside buildings). Lack of GPS access makes precision navigation in these environments very difficult. Inclusion of inertial sensors in existing navigation systems provides short-term precision navigation during periods where GPS cannot be used, but drifts significantly over long-term navigation. Development of the navigation system presented in this thesis is motivated by the need for inertial sensor drift-constraint for precision navigation in degraded and denied GPS environments. The navigation system developed in this thesis consists of inertial sensors, a simulated barometer, three Raytheon DH500 radios, and a stereo-camera image-aiding system. The Raytheon DH500 is a combat communication radio which also provides range measurements between radios within the local radio network. The measurements from each sensor are fused together with an extended Kalman filter to estimate the navigation trajectory. Residual monitoring and the Sage-Husa adaptive algorithm are individually tested in the Kalman filter range update algorithm to help improve the radio range positioning performance. The navigation system in this thesis is shown to provide long-term inertial sensor drift-constraint with position errors as low as 3 meters.

Acknowledgements

First, I acknowledge Jesus my Savior for prompting me to come here to get my masters and then giving me the strength and motivation to complete this work. You are my Rock.

Next, I'd like to thank my advisor for challenging me and giving me the opportunity to do my best.

I would also like to thank the good friends I made at AFIT for slugging through this thesis program alongside me. Their humor kept me sane and proof-reading skills really helped to refine what you read today. I also really appreciate the work of the ANT Center staff for all the software and hardware building and long hours of debugging that was necessary to get good data for my thesis.

Last, but by no means least, I would like to thank my whole family back home for their unwaivering support through this entire time. I'm finally done with school! (for now)

Erich Lichtfuss

Table of Contents

List of Figures

List of Tables

List of Abbreviations

Non-GPS Navigation Using Vision-Aiding

and

Active Radio Range Measurements

I. Introduction

This thesis presents a research effort focused on the fusion of radio range measurements with inertial and image data to provide precision navigation without the use of the global positioning system (GPS). This research effort is motivated by the requirement for precision navigation in environments where GPS is degraded or denied. Urban and indoor environments are examples of places where GPS signals are degraded or denied.

The military depends on GPS for a wide array of advanced weaponry guidance and navigation systems. General Schwartz characterized this GPS dependence in a 2010 keynote speech as an "exploitable vulnerability." [23] Increasing numbers of military operations are being conducted in so-called urban canyons where the surrounding building structures block direct view of the GPS satellites. The tall structures generate RF interference, obscuring line-of-sight view to the GPS satellites. This severely degrades the GPS navigation capability.

General Schwartz stated that our military force must "reduce its dependence on GPS-aided precision navigation and timing." He then directed research efforts to explore new technologies which will provide "less vulnerable, yet equally precise" navigation capabilities. These navigation capabilities must enable our forces "to operate in GPS-denied environments" during future operations.

1.1   Current Technology

GPS-aided inertial navigation, indoor radio navigation systems, and image-aided navigation systems are three examples of current navigation technologies. For

the GPS-aided inertial navigation system, the GPS provides long-term position stability and the inertial sensors provide short-term position precision [20]. When GPS access is denied, the inertial position solution drifts significantly providing an unusable navigation solution.

The lack of indoor access to GPS is addressed in the commercial community by development of radio navigation systems [10]. These systems consist of radio nodes placed at known locations throughout the building. Indoor navigation is then based on proximity to each of the radio nodes. The indoor radio-based positioning system provides GPS-like position capability, but requires prior knowledge of the building and prior placement of the radio nodes. Unfortunately, this is not practical in a combat environment.

Navigation without GPS in an unknown environment is addressed by stereo-camera image-aiding which is used to constrain inertial sensor drift. Such an image-aided navigation system is developed by Veth [26] and is shown to provide very good indoor navigation without prior environment knowledge. However, this method drifts unconstrained when the camera system is unable to find enough good image features to track.

1.2 Proposed Solution

The proposed radio-range aided navigation system addresses the issues of inertial navigation position drift with minimal radio infrastructure. The navigation system is composed of an inertial navigation system, a simulated barometer to constraint vertical navigation drift, the Raytheon DH500 radio range system, and the stereo-camera image-aiding system developed by Veth [26]. Three DH500 radios are provided for this thesis. Two radios are positioned at known positions which simulate potential radio base stations on troop transport vehicles. The third radio is located with the inertial sensors and camera system which would be carried by the individual soldier or on a mobile platform.

To test the navigation system, the sensor measurements are combined using an extended Kalman filter, presented in Section 2.3.2. Using measurement updates from each sensor, the Kalman filter estimates the position, velocity, and attitude of the navigation system. Additional algorithms including residual monitoring, presented in Section 2.9.1, and the Sage-Husa adaptive algorithm, presented in Section 2.9.2, are used to refine the Kalman filter's usage of the radio range measurements. Coupling these sensors together provides a better navigation solution.

1.3   Organization

The remainder of this thesis is organized as follows. Chapter II covers background topics integral to understanding the navigation system implemented in this thesis. Topics include coordinate frames, sensor fusion, radio positioning methods, and adaptive filter techniques. The methods used to implement and test the navigation system are presented in Chapter III with results detailed and analyzed in Chapter IV. Chapter V concludes this thesis with final remarks and suggestions for future areas of exploration.

II. Background

The background chapter presents the mathematical and technical foundation necessary for proper implementation of the radio aided navigation system. The chapter begins with the definition of the mathematical notation used in this document. Next, common coordinate systems and transformation methods are covered. Presentation follows of the sensors, mechanization, and errors of the inertial navigation system. Next, evaluation of related work in radio positioning methods with common techniques to compute position are presented. Errors due to RF multipath are presented along with algorithms to estimate and mitigate multipath effects. Next, baro-altitude aiding addresses the lack of vertical navigation channel observability present with radio navigation. The Chi Squared statistic aids in evaluation of range data errors against the Gaussian probability density function. The chapter concludes with adaptive filtering algorithms to improve the radio range modeling.

2.1 Notation

The mathematical notation used throughout this thesis is presented in this section. The notation provided in [26] provides guidance for the following definitions.

- **Scalar** quantities are represented with lower or upper case italic symbols. Examples include scale factors such as A and d.

- **Vector** quantities are represented with lower case boldface italic symbols. Examples include the state vector $\boldsymbol{x}$ and measurement vector $\boldsymbol{z}$.

- **Matrix** quantities are represented with upper case boldface italic symbols. Examples include the state transition matrix $\boldsymbol{\Phi}$ and measurement matrix $\boldsymbol{H}$.

- **Estimated variables** are represented with a hat accent. Examples include the estimate of the state vector $\hat{\boldsymbol{x}}$ and estimate of the measurement vector $\hat{\boldsymbol{z}}$.

- **Variables with error** are represented with a tilde accent. Examples include the slant range measurement from ranging radios $\tilde{r}$.

4

- **Direction cosine matrices** provide rotation between coordinate frames denoted by $\boldsymbol{C}_a^b$. The subscript indicates the source frame and the superscript indicates the destination frame.

2.2 Coordinate Systems and Transformations

Navigation is performed relative to a frame of reference. The frame of reference is dependent on the environment where the navigation is performed. The Earth's surface, the streets of a city, and the interior of a building present examples of environments where the significance of a navigation solution is defined relative to the present environment. Knowledge of the position and orientation of sensors mounted on a vehicle enable the sensor data to correctly aid the navigation solution.

The coordinate systems and transformations presented in this section provide a framework to define the position and orientation of the navigation state and associated sensors relative to the applicable environment. This section continues with presentation of the World Geodic System 1984 specification, detailed definitions for common reference frames, and coordinate system transformations.

2.2.1 World Geodic System 1984.

The World Geodic System 1984 specification (WGS84) is a worldwide reference frame which enables precise quantification of locations on the Earth [1]. The WGS84 specification represents the result of ongoing efforts by the National Geospatial-Intelligence Agency (NGA) to further refine and detail the surface of the Earth. WGS84 is a three-dimensional right-handed coordinate system as shown in Figure 2.1. The x-axis passes through the International Earth Rotation Service (IERS) Reference Meridian (IRM) which is analogous to the Greenwich meridian. The z-axis passes through the IERS Reference Pole (IRP) with is analogous to the north pole. The y-axis is orthogonal to both the x and z axes.

2.2.2 Coordinate Systems.

Coordinate systems provide a structure to characterize the location and orientation of a vehicle and sensors in space. This enables
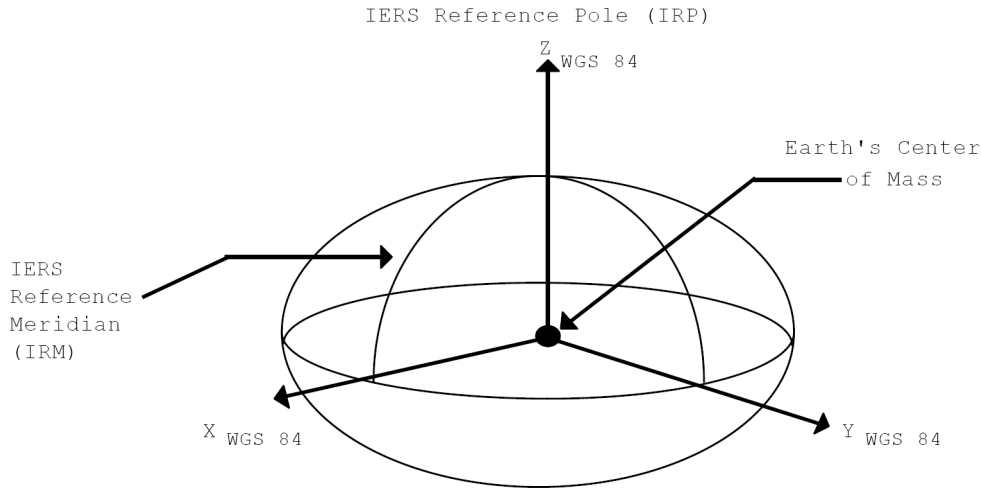
Figure 2.1:   WGS84 Coordinate System Definition. The three-axis, orthogonal coordinate system aligns the z-axis with the north pole and the x-axis with the Greenwich meridian [1].

changes in the position and orientation of a vehicle to be quantified and understood. A bulleted list follows with formal coordinate frame definitions [25, 26].

- Inertial Frame (I-frame): The I-frame is a three-axis, right-handed coordinate system with no predefined origin or orientation. The inertial frame is a theoretical reference frame which does not accelerate or rotate. Newton's laws apply in this reference frame.

- Earth-Centered Frame (i-frame): The Earth-centered frame is a three-axis right-handed coordinate system with the origin located at the center of the Earth's mass. The x and y axes lay on the equator and do not rotate relative to the *fixed* stars. The i-frame is not a true inertial frame since it accelerates through space with the Earth. However, for navigation applications on the surface of the Earth it can be considered an inertial reference frame. Figure 2.2 presents the i-frame with axes labeled O_{xi}, O_{yi}, and O_{zi}.

- Earth-Centered Earth-Fixed Frame (e-frame): The Earth-centered Earth-fixed frame is a three-axis right-handed coordinate system with the frame origin located at the center of the Earth's mass. The e-frame does not rotate relative

to the Earth with the x-axis aligned with the intersection of the Greenwich meridian and the equator. The z-axis points out the north pole. The y-axis points out from the equator 90 degrees east longitude. The e-frame is a Cartesian coordinate system. This characteristic allows for simplification of certain navigation calculations. Figure 2.2 presents the e-frame origin at O with axes labeled O_{xe}, O_{ye}, and O_{ze}.

- Vehicle-Fixed Local-Level Navigation Frame (n'-frame): The vehicle-fixed local-level navigation frame is a three-axis right-handed coordinate system with the origin defined relative to the vehicle. The x, y, and z axes are defined to point towards north, east, and down (NED), respectively. The down direction is defined to align with the the local gravity vector. The vehicle-fixed navigation frame is differentiated from the Earth-fixed navigation frame by the rotation of the vehicle-fixed frame relative to the Earth's surface as defined by the rotation rate $\boldsymbol{\omega}_{en'}^{n'}$. This rotation is discussed further in Section 2.4.2.

- Earth-Fixed Local-Level Navigation Frame (n-frame): The Earth-fixed local-level navigation frame is a three-axis right-handed coordinate system with the origin defined relative to the Earth. In general the n-frame origin is defined on the surface of the Earth. The x, y, and z axes are defined to point towards north, east, and down (NED), respectively. The down direction is defined to align with the local gravity vector. The n-frame provides simplified navigation trajectories on the surface of the Earth within a local area. The n-frame is not suited to long-distance navigation. Figure 2.2 presents the n-frame origin at P with axes labeled N, E, and D.

- Vehicle Body Frame (b-frame): The vehicle body frame is a three-axis right-handed coordinate system fixed to the vehicle. The origin is defined at a predetermined location on the vehicle. The origin typically coincides with the center of the on-board navigation sensor suite. The x and y axes project out the front and right side of the vehicle as viewed from the top. The z-axis projects out

7
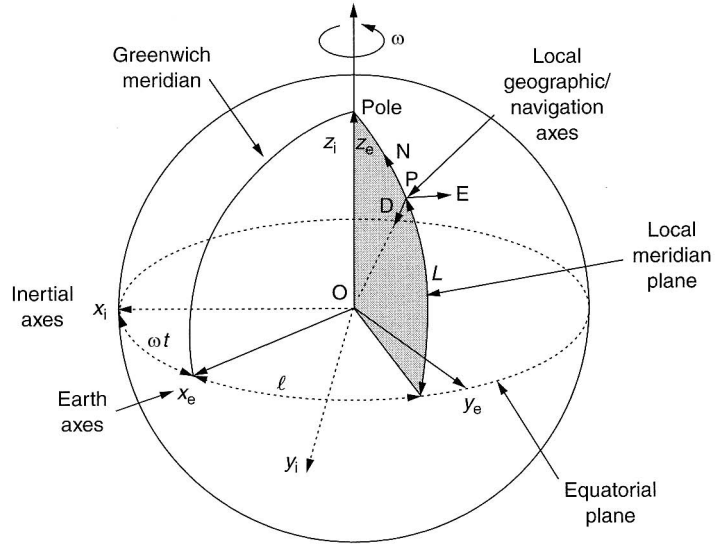
Figure 2.2:   Common Frames of Reference. Depicts Inertial, Earth, Navigation, and Body reference frames [25].

the bottom of the vehicle. Changes in the orientation of the vehicle b-frame are defined as roll, pitch, and yaw.

- Sensor Frame (s-frame): The sensor frame is a three-axis right-handed coordinate system defined for each sensor of the navigation system. The origin of an individual s-frame is defined relative to each sensor. For the purposes of this thesis, the various s-frame locations and orientations are defined relative to the b-frame. The orientation of the s-frame x, y, and z axes is unique to each sensor.

2.2.3 Coordinate System Transformations.   As mentioned previously, navigations systems are comprised of multiple sensors. In order to use information from the sensors, the orientation of the sensor relative to the vehicle body frame must be known. This orientation consists of the roll, pitch, and yaw rotations required to align the sensor's coordinate frame with the vehicle body frame. For example, the camera sensor views the environment from the perspective defined by its orientation. Definition of this orientation relative to the vehicle body coordinate systems allows the navigation system to correctly interpret the data from the camera for inclusion

into the navigation solution. This section continues with presentation of properties of direction cosine matrices (DCMs) and then Euler angles.

The DCM defines a three-dimensional matrix rotation between two coordinate frames. A vector $\boldsymbol{v}_i$ pre-multiplied by a DCM is transformed from its initial coordinate frame to the final coordinate frame as shown in Equation (2.1).

$$\boldsymbol{v}_f = \boldsymbol{C}_i^f \boldsymbol{v}_i \tag{2.1}$$

Several DCMs may be pre-multiplied together to obtain a single DCM to performs the series of rotations in a single operation. Equation (2.2) presents a series of rotations to transform a vector in the e-frame $\boldsymbol{v}_e$ into the s-frame $\boldsymbol{v}_s$ which requires passing through the n and b-frames.

$$\boldsymbol{v}_s = \boldsymbol{C}_e^s \boldsymbol{v}_e = \boldsymbol{C}_b^s \boldsymbol{C}_n^b \boldsymbol{C}_e^n \boldsymbol{v}_e \tag{2.2}$$

DCMs have two important characteristics which are presented in the following equations. The determinant of a DCM is always one

$$\mathrm{Det}(\boldsymbol{C}_e^s) \equiv |\boldsymbol{C}_e^s| = 1 \tag{2.3}$$

To reverse a DCM transformation, take the transpose or inverse of the matrix

$$\boldsymbol{C}_a^b = (\boldsymbol{C}_a^b)^{-1} = (\boldsymbol{C}_a^b)^T \tag{2.4}$$

Euler angles define three rotations about orthogonal axes. These rotations relate the orientation of a source coordinate frame to the destination coordinate frame. These angles must be applied in a specific order to ensure correct final coordinate frame rotation is achieved. First, yaw rotation is performed about the z-axis, then pitch rotation about the the y-axis, and finally roll rotation about the x-axis. This

strict order of rotation ensures the correct final orientation of the source coordinate frame. The yaw rotation about the z-axis is measured by ψ, pitch rotation about the y-axis is measured by θ, and then roll rotation about the x-axis is measured by ϕ. The next paragraph presents the conversion from Euler angles to the DCM format.

The three rotations presented above for Euler angles may be translated into a single DCM. Conversion from Euler angles to a single DCM starts with creation of one DCM for each Euler angle rotation. Each DCM rotates the coordinate frame by the corresponding angle. The source orientation of the coordinate frame is defined as orientation 1. The subsequent rotations are defined as orientations 2, 3, and 4 where orientation 4 is the final coordinate frame orientation. A combination of subscripts and superscripts are used to indicate the order of transformations. Equations (2.5), (2.6), and (2.7) present the matrices that correspond to each of the three rotations.

$$\boldsymbol{C}_1^2 = \begin{bmatrix} cos\ \psi & sin\ \psi & 0 \\ -sin\ \psi & cos\ \psi & 0 \\ 0 & 0 & 1 \end{bmatrix} \tag{2.5}$$

$$\boldsymbol{C}_2^3 = \begin{bmatrix} cos\ \theta & 0 & -sin\ \theta \\ 0 & 1 & 0 \\ sin\ \theta & 0 & cos\ \theta \end{bmatrix} \tag{2.6}$$

$$\boldsymbol{C}_3^4 = \begin{bmatrix} 1 & 0 & 0 \\ 0 & cos\ \phi & sin\ \phi \\ 0 & -sin\ \phi & cos\ \phi \end{bmatrix} \tag{2.7}$$

Pre-multiplication of the three DCMs results in a single DCM which performs the same rotation in a single step as shown in Equation (2.8).

$$\boldsymbol{C}_1^4 = \boldsymbol{C}_3^4 \boldsymbol{C}_2^3 \boldsymbol{C}_1^2 \tag{2.8}$$

2.3   State Estimation and Sensor Fusion

The radio-aided navigation system developed in this thesis utilizes multiple sensors each with unique error models and data rates. Each sensor provides information about the current vehicle navigation states of position, velocity, and attitude. Sensors used in this thesis include: an inertial navigation system, a barometer, a camera system, and a radio range system. The inertial navigation system measures how the vehicle accelerates and changes attitude. The barometer measures air pressure which correlates with the current vehicle altitude. The camera system tracks landmarks in the visual environment which provide information on the change in position and attitude of the vehicle. Finally, the radio range system provides information about the position of the vehicle relative to each of the ground radio stations. The Kalman filter provides an estimation algorithm to estimate the true vehicle states and optimally fuse the information provided by each sensor.

In reality, the "true" vehicle navigation states cannot be known exactly, but they may be estimated. The Kalman filter uses statistical models of the vehicle's motion and sensors to estimate a statistically-optimal solution to the vehicles navigation states of position, velocity, and attitude. The vehicle model describes how the vehicle moves and responds to changes in motion. Each sensor model maps the particular sensor observations to the filter states. The sensor model also describes how the sensor corrupts or adds error to the "true" position, velocity, or attitude of the vehicle. This section first presents the linear Kalman filter and then the extended Kalman filter.

2.3.1   The Linear Kalman Filter.   The Kalman filter is composed of two classes of models and two separate algorithm steps [16]. The vehicle dynamics model and sensor models comprise the two model classes. The two algorithms consist of time propagation and measurement update steps. Time propagation occurs at regular intervals and the measurement update step occurs whenever a sensor provides a measurement. Specific time index notation used to indicate variables processed through the two algorithm steps is covered at the beginning of each algorithm section. The

11

next section presents the Kalman filter models followed by the time propagation and measurement update steps in separate sections.

2.3.1.1 Linear Models. The vehicle and sensor models provide the Kalman filter with prior knowledge of the vehicle dynamics and sensor properties [16]. The vehicle dynamics model is shown in Equation (2.9)

$$\hat{\boldsymbol{x}}(t_{i+1}) = \boldsymbol{\Phi}(t_{i+1}, t_i)\hat{\boldsymbol{x}}(t_i) + \boldsymbol{B}_d(t_i)\boldsymbol{u}(t_i) + \boldsymbol{G}_d(t_i)\boldsymbol{w}_d(t_i) \tag{2.9}$$

where $\hat{\boldsymbol{x}}(t_{i+1})$ is the new state estimate, $\boldsymbol{\Phi}(t_{i+1}, t_i)$ is the state transition matrix, $\hat{\boldsymbol{x}}(t_i)$ is the current state estimate, $\boldsymbol{B}_d(t_i)$ is the control input matrix, $\boldsymbol{u}(t_i)$ contains the control input vector, and $\boldsymbol{G}_d(t_i)$ is the noise matrix which applies each noise source defined in the vector $\boldsymbol{w}_d(t_i)$ to each of the filter states. The noise source vector describes the uncertainty of the vehicle dynamics model.

Each Kalman filter sensor model maps the sensor's observation to the filter states and describes the uncertainty of the model. Equation (2.10) presents the sensor model

$$\boldsymbol{z}(t_i) = \boldsymbol{H}(t_i)\hat{\boldsymbol{x}}(t_i) + \boldsymbol{v}(t_i) \tag{2.10}$$

where $\boldsymbol{z}(t_i)$ is the sensor measurement, $\boldsymbol{H}(t_i)$ is the measurement matrix mapping the sensor's observation to the filter states, $\hat{\boldsymbol{x}}(t_i)$ is the current state estimate, and $\boldsymbol{v}(t_i)$ is noise of sensor model. Similar to the vehicle model, the sensor noise describes the uncertainty of the sensor model. The vehicle dynamics model is used during time propagation which is presented in the next section.

2.3.1.2 Time Propagation. Time propagation moves the filter state estimate and filter uncertainty through time based on the vehicle dynamics model [16]. The time index t_i^+ is defined as immediately before time propagation and t_{i+1}^- is defined as immediately after time propagation. The linear Kalman filter state estimate is initialized with the starting navigation state of the vehicle, $\hat{\boldsymbol{x}}(t_0^+) = \boldsymbol{x}(t_0)$. The

filter covariance $\boldsymbol{P}(t_0^+)$, also known as the filter uncertainty, is initialized with the uncertainty of the vehicle's initial navigation state. This step is composed of two equations. Equation (2.11) presents the propagation of the filter state estimate

$$\hat{\boldsymbol{x}}(t_{i+1}^-) = \boldsymbol{\Phi}(t_{i+1}, t_i)\hat{\boldsymbol{x}}(t_i^+) + \boldsymbol{B}_d(t_i)\boldsymbol{u}(t_i) \tag{2.11}$$

where $\hat{\boldsymbol{x}}(t_{i+1}^-)$ is the new state estimate, $\boldsymbol{\Phi}(t_{i+1}, t_i)$ is the state transition matrix, $\hat{\boldsymbol{x}}(t_i^+)$ is the current state estimate, $\boldsymbol{B}_d(t_i)$ is the control input matrix, and $\boldsymbol{u}(t_i)$ is the control input vector. The state transition matrix $\boldsymbol{\Phi}(t_{i+1}, t_i)$ and control input matrix $\boldsymbol{B}_d(t_i)$ are defined in the vehicle dynamics model. The Equation (2.12) presents the propagation of the filter uncertainty

$$\boldsymbol{P}(t_{i+1}^-) = \boldsymbol{\Phi}(t_{i+1}, t_i)\boldsymbol{P}(t_i^+)\boldsymbol{\Phi}^T((t_{i+1}, t_i) + \boldsymbol{G}_d(t_i)\boldsymbol{Q}_d(t_i)\boldsymbol{G}_d^T(t_i) \tag{2.12}$$

where $\boldsymbol{P}(t_{i+1}^-)$ is the new filter uncertainty, $\boldsymbol{\Phi}(t_{i+1}, t_i)$ is the state transition matrix, $\boldsymbol{P}(t_i^+)$ is the current filter uncertainty, $\boldsymbol{G}_d(t_i)$ is the noise matrix, and $\boldsymbol{Q}_d(t_i)$ contains the strength of each noise source. The variance of each white, Gaussian noise source defined in the noise vector $\boldsymbol{w}_d(t_i)$ is contained on the diagonal of the noise matrix $\boldsymbol{Q}_d(t_i)$ as defined in Equation (2.13)

$$E\{\boldsymbol{w}_d(t_i)\boldsymbol{w}_d(t_j)\} = \begin{cases} \boldsymbol{Q}_d(t_i) & t_i = t_j \\ 0 & t_i \neq t_j \end{cases} \tag{2.13}$$

where $\boldsymbol{w}_d(t_i)$ is the noise vector and $\boldsymbol{Q}_d(t_i)$ contains the noise source strengths on the diagonal. Note that all the off-diagonal terms are zero because each noise source is independent.

Time propagation occurs regardless of the availability of measurement updates. However, note in Equation (2.12) that the filter uncertainty only increases during time propagation. Unless sensor measurements are provided, the Kalman filter uncertainty in the filter states will grow to unusable levels. For example, some precise navigation

applications require centimeter-level accuracy. If the filter uncertainty grows much beyond 10-20 centimeters, the filter navigation solution no longer provides centimeter-level accuracy. The measurement update process is presented in the next section.

2.3.1.3 Measurement Update. The measurement update step occurs after time propagation when a sensor measurement is available [16]. The time index t_{i+1}^- defines the time step immediately before a measurement update and t_{i+1}^+ defines the time step immediately after a measurement update. A measurement update is composed of three equations. First, the Kalman gain is computed in Equation (2.14)

$$\boldsymbol{K}(t_i) = \boldsymbol{P}(t_{i+1}^-)\boldsymbol{H}^T(t_i)[\boldsymbol{H}(t_i)\boldsymbol{P}(t_{i+1}^-)\boldsymbol{H}^T(t_i) + \boldsymbol{R}(t_i)]^{-1} \qquad (2.14)$$

where $\boldsymbol{K}(t_i)$ is the Kalman gain, $\boldsymbol{P}(t_{i+1}^-)$ is the current filter uncertainty, $\boldsymbol{H}(t_i)$ is the measurement matrix, and $\boldsymbol{R}(t_i)$ is the measurement model uncertainty. Next, the state estimate is updated with the sensor observation in Equation (2.15)

$$\hat{\boldsymbol{x}}(t_{i+1}^+) = \hat{\boldsymbol{x}}(t_{i+1}^-) + \boldsymbol{K}(t_i)[\boldsymbol{z}(t_i) - \boldsymbol{H}(t_i)\hat{\boldsymbol{x}}(t_{i+1}^-)] \qquad (2.15)$$

where $\hat{\boldsymbol{x}}(t_{i+1}^+)$ is the updated state estimate, $\hat{\boldsymbol{x}}(t_{i+1}^-)$ is the current state estimate, $\boldsymbol{K}(t_i)$ is the Kalman gain, $\boldsymbol{z}(t_i)$ is the sensor measurement, and $\boldsymbol{H}(t_i)$ is the measurement matrix. Finally, the filter uncertainty is updated to reflect the information added by the sensor observation. Equation (2.16) presents the filter uncertainty update

$$\boldsymbol{P}(t_{i+1}^+) = \boldsymbol{P}(t_{i+1}^-) - \boldsymbol{K}(t_i)\boldsymbol{H}(t_i)\boldsymbol{P}(t_{i+1}^-) \qquad (2.16)$$

where $\boldsymbol{P}(t_{i+1}^+)$ is the updated filter uncertainty, $\boldsymbol{P}(t_{i+1}^-)$ is the current filter uncertainty, $\boldsymbol{K}(t_i)$ is the Kalman gain, and $\boldsymbol{H}(t_i)$ is the measurement matrix. Note that the filter uncertainty can only decrease in Equation (2.16). This reflects that any measurement update, no matter how poor, contains new information about the filter states.

Observing the growth and change in filter uncertainty $\boldsymbol{P}(t_i)$ over time conveys a measure of "observability" and uncertainty the system sensors and vehicle dynamics model provide for each of the system states. For example, the filter uncertainty over time will remain lower for the position states in a Kalman filter where the system sensors measure position directly such as with a GPS receiver or radio range system. Conversely, the uncertainty will continue to increase over time for the position states if the GPS or radio range system ceases to provide position updates. The system dynamics model uncertainty describes how the Kalman filter's uncertainty of the navigation states increase during periods when no sensor measurement updates are available.

Models of real-world systems are generally non-linear. As is evident by the name, the linear Kalman filter accepts only linear vehicle and sensor models. The linearization process to obtain a linear model from a non-linear model removes key information describing the function and operation of the vehicle or sensor system. The non-linear nature of real-world systems can cause the linear Kalman filter states to diverge, resulting in erroneous state estimates. The extended Kalman filter is presented in the next section to address the limitations of the linear Kalman filter.

2.3.2 Extended Kalman Filter. The non-linearities contained in real-world vehicle dynamics and sensor models must be included in the Kalman filter to help reduce filter divergence [15]. The extended Kalman filter (EKF) brings model non-linearities into the estimation process by re-linearizing non-linear vehicle and sensor models about the is current state estimate. The EKF differs from the linear Kalman filter by estimating the error in the filter states as shown in Equation (2.17)

$$\delta\hat{\boldsymbol{x}}(t_i) = \boldsymbol{x}(t_i) - \hat{\boldsymbol{x}}(t_i) \tag{2.17}$$

where $\delta\boldsymbol{x}(t_i)$ is the state estimate error , $\boldsymbol{x}(t_i)$ is the true state vector, and $\hat{\boldsymbol{x}}(t_i)$ is the full estimate of the state vector. Additional differences between the linear and

extended Kalman filters include propagation of the full system state with the non-linear vehicle dynamics model and re-linearization of the models about the current state estimate before performing time propagation or measurement updates. Through these differences, the EKF incorporates non-linearities in the vehicle dynamics and sensor measurement models. The first section presents the non-linear vehicle dynamics and sensor models. The following sections present the EKF time propagation and measurement update algorithms

2.3.2.1 EKF Models. This section presents the non-linear vehicle dynamics and sensor models used in the EKF [15]. These models provide the EKF with prior knowledge of the vehicle and sensor properties. Equation (2.18) contains the non-linear, continuous-time vehicle dynamics model

$$\dot{\boldsymbol{x}}(t) = \boldsymbol{f}[\boldsymbol{x}(t), \boldsymbol{u}(t), t] + \boldsymbol{G}(t)\boldsymbol{w}(t) \tag{2.18}$$

where $\dot{\boldsymbol{x}}(t)$ is the first derivative of the state vector, $\boldsymbol{x}(t)$ is the state vector, $\boldsymbol{u}(t)$ is the control input vector, $\boldsymbol{G}(t)$ is the measurement noise matrix which applies each noise source defined in $\boldsymbol{w}(t)$ to each of the states. The noise source vector describes the uncertainty of the vehicle dynamics model. The state transition function $\boldsymbol{f}$ is a function of the state vector, control input, and time. The strengths of each noise sources are defined in the matrix $\boldsymbol{Q}$ as shown in Equation (2.19).

$$E[\boldsymbol{w}(t_i)\boldsymbol{w}^T(t_j)] = \begin{cases} \boldsymbol{Q}(t_i) & t_i = t_j \\ \boldsymbol{0} & t_i \neq t_j \end{cases} \tag{2.19}$$

Equation (2.20) presents the non-linear sensor model

$$\boldsymbol{z}(t) = \boldsymbol{h}[\boldsymbol{x}(t), t] + \boldsymbol{v}(t) \tag{2.20}$$

16

where $\boldsymbol{z}(t)$ is the sensor measurement, $\boldsymbol{x}(t)$ is the state vector, and $\boldsymbol{v}(t)$ is a vector of white, Gaussian noises with strengths describing the uncertainty of the measurement model. The measurement function $\boldsymbol{h}$ is a function of the state vector and time. The strength of each of noise contained in vector $\boldsymbol{v}(t)$ is defined in the matrix $\boldsymbol{R}$ as shown in Equation (2.21).

$$E[\boldsymbol{v}(t_i)\boldsymbol{v}^T(t_j)] = \begin{cases} \boldsymbol{R}(t_i) & t_i = t_j \\ \boldsymbol{0} & t_i \neq t_j \end{cases} \tag{2.21}$$

The non-linear vehicle dynamics and sensor models must be linearized before they can be implemented in the EKF. Equation (2.22) presents the linearization of the vehicle dynamics model about the current full state vector estimate

$$\boldsymbol{F}[\hat{\boldsymbol{x}}(t), \boldsymbol{u}(t), t] = \left. \frac{\partial \boldsymbol{f}[\boldsymbol{x}, \boldsymbol{u}(t), t]}{\partial \boldsymbol{x}} \right|_{\boldsymbol{x}=\hat{\boldsymbol{x}}(t)} \tag{2.22}$$

where $\hat{\boldsymbol{x}}(t)$ is the estimate of the state vector, $\boldsymbol{u}(t)$ is the control input vector, $\boldsymbol{x}(t)$ is the state vector, and $\boldsymbol{u}(t)$ is the control input vector. The function $\boldsymbol{F}[\hat{\boldsymbol{x}}(t), \boldsymbol{u}(t), t]$ is the linearized result of the partial derivatives of non-linear vehicle dynamics function $\boldsymbol{f}[\hat{\boldsymbol{x}}(t), \boldsymbol{u}(t), t]$ taken with respect to the filter states. As before, the vehicle dynamics are a function of the state estimate, control input and time. To obtain the state transition matrix, the matrix exponential must be applied as shown in Equation (2.23)

$$\boldsymbol{\Phi}[t_{i+1}, t_i, \hat{\boldsymbol{x}}(t_i^+)] = e^{\boldsymbol{F}[\hat{\boldsymbol{x}}(t), \boldsymbol{u}(t), t]\Delta t} \tag{2.23}$$

where $\boldsymbol{\Phi}[t_{i+1}, t_i, \hat{\boldsymbol{x}}(t_i^+)]$ is the state transition matrix, $\boldsymbol{F}[\hat{\boldsymbol{x}}(t), \boldsymbol{u}(t), t]$ is the linearized vehicle dynamics model, and Δt is the time step of the Kalman filter. The matrix exponential must be re-applied when ever the linearized vehicle dynamics model is re-evaluated with a new state estimate.

Equation (2.24) displays the linearization of the sensor model about the current full state vector estimate

$$\boldsymbol{H}[\hat{\boldsymbol{x}}(t_{i+1}^-), t_{i+1}] = \left. \frac{\partial \boldsymbol{h}[\boldsymbol{x}, t_{i+1}]}{\partial \boldsymbol{x}} \right|_{\boldsymbol{x} = \hat{\boldsymbol{x}}(t_{i+1}^-)} \tag{2.24}$$

where $\hat{\boldsymbol{x}}(t_{i+1}^-)$ is the discrete-time state estimate immediately before a measurement update. The function $\boldsymbol{H}[\hat{\boldsymbol{x}}(t_{i+1}^-), t_{i+1}]$ is the linearized result of the partial derivatives of the non-linear measurement function $\boldsymbol{h}[\hat{\boldsymbol{x}}(t_{i+1}^-), t_{i+1}]$ with respect to the filter states. As stated previously, the measurement function is dependent on the state estimate and time. Both the non-linear and linearized vehicle dynamics models are used in time propagation, presented in the next section.

2.3.2.2 *EKF TimePropagation.*

EKF time propagation differs from the linear Kalman filter by propagating the state estimate with the non-linear vehicle dynamics model [15]. The linearized vehicle dynamics model is used to propagate the error of the state estimate. The time index right before time propagation occurs is denoted t_i^+ and right after time propagation occurs is denoted t_{i+1}^-. The starting vehicle navigation states $\boldsymbol{x}(t_0)$ initializes EKF full state estimate $\hat{\boldsymbol{x}}(t_0^+)$. Likewise, the uncertainty in the starting vehicle navigation states initializes the filter covariance or uncertainty $\boldsymbol{P}(t_0^+)$. Note that the state estimate error is zero, $\delta\hat{\boldsymbol{x}}(t_0^+) = 0$, at the beginning of filter operation.

Time propagation for the EKF consists of two equations. Figure 2.3 illustrates the time propagation of the full state estimate using the non-linear vehicle dynamics model. Equation (2.25) presents the integration in discrete-time, mathematical form

$$\hat{\boldsymbol{x}}(t_{t+1}^-) = \hat{\boldsymbol{x}}(t_i^+) + \int_{t_i}^{t_{i+1}} \boldsymbol{f}[\hat{\boldsymbol{x}}(t), \boldsymbol{u}(t), t] dt \tag{2.25}$$

where $\hat{\boldsymbol{x}}(t_{t+1}^-)$ is the new state estimate, $\hat{\boldsymbol{x}}(t_i^+)$ is the current state estimate, and the integration of the non-linear vehicle dynamics model $\boldsymbol{f}[\hat{\boldsymbol{x}}(t), \boldsymbol{u}(t), t]$ computes the change in the full state estimate.
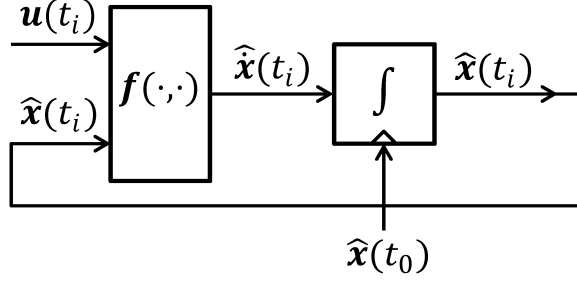
Figure 2.3: Block Diagram for Nonlinear Integration. The full state estimate $\hat{x}$ and control input u are used to calculate the change in the full state estimate denoted as $\dot{\hat{x}}$. The integration step accumulates the changes to produce a whole state estimate.

As stated at the beginning of this section, the initial state estimate error $\delta\hat{x}(t_i)$ is zero. In the measurement update step, the estimate of the state error is used to correct the full state estimate, after which the state estimate error is again returned to zero. Time propagation of the state estimate error consists of propagating a vector of zeros. The filter uncertainty is propagated as shown in Equation (2.26)

$$\boldsymbol{P}(t_{i+1}^-) = \boldsymbol{\Phi}[t_{i+1}, t_i, \hat{\boldsymbol{x}}(t_{i+1}^-)]\boldsymbol{P}(t_i^+)\boldsymbol{\Phi}^T[t_{i+1}, t_i, \hat{\boldsymbol{x}}(t_{i+1}^-)] + \boldsymbol{Q}_d \qquad (2.26)$$

where $\boldsymbol{P}(t_{i+1}^-)$ is the new filter uncertainty, $\boldsymbol{\Phi}[t_{i+1}, t_i, \hat{\boldsymbol{x}}(t_{i+1}^-)]$ is the state transition matrix evaluated at the current full state estimate $\hat{\boldsymbol{x}}(t_{i+1}^-)$, and $\boldsymbol{P}(t_i^+)$ is the current uncertainty of the vehicle dynamics model. Equation (2.27) from [16] is used to obtain the discrete-time vehicle model uncertainty $\boldsymbol{Q}_d$,

$$\boldsymbol{Q}_d(t_{i-1}) \approx \frac{1}{2}\left[\boldsymbol{\Phi}(t_i, t_{i-1})\boldsymbol{G}(t_{i-1})\boldsymbol{Q}(t_{i-1})\boldsymbol{G}^T(t_{i-1})\boldsymbol{\Phi}^T(t_i, t_{i-1}) + \boldsymbol{G}(t_i)\boldsymbol{Q}(t_i)\boldsymbol{G}^T(t_i)\right]\Delta t \tag{2.27}$$

where $\boldsymbol{\Phi}(t_i, t_{i-1})$ is the state transition matrix, $\boldsymbol{G}(t_{i-1})$ is the measurement noise matrix, $\boldsymbol{Q}(t_{i-1})$ is the matrix of continuous-time noise strengths, and Δt is the sample rate of the discrete-time Kalman filter. The next section presents the EKF measurement update.

2.3.2.3 EKF Measurement Update.   The measurement update step occurs after time propagation when a sensor measurement is available [15]. The time index right before a measurement update is denoted t_{i+1}^- and right after a measurement update is denoted t_{i+1}^+. The EKF measurement update consists of four equations. As with the linear Kalman filter, the Kalman gain is computed first as shown in equation

$$\boldsymbol{K}(t_{i+1}) = \boldsymbol{P}(t_{i+1}^-)\boldsymbol{H}^T[\hat{\boldsymbol{x}}(t_{i+1}^-), t_i]\left\{\boldsymbol{H}[\hat{\boldsymbol{x}}(t_{i+1}^-), t_i]\boldsymbol{P}(t_{i+1}^-)\boldsymbol{H}[\hat{\boldsymbol{x}}(t_{i+1}^-), t_i] + \boldsymbol{R}(t_i)\right\}^{-1}$$
(2.28)

where $\boldsymbol{K}(t_i)$ is the Kalman gain, $\boldsymbol{P}(t_{i+1}^-)$ is the current filter uncertainty, $\boldsymbol{H}[\hat{\boldsymbol{x}}(t_{i+1}^-), t_i]$ is the measurement matrix, and $\boldsymbol{R}(t_i)$ is the measurement model uncertainty. Next, the state error is computed as shown in equation

$$\delta\hat{\boldsymbol{x}}(t_{i+1}^+) = \delta\hat{\boldsymbol{x}}(t_{i+1}^-) + \boldsymbol{K}(t_{i+1})\left[\boldsymbol{z}(t_{i+1}) - \boldsymbol{H}[\hat{\boldsymbol{x}}(t_{i+1}^-), t_{i+1}] - \boldsymbol{H}[\hat{\boldsymbol{x}}(t_{i+1}^-), t_{i+1}]\delta\hat{\boldsymbol{x}}(t_{i+1}^-)\right]$$
(2.29)

where $\delta\hat{\boldsymbol{x}}(t_{i+1}^+)$ is the new state estimate error , $\delta\hat{\boldsymbol{x}}(t_{i+1}^-)$ is the current state estimate error, $\boldsymbol{K}(t_{i+1})$ is the Kalman gain, $\boldsymbol{z}(t_{i+1})$ is the sensor measurement, and $\boldsymbol{H}[\hat{\boldsymbol{x}}(t_{i+1}^-), t_{i+1}]$ is the measurement matrix evaluated at the current full state estimate $\hat{\boldsymbol{x}}(t_{i+1}^-)$. Since the state estimate error is zero coming into the measurement update step, Equation (2.29) may be simplified as shown in Equation (2.30).

$$\delta\hat{\boldsymbol{x}}(t_{i+1}^+) = \boldsymbol{K}(t_{i+1})\left[\boldsymbol{z}(t_{i+1}) - \boldsymbol{H}[\hat{\boldsymbol{x}}(t_{i+1}^-), t_{i+1}]\right]$$
(2.30)

The filter uncertainty update follows as displayed in Equation (2.31)

$$\boldsymbol{P}(t_{i+1}^+) = \boldsymbol{P}(t_{i+1}^-) - \boldsymbol{K}(t_{i+1})\boldsymbol{H}[\hat{\boldsymbol{x}}(t_{i+1}^-), t_{i+1}]\boldsymbol{P}(t_{i+1}^-)$$
(2.31)

where $\boldsymbol{P}(t_{i+1}^+)$ is the new filter uncertainty, $\boldsymbol{P}(t_{i+1}^-)$ is the current filter uncertainty, $\boldsymbol{K}(t_{i+1})$ is the Kalman gain, and $\boldsymbol{H}[\hat{\boldsymbol{x}}(t_{i+1}^-), t_{i+1}]$ is the measurement matrix evaluated at the current full state estimate $\hat{\boldsymbol{x}}(t_{i+1}^-)$. Finally, the state estimate error is used to correct the full state estimate as presented in Equation (2.32)

$$\hat{\boldsymbol{x}}(t_{i+1}^+) = \hat{\boldsymbol{x}}(t_{i+1}^-) + \delta\hat{\boldsymbol{x}}(t_{i+1}^+) \tag{2.32}$$

where $\hat{\boldsymbol{x}}(t_{i+1}^+)$ is the new full state estimate, $\hat{\boldsymbol{x}}(t_{i+1}^-)$ is the current full state estimate, and $\delta\hat{\boldsymbol{x}}(t_{i+1}^+)$ is the filter error estimate. After the full state estimate is corrected, the state estimate error is reset back to zero. The EKF time propagation step occurs next and repeats until another sensor measurement becomes available. This concludes the EKF algorithm.

2.4 Inertial Navigation

The inertial navigation system (INS) is a passive navigation device. Unlike GPS, INS cannot be jammed by radio frequency signals. The passive nature of INS makes it ideal for providing navigation capability in GPS-denied environments [25].

This section covers strap-down inertial navigation [25]. In a strap-down INS setup the sensors are fixed in orientation relative to the INS body. This differs from a platform INS where the sensors are free to rotate relative to the INS body and remain stationary relative to the fixed stars. The INS accelerometer and gyroscope sensors are covered in the first section. The next section presents the equations necessary for strap-down INS mechanization. The last section details error sources which result in drift of the INS navigation solution.

2.4.1 INS Sensors. The INS is composed of two types of sensors: accelerometers and gyroscopes [25]. Accelerometers consist of a mass and transducer which, when accelerated along its input axis, generates an electrical signal. This electrical signal is used by the INS as the magnitude of acceleration along the specified axis.

This interaction follows Newton's second law of motion which is described by the equation

$$F = ma \tag{2.33}$$

where F is the force which results when an acceleration a is applied to a rigid object of mass m. Conversion of the acceleration into an electrical signal is performed by the transducer. One form of transducer measures the displacement of a mass attached to a spring. As the acceleration increases along the input axis, the displacement of the mass increases.

Gyroscopes originally consisted of a spinning mass suspended within two independent gimbals. The model HG1700 INS applied in this thesis uses ring-laser gyros which are described in this paragraph [19]. The ring-laser gyro is one example of an optical gyroscope. Optical gyroscopes used interferometers or interferometric methods to sense angular motion [25].

Current technology has advanced to use ring laser gyros which are described in this paragraph. The inertia of a spinning mass causes it to resist changes in orientation. In a platform INS, the gyroscope is not allowed to precess or rotate beyond very small angles. This type of gyroscope is called a rate-gyro. Force is applied by the spinning mass to the gimbals when an angular velocity is applied to the input axis of the gyroscope. Electronic transducers on the gimbals measure the force applied to the gimbals by the spinning mass, allowing measurements of angular rate.

An INS typically hosts three accelerometers and three gyroscopes. The input axes of the accelerometers and gyroscopes are positioned at right-angles along the three main axes of the INS b-frame. The accelerometers measure specific force which accounts for both changes in velocity and gravity. The gyroscopes measure the rate of angular rotation of the INS platform. Together, these six sensors enable measurement

of the position, velocity, and attitude of the INS platform through the mechanization of the sensor data.

2.4.2 INS Mechanization. The data provided by the accelerometers and rate-gyros is mechanized through navigation equations to provide measurements of position, velocity, and attitude of the INS b-frame [25]. The strap-down nature of the INS requires knowledge of the INS orientation for correct usage of the accelerometer measurements.

INS mechanization begins with attitude calculations based on gyroscope measurements. The gyroscopes measure the angular rate of the INS body. Equation (2.34) shows the calculation of the INS body rate

$$\boldsymbol{\omega}_{n'b}^{b} = \boldsymbol{\omega}_{ib}^{b} - \boldsymbol{C}_{n'}^{b}[\boldsymbol{\omega}_{ie}^{n'} + \boldsymbol{\omega}_{en'}^{n'}] \tag{2.34}$$

where $\boldsymbol{\omega}_{n'b}^{b}$ is the body rate, $\boldsymbol{\omega}_{ib}^{b}$ is the angular rates measured by the INS gyroscopes, $\boldsymbol{C}_{n'}^{b}$ is the DCM from the INS b-frame to the local n'-frame, $\boldsymbol{\omega}_{ie}^{n'}$ is the turn rate of the Earth with respect to the i-frame expressed in the n'-frame, and $\boldsymbol{\omega}_{en'}^{n'}$ is the turn rate of the local n'-frame with respect to the e-frame, expressed in the n'-frame.

The orientation of the INS body resides in the DCM $\boldsymbol{C}_{n'}^{b}$. This DCM is updated with the INS body rate $\boldsymbol{\omega}_{n'b}^{b}$ through Equation (2.35)

$$\dot{\boldsymbol{C}}_{n'}^{b} = \boldsymbol{C}_{n'}^{b}\boldsymbol{\Omega}_{n'b}^{b} \tag{2.35}$$

where $\boldsymbol{\Omega}_{n'b}^{b}$ is the skew-symmetric form of the body rate. Equation (2.36) displays the skew-symmetric form

$$\boldsymbol{\Omega}_{n'b}^{b} = \begin{bmatrix} 0 & -\omega_z & \omega_y \\ \omega_z & 0 & -\omega_x \\ -\omega_y & \omega_x & 0 \end{bmatrix} \tag{2.36}$$

23

where $\boldsymbol{\omega}_{n'b}^{b} = [\omega_x, \omega_y, \omega_z]$.

Next, the INS body DCM is transposed, $\boldsymbol{C}_b^{n'} = \boldsymbol{C}_{n'}^{bT}$, to rotate the accelerometer specific force measurements, $\boldsymbol{f}^b = [f_x, f_y, f_z]$, from the INS b-frame to the local n'-frame. Equation (2.37) presents the computation of change in velocity

$$\dot{\boldsymbol{v}}_e^{n'} = \boldsymbol{C}_b^{n'} \boldsymbol{f}^b - [2\boldsymbol{\omega}_{ie}^{n'} + \boldsymbol{\omega}_{en'}^{n'}] \times \boldsymbol{v}_e^{n'} + \boldsymbol{g}_l^{n'} \tag{2.37}$$

where $\dot{\boldsymbol{v}}_e^{n'}$ is the change in velocity with respect to the e-frame expressed in the local n'-frame, $\boldsymbol{C}_b^{n'}$ is the INS body orientation, $\boldsymbol{f}^b$ is the accelerometer measurements in the INS b-frame, $\boldsymbol{\omega}_{ie}^{n'}$ is the turn rate of the Earth with respect to the i-frame expressed in the n'-frame, $\boldsymbol{\omega}_{en'}^{n'}$ is the turn rate of the local n'-frame with respect to the e-frame expressed in the n'-frame, $\boldsymbol{v}_e^{n'} = [v_N, v_E, v_D]^T$ is the velocity with respect to the e-frame expressed in the local n'-frame, and $\boldsymbol{g}_l^{n'}$ contains the local gravity vector.

The INS mechanization contained in the above equations integrates the changes in velocity and body orientation to compute the velocity and attitude of the INS body in the local n'-frame. Integration of the velocity $\boldsymbol{v}_e^{n'}$ provides navigation position relative to the starting location of the INS.

2.4.3 INS Error Sources. Imperfections in accelerometers, gyroscopes, and computation systems are three areas that contribute to accumulation of error in the INS position, velocity and attitude solution [25]. This accumulation of error appears as a drift in the INS navigation solution. Additional sources of error arise from uncertainty in the initial INS position and orientation. The INS provides navigation relative to a starting location and attitude. Any uncertainty in the initial position or attitude introduces error into the INS navigation solution. The following sections present details for errors contributed by the accelerometers, gyroscopes, and computation system.

2.4.3.1   Accelerometer Errors.   Accelerometers have four main sources of error which contribute to INS navigation drift [25]. First, a fixed bias error is an offset present in the measured acceleration which remains constant regardless of the application of further acceleration. Next, a scale-factor error is a ratio which describes the error between the applied and the measured acceleration. Cross-coupling errors are erroneous outputs from the accelerometer to accelerations applied orthogonal to its input axis. Finally, vibro-pendulous errors describe the resonance characteristics of the suspended mass inside an accelerometer. These error sources are taken into account in the accelerometer model shown in Equation (2.38)

$$\tilde{a}_x = (1 + S_x)a_x + M_y a_y + M_z a_z + B_f + B_v a_x a_y + n_x \qquad (2.38)$$

where $\tilde{a}_x$ is the corrupted accelerometer measurement, a_x is the true accelerometer measurement, S_x is the scale factor error, M_y and M_z are the cross-axis coupling errors, B_f is the measurement bias, B_v is the vibro-pendulous error coefficient, and n_x is a random bias which is caused by instabilities within the accelerometer assembly.

2.4.3.2   Gyroscope Errors.   The rate-gyroscopes used in the INS have six significant sources of error [25]. The first three error sources describe non-idealities in the structure of the gyroscope. Reduction in gyroscope sensitivity due to flex lead torques and friction in the gimbal pivots is termed g-insensitivity bias. Increased gyroscope sensitivity due to unbalanced mass on the gimbals or unbalance spinning gyro mass is termed g-sensitivity bias. Third, the anisoelastic bias describes unbalanced compliance of the gyroscope's float assembly along the input and spin axes. The remaining three error sources are the scale-factor error, cross-coupling error, and the zero-mean random bias error.

Similar to the accelerometer, the scale-factor error describes the ratio of applied angular velocity to the measured angular velocity. Cross-coupling errors account for the effects of angular velocities applied orthogonal to the gyro's input axis. Finally, the

zero-mean random bias captures errors arising from gyroscope mechanical instabilities such as pivot friction and random movements of the spin motor about the gyro's spin-axis. Equation (2.39) presents a formula which accounts for the effects of these errors on the output signal from a gyroscope

$$\tilde{\omega}_x = (1 + S_x)\omega_x + M_y\omega_y + M_z\omega_z + B_{fx} + B_{gx}a_x + B_{gz}a_z + B_{axz}a_xa_z + n_x \quad (2.39)$$

where $\tilde{\omega}_x$ is the measured angular rate of the gyro about its input axis; ω_x is the true angular rate of the gyro about its input axis; ω_y and ω_z are the angular rates about the output and spin axes of the gyro, respectively; a_x and a_z are the accelerations of the gyro along the input and spin axes, respectively. S_x is the scale factor, M_y and M_z are the cross-coupling coefficients, B_{fx} is the g-insensitivity bias, B_{gx} and B_{gz} are the g-sensitivity bias coefficients, B_{axz} is the anisoelastic bias coefficient and n_x is the zero-mean random bias.

2.4.4 Computation Errors. Measurements from the accelerometers and gyroscopes are applied to the mechanization equations shown in Section 2.4.2 by computers. Limitations in computers comprise the third set of errors.

Computers have fixed precision due to pre-determined register sizes and memory limitations. Numerical truncation due to limited precision adds error to each INS computation. Bandwidth limitations due to the internal clock frequency of the INS computer present additional error where changes in attitude and velocity occur faster than the computer is sampling. These measurements are lost, resulting in unaccounted attitude and velocity changes which add to the INS error.

2.5 Radio Positioning Methods

The errors accumulated from navigation with an INS presented in Section 2.4 grow over time at an increasing rate which is seen as a drift in the navigation solution.

To obtain precise navigation solutions, the drift present in INS navigation systems must be constrained. A source of error constraint comes from sensors with non-integrated measurement error. Navigation by radio range measurements is presented as a source of non-integrated error.

This section proceeds with a survey of other work conducted in the area of range-aided navigation. Next, three techniques for positioning a mobile radio transceiver relative to stationary radio transceivers with known locations. The mobile radio transceiver is labeled as a Mobile Station (MS) and the stationary radio transceiver is labeled as a Base Station station (BS). Radio frequency (RF) signals sent between the MS and BSs provide positioning information. Time of Arrival (TOA), Angle of Arrival (AOA), and Received Signal Strength (RSS) comprise general forms of radio positioning techniques [14].

2.5.1 Range-Aided Navigation Survey. This section presents an survey of other research that has been conducted in range-aided navigation technologies. Applications range from military vehicle navigation to industrial asset tracking and fire-fighter personnel accountability.

Ernsberger [8] explored radio-aided navigation with the incorporation of image, baro-altimeter, and inertial measurements. Through computer-based simulations, the performance of this extended Kalman filter-based navigation system was evaluated. The simulated range system consisted of radios fixed to the ground and radios mounted on moving vehicles. The imaging system consisted of monocular sensors mounted to each of the vehicles. The horizontal RMS navigation position error using only range and baro-altimeter measurements was 20.24 meters. Incorporation of the imaging system and inertial measurements produced a horizontal RMS position error of 6.81 meters. The inertial and image data provided a notable improvement in positioning accuracy.

Ultra wide band (UWB) positioning technology also presents a viable range-aided navigation system. Fontana, Richley, and Barney [10] detail an UWB posi-

tioning system use to position and track assets. The specific application is industrial facilities and hospitals. This UWB ranging system uses a network of receivers placed at know locations inside the building. Then, small active UWB tags are placed on objects to be positioned and tracked. The burst transmission from each active tag includes an ID and optional fields for additional data. The interval of tag transmission can range from 5 seconds to an hour depending on the application. Battery life in excess of 3.8 years can be obtained from the 1 amp-hour lithium battery cells contained in each active tag. A central processing hub consisting of a dedicated computer processes the time-tagged signals collected from each active tag. Time of arrival methods are used with leading-edge signal detection circuitry to obtain sub-foot position accuracy. Positioning standard deviation below 0.5 feet is demonstrated in this paper.

Additional range-aided navigation applications are found in the arena of search and rescue. Worcester Polytechnic Institute's (WPI) [4–6] Precision Personnel Locator (PPL) system is one such research effort which has produced a radio-range based positioning system which tracks personnel in indoor environments assuming no existing radio infrastructure. This positioning system consists of reference radio stations potentially located on emergency vehicles. Once the vehicles arrive at a scene, the PPL system performs an auto-calibration to position each of the emergency vehicles and setup a local navigation reference frame. Small transmitters worn by each of the emergency personnel transmit time-tagged data which is received by in-range reference stations. Time-difference of arrival (TDOA) algorithms are used to position each of the personnel within range of this system. Additional relevant information such as distress signals, temperature, and personnel diagnostic data is also relayed to the reference stations. A base station collects the data from the reference stations and provides a user-interface which presents relevant position and health information to the command and control center at the scene.

Key contributions from each of these research efforts include simulation of range-aided navigation with additional sensors, implementation of range-aided positioning

in challenging indoor environments, and range-aided navigation systems which do not require prior information of the building or environment. This section continues with presentation of range-aiding navigation algorithms and techniques.

2.5.2 Time of Arrival. TOA measurements provide slant range distances between two radios. The TOA radio positioning method is implemented by the Raytheon DH500 radios used in this thesis. Slant range is defined as the line of sight (LOS) distance between the BS and MS. The slant range is directly proportional to the propagation time of the radio signal from the BS to the MS. Equation (2.40) presents the calculation of the slant range

$$R_i = c(t_{MS} - t_{BS_i}) \tag{2.40}$$

where R_i is the slant range, t_{BS_i} is the time the signal left the base station, t_{MS} is the time the signal arrived at the mobile station, and c is the speed of light. TOA positioning algorithms require precise time synchronization between all radios. TOA also requires a time stamp or symbol be inserted into the transmitted signal to allow the receiving radio to determine when the signal left the transmitter.

RF signal multipath significantly degrades TOA measurement accuracy [14]. Multipath is present even when two radios have LOS visibility. RF signals bounce off buildings and other objects in the environment arriving at the receiving radio at different times. This presents a positive bias or apparent increase in the distance between two radios for the reflected RF signals. Specialized algorithms presented in the Section 2.6 address both the multipath and non-LOS (NLOS) issues.

Given a two-dimensional Cartesian coordinate system, a minimum of two slant ranges are required to solve for the location of the mobile radio. Equation (2.41) present the mathematical solution

$$R_i = \sqrt{(x_{MS} - x_{BS_i})^2 + (y_{MS} - y_{BS_i})^2} \tag{2.41}$$
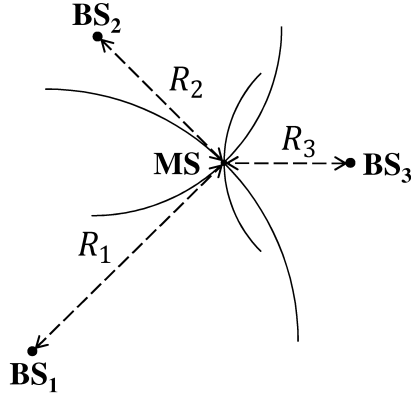
Figure 2.4:   Positioning Based on Time of Arrival for a 3-Dimensional Solution. The time of arrival for the radio signals sent between each mobile and base station pair presents a measurement of the slant range distance between the radio antennas [14].
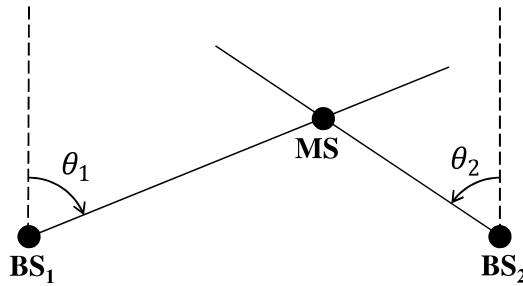
Figure 2.5:   Positioning Based on Angle of Arrival for a 2-Dimensional Solution. Strict definitions of radio signal arrival angles are required to perform angle of arrival radio positioning [14].

where x_{MS} and y_{MS} are the position of the mobile station, x_{BS_i} and y_{BS_i} are the position of the ith base station, and R_i is the true slant range between them. At least three slant range measurements are required to solve for the MS position in a three-dimensional coordinate system as shown in Figure 2.4.

2.5.3 Angle of Arrival.   AOA measurements provide the angle of signal arrival to a MS from a BS. A benefit of AOA techniques is the lack of time synchronization needed between the MS and BSs. A significant drawback is the specialized hardware needed to determine the AOA of incoming RF signals [14]. Figure 2.5 presents a graphical depiction of two-dimensional, AOA positioning.

30

A two-dimensional position calculation requires two AOA measurements. Equations (2.42) and (2.43) present the two-dimensional mathematical position solution

$$x_{MS} = \frac{x_{BS_1}tan(\pi - \theta_1) + x_{BS_2}tan(\pi - \theta_2) + y_{BS_2} - y_{BS_1}}{tan(\pi - \theta_1) + tan(\pi - \theta_2)} \qquad (2.42)$$

$$y_{MS} = \frac{y_{BS_1}tan(\pi - \theta_2) + y_{BS_2}tan(\pi - \theta_1) + (x_{BS_2} - x_{MS_1})tan(\pi - \theta_1)tan(\pi - \theta_2)}{tan(\pi - \theta_1) + tan(\pi - \theta_2)}$$
$$(2.43)$$

where x_{BS_1} and y_{BS_1} are the position of base station 1, x_{BS_2} and y_{BS_2} are the position of base station 2, θ_1 is the angle from base station 1 to the mobile station, θ_2 is the angle from base station 2 to the mobile station, and x_{MS} and y_{MS} is the resulting position of the mobile station. Three AOAs must be received to determine the three-dimensional location of the MS.

The accuracy of AOA positioning depends on the accuracy of AOA measurement. As the receiving radio moves further away from the transmitting radio, AOA measurements become less accurate. This is due to the geometry of the radios and RF multipath introduced by reflections of the RF signals from objects present in the environment.

2.5.4 Received Signal Strength. The RSS positioning algorithm provides measurement of RF signal attenuation between two radios [14]. The farther a RF signal propagates, the more the received signal strength decreases. Given a RF channel model and known initial signal strength, the amount of signal attenuation directly correlates to the distance between the radios. The RSS method provides accurate slant ranges for an environment clear of multipath fading and shadowing. Benefits of RSS include the simplicity in hardware requirements and lack of the need for precise time synchronization between the MS and BSs. Unknown RF channel models present a significant drawback for the RSS positioning method. Both outdoor and
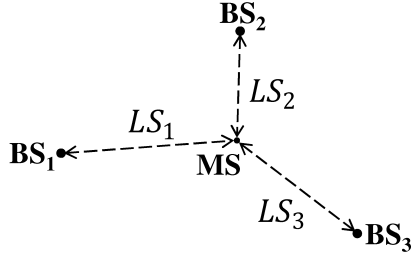
Figure 2.6: Positioning Based on Received Signal Strength for 3-Dimensional Solution. Un-modeled RF channel signal reduction between each mobile and base radio pair introduces significant uncertainty into the position solution [14].

indoor NLOS conditions present multipath fading issues with varying RF channel models [14]. Advanced algorithms, RSS contour maps, and multiple RSS measurements from several stationary radios help to mitigate these issues [14]. A minimum of two BSs are required for a two-dimensional position solution and three are required for a 3D solution. Figure 2.6 presents a graphical representation of a three-dimensional RSS solution.

2.6 Multipath Mitigation

The radio range positioning algorithms presented in the previous section heavily depend on clear RF channels between radios to provide accurate measurements. Buildings, walls, and other obstructions sources significantly degrade the position solution obtained from each positioning algorithm [27]. A significant source of position error comes from multipath interference. Estimation and removal of the errors contributed by multipath allows for calculation of a much more accurate position solution.

This section covers software-based methods to estimate and reduce multipath effects on TOA measurements between two radios. The ideal RF channel between the BS and MS radios is free of RF signal reflections, scattering, and fading. This condition is rarely achieved, especially in urban canyons where buildings, electrical services, and vehicles cause RF reflection, scattering, and fading. As a radio wave bounces off buildings, the signal strength decreases and the overall signal path in-
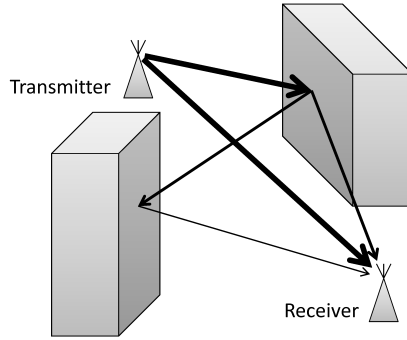
Figure 2.7: Depiction of RF Multipath. The signal from the transmitter decreases in strength with each reflection. The reflected signals travel a longer total distance to the receiver which adds a positive error bias to the slant range measurement.

creases. The increased signal path causes the TOA measurements to increase with a positive error bias.

Figure 2.7 presents a depiction of a multipath environment and NLOS effects on a single radio wave. Given the signal path between the MS and BS is LOS, part of the radio wave will arrive at the receiver directly from the transmitter. The rest of the radio wave is reflected, scattered, and the signal strength is reduced as the number of signal reflections increases. Also, note the increase in signal path length from the strongest LOS path to the weakest NLOS path. The increased signal path appears as a positive error in the slant range. A broad array of both software and hardware methods exist to reduce and mitigate multipath effects. This section presents an overview of software-based error mitigation techniques which occurs after the hardware due the proprietary nature of the Raytheon DH500 radios.

Software based multipath mitigation methods take on several forms. Linear and Gaussian models such as the Ring of Scatterers (ROS), Disk of Scatterers (DOS), and clipped Gaussian models provide well-known methods of estimating NLOS multipath features [2,3]. These three models are briefly presented in this section. One Kalman filter multipath mitigation method uses a biased Kalman filter to estimate and smooth the NLOS effects on the TOA measurements [12]. Another Kalman filter method utilizes an interacting multiple model (IMM) Kalman filter with individual models tuned for LOS and NLOS conditions. As the MS moves in and out of NLOS conditions,

the IMM Kalman filter selects the appropriate model based on the incoming signal variance [7, 9].

The Cramer-Rao lower bound (CRLB) provides a mathematical calculation of the lower limit for the covariance matrix of an unbiased estimate of unknown parameters. Evaluation of the Kalman filter uncertainty in terms of the CRLB provides the best expected navigation performance. Given known multipath conditions, a modified algorithm termed the generalized CRLB (G-CRLB) provides the best expected positioning accuracy [21].

The three scatterer models mentioned above are depicted in Figure 8(c). These models describe the likelihood that an object causing scatter is present in the specified region. The BS radios are positioned at known stationary locations. The MS radio moves around within the region of application. Application of these models to obtain a 2-dimensional position solution requires at least three separate, visible BS radios. The next paragraph develops the scatterer models.

In order to develop these three models, several variables are defined. The error in the measured slant range η_{ij} is computed in Equation (2.44)

$$\eta_{ij} = l_{ij} - R_i \tag{2.44}$$

where R_i is the true slant range from BS_i to the MS in the center of the models and the j-th multipath corrupted slant range measured by the MS is labeled l_{ij}. Implementation of each model consists of statistical estimation of the mean and variance of the incoming slant range measurements. These statistics are used to iteratively estimate the MS position (x_{ms}, y_{ms}) and associated model parameter r.

The definition of the model parameter r depends on the model implemented. For the ROS model, $r = R_r$ where R_r defines the radius of the ring. For the DOS model, $r = R_d$ where R_d defines the radius of the disk. For the Gaussian model, $r = \sigma_g$ where σ_g defines the standard deviation of the Gaussian scatterer distribution

(a) Ring Of Scatterers (ROS) Model   (b) Disk Of Scatterers (DOS) Model

(c) Clipped Gaussian Scatter Model
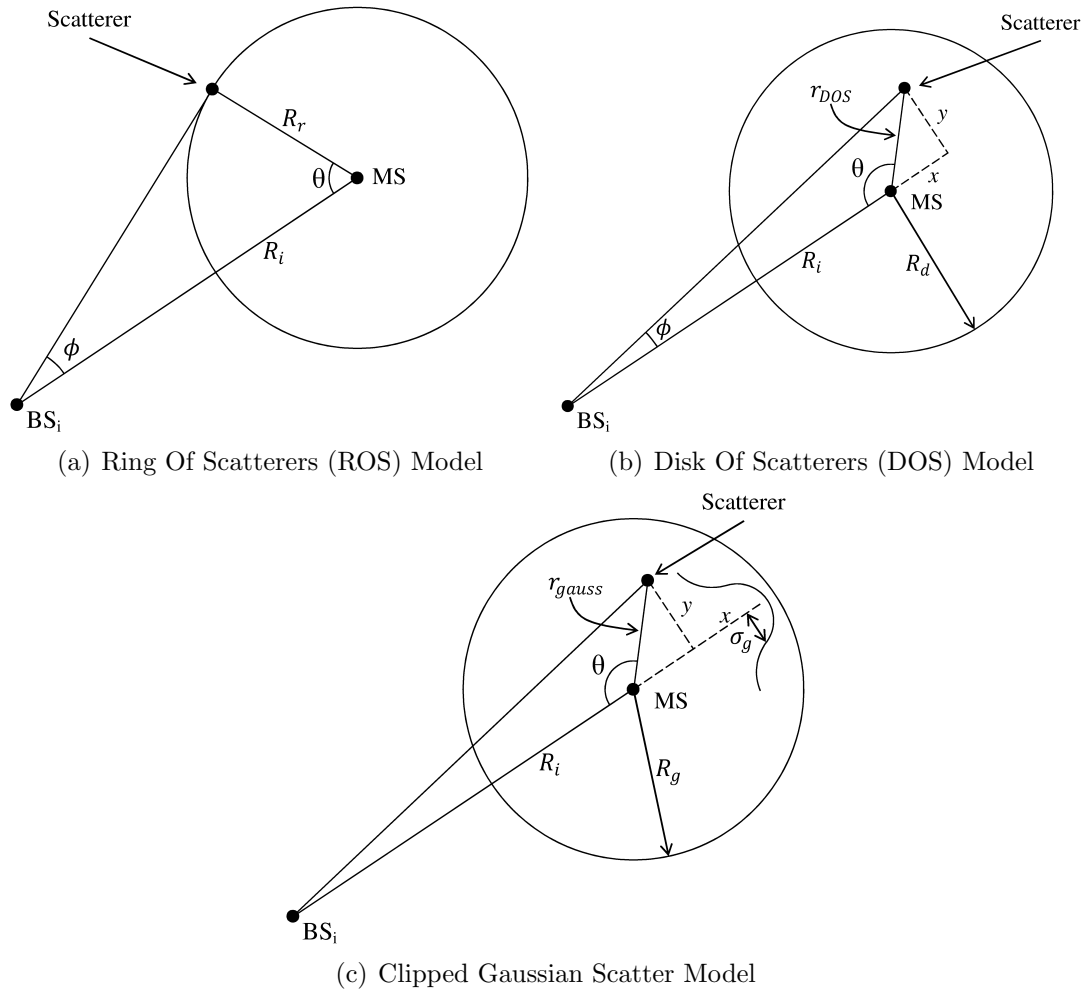
Figure 2.8:   Illustration of the Three Scatterer Models [3]. The scatterers lie on the ring for the ROS. For the DOS model, the scatterers are uniformly distributed within the ring. The clipped Gaussian model positions the scatterers in a Gaussian distribution centered around the master station.

on the disk. The three model parameters are defined for simplicity in Equation (2.45). Definition of the PDFs for each model is contained in [2].

$$
r = \begin{cases} R_r & \text{ROS Model} \\ R_d & \text{DOS Model} \\ \sigma_g & \text{Gaussian Clipped Model} \end{cases} \tag{2.45}
$$

Application of the scatterer models to determine the position (x_{ms}, y_{ms}) of the MS consists of computing the variance of the TOAs for at least three BS-MS pair. Next, instantiate the PDF for the desired scatterer model three times, equating the variances from each radio pairs to each of the PDF realizations. The position of the MS is found through simultaneous solution of the three PDF equations [2].

Al-Jazzar and Caffery [2, 3] present results which show the error reduction capability of the scatterer models. Position errors are reduced by 100-200 meters depending on the model used and associated parameters. The results presented also show the scatterer models to be effective at position error reduction when applied to environments which do not conform to these models.

2.7 *Baro-Altitude Aiding*

Radio range positioning on the surface of the Earth provides excellent observability of the horizontal navigation channels, but poor observability in the vertical navigation channel. A barometer provides measurement of air pressure. Since air pressure varies with altitude, barometric pressure provides an indirect measurement of altitude. The use of barometric pressure to aid in altitude measurement is termed baro-altitude aiding. Baro-altitude aiding is presented in this section to aid in measurement of the vertical navigation channel. This section presents an air pressure to altitude conversion formula and then discusses errors associated with baro-altitude aiding.

Baro-altitude aiding provides a relative measure of altitude based on current air pressure. As altitude increases, air pressure decreases and vise versa. The difference in air pressure between two locations provides a measure of altitude change. Equation (2.46) presents the conversion from change in air pressure to change in height [24]

$$\Delta h = 44330 \cdot \left(1 - \left(\frac{P}{P_0}\right)^{0.19}\right) - h_{init} \tag{2.46}$$

where Δh is the change in height in meters, P is the current air pressure in kPa, P_0 is defined as 101.325 kPa which is the standard pressure, and h_{init} is the initial height in meters.

Several error sources exist for baro-altitude aiding. Local weather phenomenon causes air pressure to change slowly over time. The use of baro-altitude aiding inside buildings or vehicles introduces further error from building pressurization by the ventilation system and pressure changes due to opening and closing doors. A stationary reference barometer provides mitigation of air pressure drift due to local weather phenomenon [24]. Careful Kalman filter barometer measurement integration and barometer response modeling can help mitigate error effects from ventilation systems and operation of building doors. The next paragraph overviews a Kalman filter implementation of baro-altitude aiding.

The EKF implemented in this thesis uses baro-altitude aiding to assist in vertical channel measurement. Correct EKF implementation requires modeling of the error source present in the baro-altitude aiding sensor. Kim and Sukkarieh [11] model the barometric error as the output of a first-order Gauss Markov (FOGM) process with the measurement noise modeled by a white Gaussian noise source. Figure 2.9 presents the block diagram depiction of the FOGM generation process. The period β and magnitude $\sqrt{2\sigma_w^2\beta}$ of the FOGM process are defined by analyzing real baro-altimeter data [11]. The magnitude of the white Gaussian measurement process noise $v(t)$ is determined based on the individual sensor characteristics. The Gaussian, zero-mean noise sources $w(t)$ and $v(t)$ are independent.
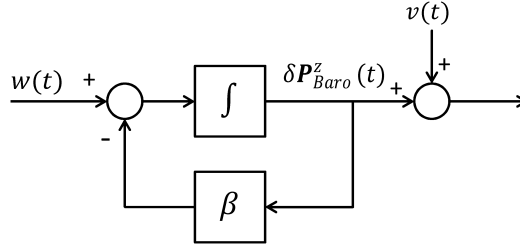
Figure 2.9:   Barometer Error Model. The FOGM describes barometer error and the white Gaussian noise source $v(t)$ describes measurement process noise.

2.8   Chi Square Statistics

Sensor models used in linear and extended Kalman filters assume the uncertainty or error distribution of sensor is Gaussian [16]. To ascertain whether the measurement errors from a given sensor fit a Gaussian distribution, the Chi Squared statistical test is introduced. The Chi Squared test provides a numerical Goodness Of Fit (GOF) assessment of how well a collection data points conforms to a null hypothesis [13]. For the purposes of this thesis, the null hypothesis is the Gaussian distribution. Explanation of the Chi Squared algorithm follows.

The sample space of the given data set of sensor error and of the null hypothesis S_X is divided up into K disjoint intervals. The number of sensor error samples contained in each interval is labeled n_k. Likewise, the number of null hypothesis samples contained in each interval is represented by m_k. Next, apply the formula provided in Equation (2.47) to compute the Chi Squared statistic

$$D^2 = \sum_{k=1}^{K} \frac{(n_k - m_k)^2}{m_k} \tag{2.47}$$

where D^2 is the Chi Squared statistic, K is the number of disjoint intervals, n_k is the number of error samples within each interval, and m_k is the number of null hypothesis within each interval. The value D^2 is low if the range error fits the null hypothesis. If the range error does not fit the null hypothesis, D^2 has a high value. The outcome of this comparison is presented as *non-Gaussian* or *Gaussian*, either rejecting or accepting the null hypothesis respectively.

The threshold comparison of D^2 is performed at the 5% significance level. The significance level is represented by the variable t_α. Table 8.3 in [13] contains a set of values for various significance levels. Therefore, if $D^2 \geq t_\alpha$ the outcome is *non-Gaussian* and the null hypothesis is rejected. If $D^2 < t_\alpha$ the outcome is *Gaussian* and the null hypothesis is accepted.

The Chi Squared test provides a numerical assessment of how well the measurements from a sensor fit a white Gaussian distribution. The Chi Squared GOF test is used in Chapter IV to provide a mathematical determination whether a data set fits the Gaussian distribution or not. The Chi Squared test assists in evaluation and refinement of sensor models used in the Kalman filter where the measurement uncertainty is assumed to be white and Gaussian in its distribution. However, development of accurate sensor models when errors do not conform to the white Gaussian distribution assumption can be prohibitively complex. The next section presents adaptive filters which provide an alternative to complex sensor models.

2.9 Adaptive Filter Algorithms

The Kalman filter models sensor error with predetermined measurement uncertainty contained in the variable $\boldsymbol{R}$. The basic Kalman filter or EKF assumes the error contained in the sensor's measurements remains constant during the Kalman filter's operation. Radio range measurements break this assumption in real-world operation. The results of range characterization presented in Chapter IV will clearly show the actual range measurement error is significantly greater compared to the predefined measurement uncertainty $\boldsymbol{R}(t_i)$. The discrepancy between the predetermined uncertainty and actual range uncertainty causes the Kalman filter to improperly use the range measurements. Adaptive filter algorithms allow the measurement uncertainty to be adjusted during filter operation which enables the Kalman filter to properly utilize the range measurements.

The two adaptive filter algorithms discussed in this section modify the filter techniques presented in Section 2.3 to account for changes the system dynamics and

sensor model uncertainties. Residual monitoring presents a technique to discard measurements with uncertainty greater than a predetermined threshold. Presentation of Sage-Husa algorithm follows which contains a notable computational efficiency improvement over the AKF and adds estimation of the mean of the system dynamics and measurement model uncertainty.

2.9.1 Residual Monitoring. Residual monitoring encompasses a group of algorithms which provide information based on the measurement residual. Applications of residual monitoring include, sensor failure detection by application of a likelihood function and rejection of spurious measurements by thresholding residual covariances above 3-σ of the sensor model uncertainty. Each algorithm is based on statistical assumptions about the measurement residual. This section presents the statistical model for the measurement residual and two algorithms to exploit deviations from this model.

Maybeck [16] presents two statistical models for the measurement residual. First, the definition of the measurement residual is

$$\boldsymbol{r}(t_i) = \boldsymbol{z}(t_i) - \boldsymbol{H}(t_i)\hat{\boldsymbol{x}}(t_i^-) \tag{2.48}$$

where $\boldsymbol{r}(t_i)$ is the measurement residual, $\boldsymbol{z}(t_i)$ is the measurement from the sensor, $\boldsymbol{H}(t_i)$ is the measurement matrix, and $\hat{\boldsymbol{x}}(t_i^-)$ is the filter state estimate just before the measurement update is applied. Equation (2.49) states that the expected value or mean of the measurement residual $\boldsymbol{r}(t_i)$ should be zero.

$$E\{\boldsymbol{r}(t_i)\} = \boldsymbol{0} \tag{2.49}$$

Equation (2.50) states the covariance of the measurement residual $\boldsymbol{r}(t_i)$ should match the measurement residual covariance

$$E\{\boldsymbol{r}(t_i)\boldsymbol{r}^T(t_i)\} = \boldsymbol{H}(t_i)\boldsymbol{P}(t_i^-)\boldsymbol{H}^T(t_i) + \boldsymbol{R}(t_i) \qquad (2.50)$$

where the measurement residual covariance is comprised of the measurement matrix $\boldsymbol{H}(t_i)$, the filter covariance before the measurement update is $\boldsymbol{P}(t_i^-)$, and the sensor model uncertainty is $\boldsymbol{R}(t_i)$. The subsequent paragraphs present two applications of the statistical measurement residual model.

The first application of the statistical models is detection of a sensor failure. A likelihood function with a moving window based on the N most recent measurement residuals is shown in Equation (2.51) [16]

$$L_{Nk}(t_i) = c_k(t_i) - \frac{1}{2} \sum_{j=i-N+1}^{i} \frac{r_k^2(t_j)}{\sigma_k^2(t_j)} \qquad (2.51)$$

where $c_k(t_i)$ is a slowly varying negative value uncorrelated with the measurement residual, N determines the length of the likelihood function window, $r_k^2(t_j)$ is the covariance of the measurement residual, and $\sigma_k^2(t_j)$ is the kth diagonal term of the residual covariance defined in Equation (2.50). The output of the likelihood function $L_{Nk}(t_i)$ is compared against a threshold value. The likelihood function value becomes more negative when either the measurement residual incurs a bias or the covariance increases significantly. A significant increase in covariance is characterized by measurement covariances beyond 3-σ of the sensor model uncertainty.

The second application consist of applying a threshold against the covariance statistic. If the covariance of the current measurement residual exceeds 3-σ of the sensor model uncertainty it is rejected and no measurement update occurs. This method is used in this thesis to help reduce error introduced by outlier radio range measurements. Equation (2.52) presents the logic comparison

$$\text{Measurement Decision} = \begin{cases} \text{Accept} & r^2(t_i) < (3\sigma)^2 \\ \text{Reject} & r^2(t_i) \geq (3\sigma)^2 \end{cases} \qquad (2.52)$$

where $r^2(t_i)$ is the square of the current residual and $(3\sigma)^2$ is the rejection threshold. The variable σ is defined by the sensor model uncertainty. Measurements with covariances greater than 3-σ are generally considered unacceptable. This algorithm provides rejection of measurements with very high uncertainties. However, if the Kalman filter diverges, large measurement residuals occur and measurements that should be used to correct the divergence will be rejected based on the hard rejection threshold. The adaptive Kalman filter algorithms presented in the next two sections contain methods to deal with high measurement residuals without completely rejecting sensor measurements.

2.9.2 Sage-Husa Algorithm. As mentioned in the previous section, radio range measurements contain varying uncertainty dependent on time-synchronization and the RF environment. The AKF enables estimation of the vehicle and sensor model uncertainty during filter operation. As the uncertainty in the radio measurements increase, the AKF increases the EKF radio model uncertainty. However, the AKF does not account for the non-zero mean of the range error, which dictates the need for a more advanced adaptive algorithm.

The Sage-Husa adaptive algorithm presents an algorithm where the first two moments (mean and variance) of the errors may be estimated for both the vehicle dynamics and sensor models [17, 22, 28]. The Sage-Husa algorithm performs a time-history average of the mean and variance calculations to smooth the estimation. Unlike the AKF, Sage-Husa requires storage of only the last mean and variance estimate, significantly reducing computer storage requirements. The Sage-Husa algorithm operates without the long summation operations present in the AKF, further reducing the computation resource requirements. This section continues with presentation of the Sage-Husa adaptive algorithm and then the implementation equations necessary for inclusion into a Kalman filter.

2.9.2.1 Estimation Algorithm. This section presents the Sage-Husa algorithm equations for the sensor model error and then for the vehicle dynamics

42

model error. For the sensor model, $\hat{\boldsymbol{r}}(t_i)$ contains the estimated mean and $\hat{\boldsymbol{R}}(t_i)$ contains the estimated variance of the sensor model error. Equation (2.53) presents the estimation of the mean of the sensor model error [28]

$$\hat{\boldsymbol{r}}(t_{i+1}) = (1 - d)\hat{\boldsymbol{r}}(t_i) + d[\boldsymbol{z}(t_{i+1}) - \boldsymbol{H}(t_{i+1})\hat{\boldsymbol{x}}(t_{i+1}^-)] \tag{2.53}$$

where $\hat{\boldsymbol{r}}(t_{i+1})$ is the new estimated mean of the sensor model error, the scalar d controls the weight placed on the new mean estimates, $\hat{\boldsymbol{r}}(t_i)$ is the previous estimated mean of the sensor model error, $\boldsymbol{z}(t_{i+1})$ is the sensor measurement, $\boldsymbol{H}(t_{i+1})$ is the measurement matrix, and $\hat{\boldsymbol{x}}(t_{i+1}^-)$ is the current filter state estimate. The computation $\boldsymbol{H}(t_{i+1})\hat{\boldsymbol{x}}(t_{i+1}^-)$ presents the expected measurement. Subtraction of the expected measurement from the sensor measurement $\boldsymbol{z}(t_{i+1})$ returns the measurement residual or error in the expected measurement. The average of the measurement residual provides an estimate of the mean of the sensor model error.

Estimation of the variance or second moment of the measurement residual for the sensor model error is performed in two steps. First, the estimated mean is removed from the measurement residual as shown in Equation (2.54)

$$\tilde{\boldsymbol{z}}(t_{i+1}) = \boldsymbol{z}(t_{i+1}) - \boldsymbol{H}(t_{i+1})\hat{\boldsymbol{x}}(t_{i+1}^-) - \hat{\boldsymbol{r}}(t_{i+1}) \tag{2.54}$$

where $\tilde{\boldsymbol{z}}(t_{i+1})$ is the estimate of the zero-mean measurement residual, $\boldsymbol{z}(t_{i+1})$ is the sensor measurement, $\boldsymbol{H}(t_{i+1})$ is the measurement matrix, $\hat{\boldsymbol{x}}(t_{i+1}^-)$ is the current filter state estimate, and $\hat{\boldsymbol{r}}(t_{i+1})$ is the average mean of the sensor model error. Next, Equation (2.55) presents computation of the variance, or uncertainty, of the sensor model

$$\hat{\boldsymbol{R}}(t_{i+1}) = (1 - d)\hat{\boldsymbol{R}}(t_i) + d[\tilde{\boldsymbol{z}}(t_{i+1})\tilde{\boldsymbol{z}}(t_{i+1})^T - \boldsymbol{H}(t_{i+1})\boldsymbol{P}(t_{i+1}^-)\boldsymbol{H}(t_{i+1})^T] \tag{2.55}$$

where $\hat{\boldsymbol{R}}(t_{i+1})$ is the new estimated variance of the sensor model error, the scalar d controls the weight placed on the new mean estimates, $\hat{\boldsymbol{R}}(t_i)$ is the previous estimated variance of the sensor model error, $\tilde{\boldsymbol{z}}(t_{i+1})$ is the estimate of the zero-mean measurement residual, $\boldsymbol{H}(t_{i+1})$ is the measurement matrix, and $\boldsymbol{P}(t_{i+1}^-)$ is the current filter uncertainty. The computation $\tilde{\boldsymbol{z}}(t_{i+1})\tilde{\boldsymbol{z}}(t_{i+1})^T$ presents the uncertainty of the current measurement update. The computation $\boldsymbol{H}(t_{i+1})\boldsymbol{P}(t_{i+1}^-)\boldsymbol{H}(t_{i+1})^T$ presents the expected variance of the current measurement update. Subtraction of the actual and expected variance presents the error in the previous uncertainty $\hat{\boldsymbol{R}}(t_i)$ of the measurement model error. This error is used to correct the sensor model uncertainty. The Sage-Husa algorithm for the vehicle dynamics model is presented next.

For the vehicle dynamics model, $\hat{\boldsymbol{q}}(t_i)$ contains the estimated mean and $\hat{\boldsymbol{Q}}_d(t_i)$ contains the estimated variance of the vehicle dynamics model error. Equation (2.56) presents the estimation of the mean of the vehicle dynamics model

$$\hat{\boldsymbol{q}}(t_{i+1}) = (1-d)\hat{\boldsymbol{q}}(t_i) + d[\hat{\boldsymbol{x}}(t_{i+1}^+) - \boldsymbol{\Phi}(t_{i+1},t_i)\hat{\boldsymbol{x}}(t_i^+)] \qquad (2.56)$$

where $\hat{\boldsymbol{q}}(t_{i+1})$ is the new estimated mean of the vehicle dynamics model error, the scalar d controls the weight placed on the new mean estimates, $\hat{\boldsymbol{q}}(t_i)$ is the previous estimated mean of the vehicle dynamics model error, $\hat{\boldsymbol{x}}(t_{i+1}^+)$ current filter state estimate, $\boldsymbol{\Phi}(t_{i+1},t_i)$ is the state transition matrix, and $\hat{\boldsymbol{x}}(t_i^+)$ is the previous filter state estimate. The computation $\hat{\boldsymbol{x}}(t_{i+1}^+) - \boldsymbol{\Phi}(t_{i+1},t_i)\hat{\boldsymbol{x}}(t_i^+)$ presents the small change or perturbation in the state estimate. The time-history average performed on this perturbation provides an estimate of the mean of the vehicle dynamics model error. Next, estimate of the variance of the vehicle model error is presented.

Equation (2.57) shows the estimate of the variance of the vehicle dynamics model error

44

$$\hat{\boldsymbol{Q}}_d(t_{i+1}) = (1-d)\hat{\boldsymbol{Q}}_d(t_i) + d[\boldsymbol{K}(t_{i+1})\tilde{\boldsymbol{z}}(t_{i+1})\tilde{\boldsymbol{z}}(t_{i+1})^T\boldsymbol{K}(t_{i+1})^T$$
$$+\boldsymbol{P}(t_{i+1}^+) - \boldsymbol{\Phi}(t_{i+1}, t_i)\boldsymbol{P}(t_i^+)\boldsymbol{\Phi}(t_{i+1}, t_i)^T] \tag{2.57}$$

where $\hat{\boldsymbol{Q}}_d(t_{i+1})$ is the new estimated variance of the vehicle dynamics model error, the scalar d controls the weight placed on the new mean estimates, $\hat{\boldsymbol{Q}}_d(t_i)$ is the previous estimated variance of the vehicle dynamics model error, $\boldsymbol{K}(t_{i+1})$ is the Kalman gain, $\tilde{\boldsymbol{z}}(t_{i+1})$ is the estimate of the zero-mean measurement residual, $\boldsymbol{P}(t_{i+1}^+)$ is the current filter uncertainty, $\boldsymbol{\Phi}(t_{i+1}, t_i)$ is the state transition matrix, and $\boldsymbol{P}(t_i^+)$ is the previous filter uncertainty.

The measurement residual variance $\tilde{\boldsymbol{z}}(t_i)\tilde{\boldsymbol{z}}(t_i)^T$ is pre and post-multiplied by the Kalman gain $\boldsymbol{K}(t_i)$ to obtain the state perturbation uncertainty. This constitutes the measured variance of the vehicle dynamics model error. The computation of

$$\boldsymbol{P}(t_i^-) - \boldsymbol{\Phi}(t_i, t_{i-1})\boldsymbol{P}(t_{i-1}^+)\boldsymbol{\Phi}(t_i, t_{i-1})^T \tag{2.58}$$

gives the expected variance of the vehicle dynamics model error. Subtraction of the measured and expected variance presents the error in the previous vehicle dynamics model uncertainty $\hat{\boldsymbol{Q}}_d(t_i)$. This error is used to correct the estimated variance of the vehicle dynamics model error. The corrected variance estimate, $\hat{\boldsymbol{Q}}_d(t_{i+1})$, is used as the new vehicle dynamics model uncertainty. The next section covers implementation of Sage-Husa algorithm in the time propagation and measurement update Kalman filter steps.

2.9.2.2 Kalman Filter Implementation. The previous section presents the algorithms to estimate the mean and variance of the vehicle dynamics and sensor model errors. Application of these estimates within the Kalman filter is presented next. The two equations comprising time propagation step are presented first.

Equation (2.59) presents correction of the mean error in the state vector propagation [28]

$$\hat{\boldsymbol{x}}(t_{i+1}^-) = \boldsymbol{\Phi}(t_{i+1}, t_i)\hat{\boldsymbol{x}}(t_i^+) + \hat{\boldsymbol{q}}(t_i) \tag{2.59}$$

where $\hat{\boldsymbol{x}}(t_{i+1}^-)$ is the new filter state estimate corrected with the average mean of the vehicle dynamics model error, $\boldsymbol{\Phi}(t_{i+1}, t_i)$ is the state transition matrix, $\hat{\boldsymbol{x}}(t_i^+)$ is the current state estimate, and $\hat{\boldsymbol{q}}(t_i)$ is the estimated mean of the vehicle dynamics model error. The addition of estimated mean $\hat{\boldsymbol{q}}(t_i)$ as opposed to subtraction is due to the subtraction

$$\hat{\boldsymbol{x}}(t_{i+1}^+) - \boldsymbol{\Phi}(t_{i+1}, t_i)\hat{\boldsymbol{x}}(t_i^+) \tag{2.60}$$

performed in Equation (2.56). The sign convention is chosen to reduce the error of the mean in the state estimate.

Equation (2.61) presents the corrected filter uncertainty propagation [28]

$$\boldsymbol{P}(t_{i+1}^-) = \boldsymbol{\Phi}(t_{i+1}, t_i)\boldsymbol{P}(t_i^+)\boldsymbol{\Phi}(t_{i+1}, t_i)^T + \boldsymbol{G}_d\hat{\boldsymbol{Q}}_d(t_{i+1})\boldsymbol{G}_d^T \tag{2.61}$$

where $\boldsymbol{P}(t_{i+1}^-)$ is the new filter uncertainty, $\boldsymbol{\Phi}(t_{i+1}, t_i)$ is the state transition matrix, $\boldsymbol{P}(t_i^+)$ is the current filter uncertainty, $\boldsymbol{G}_d$ is the noise matrix, and $\hat{\boldsymbol{Q}}_d(t_{i+1})$ is the estimated vehicle dynamics model uncertainty. The measurement update step is presented next.

Three equations comprise the measurement update algorithm. First, the Kalman gain is computed in Equation (2.62)

$$\boldsymbol{K}(t_{i+1}) = \boldsymbol{P}(t_{i+1}^-)\boldsymbol{H}^T(t_{i+1})[\boldsymbol{H}(t_{i+1})\boldsymbol{P}(t_{i+1}^-)\boldsymbol{H}^T(t_{i+1}) + \hat{\boldsymbol{R}}(t_{i+1})]^{-1} \tag{2.62}$$

where $\boldsymbol{K}(t_{i+1})$ is the Kalman gain, $\boldsymbol{P}(t_{i+1}^-)$ is the current filter uncertainty, $\boldsymbol{H}^T(t_{i+1})$ is the measurement matrix, and $\hat{\boldsymbol{R}}(t_{i+1})$ is the estimated sensor model uncertainty. Second, Equation (2.63) shows the update of the filter states [28]

$$\hat{\boldsymbol{x}}(t_{i+1}^+) = \hat{\boldsymbol{x}}(t_{i+1}^-) + \boldsymbol{K}(t_{i+1})[\boldsymbol{z}(t_{i+1}) - \boldsymbol{H}(t_{i+1})\hat{\boldsymbol{x}}(t_{i+1}^-) - \hat{\boldsymbol{r}}(t_{i+1})] \qquad (2.63)$$

where $\hat{\boldsymbol{x}}(t_{i+1}^+)$ is the new state estimate, $\hat{\boldsymbol{x}}(t_{i+1}^-)$ is the current state estimate, $\boldsymbol{K}(t_{i+1})$ is the Kalman gain, $\boldsymbol{z}(t_{i+1})$ is the sensor measurement, $\boldsymbol{H}(t_{i+1})$ is the measurement matrix, and $\hat{\boldsymbol{r}}(t_{i+1})$ is the estimated mean of the sensor model error. The subtraction of the estimated mean $\hat{\boldsymbol{r}}(t_{i+1})$ provides the zero-mean measurement residual, presented previously in Equation (2.54), to update with filter states.

Last, the filter uncertainty is updated as shown in Equation (2.64)

$$\boldsymbol{P}(t_{i+1}^+) = \boldsymbol{P}(t_{i+1}^-) - \boldsymbol{K}(t_{i+1})\boldsymbol{H}(t_{i+1})\boldsymbol{P}(t_{i+1}^-) \qquad (2.64)$$

where $\boldsymbol{P}(t_{i+1}^+)$ is the new filter uncertainty, $\boldsymbol{P}(t_{i+1}^-)$ is the current filter uncertainty, $\boldsymbol{K}(t_{i+1})$ is the Kalman gain, and $\boldsymbol{H}(t_{i+1})$ is the measurement matrix. The estimate of the sensor model uncertainty is used in Equation (2.62) to compute the Kalman gain. Through the Kalman gain, the sensor model uncertainty estimate effects the filter uncertainty update shown in Equation (2.64).

The topics presented in this background chapter prepare the reader to understand the specific application of coordinate frames, Kalman filtering, sensor models, statistical analysis, and adaptive filtering which follow in the subsequent chapters. Chapter III presents the navigation system which uses an EKF and associated models to estimate navigation trajectories. Chapter IV contains the results and statistical analysis from several data collections conducted to evaluate the performance of the navigation system.

III. Methodology

The purpose of the radio range measurement is to constrain the drift present in the INS when GPS is not available. To ascertain the trajectory-drift constraint capability of the DH500 radio system, a sensor platform is created and a set of data collects are performed. The EKF post-processing implementation and sensor platform are detailed in Section 3.1. Each of the indoor and outdoor data collects are detailed in Section 3.2.

3.1 Navigation System

The navigation system consists of a sensor platform and post-processing algorithms used to compute the navigation trajectory. Section 3.1.1 covers the placement and configuration for each sensor. Section 3.1.2 presents the EKF update models for each sensor along with the specific post-processing algorithms used to obtain the navigation solution.

3.1.1 Sensor Platform. The sensor platform anchors the sensor suite used in this thesis and defines a position and orientation for each sensor relative to the sensor platform's b-frame. The sensor suite used in this thesis consists of an HG1700 tactical-grade INS [19], DH500 radio system, a stereo-camera imaging system [26], and the SPAN differential GPS (DGPS) receiver which provides centimeter-level positioning accuracy.

Figure 3.1 presents the physical layout of the sensor used in this thesis. Two of the DH500 radios are set at DGPS-surveyed locations. These stationary radios are labeled base station 1 (BS1) and base station 2 (BS2). The third radio, labeled mobile station (MS), is attached to the sensor platform. The range measurements between each BS-MS radio pair are labeled r_1 and r_2. The INS, stereo-camera imaging system, and DGPS receiver are also attached to the sensor platform. A barometer is simulated by corrupting truth data from the DGPS for the outdoor data collections and from the
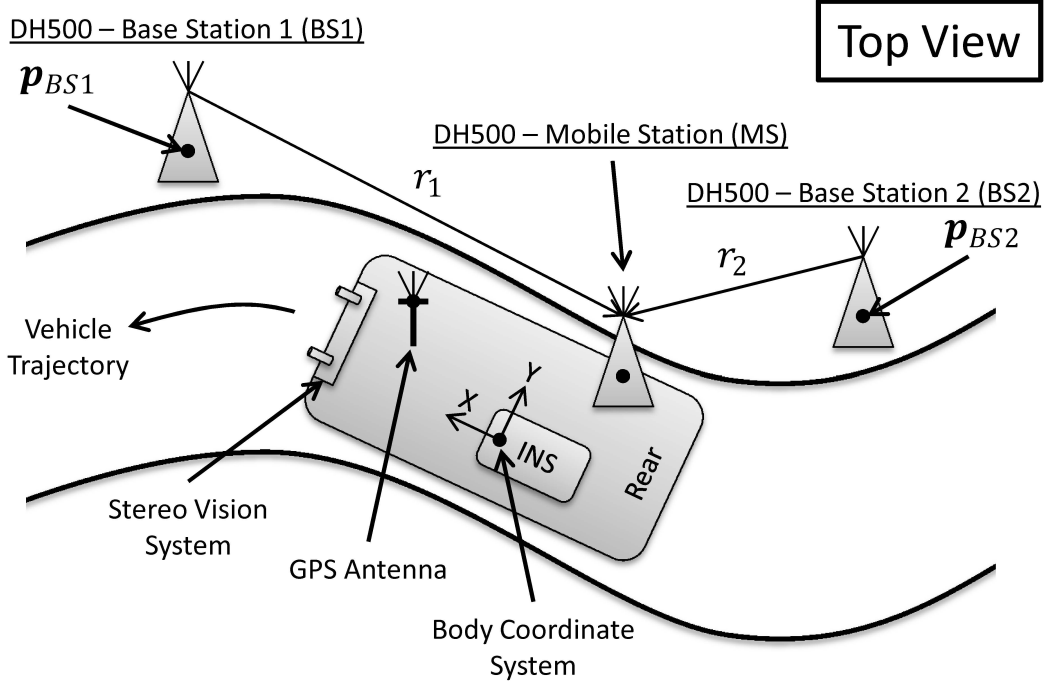
Figure 3.1: Overview of Navigation System Setup. Note the two stationary DH500 radios BS1 and BS2 provide slant range measurements r_1 and r_2 for constraint of the navigation drift.

height of the sensor platform above surveyed markers for the indoor data collections. The simulated barometer data is used to constrain vertical navigation axis drift.

Figure 3.2 illustrates the vectors and DCMs which define each sensor's position and orientation relative to the sensor platform b-frame. The origin of the b-frame is defined to coincide with the origin of the INS s-frame. Also, the orientation of the INS is rotated to align with the b-frame. These INS definitions simplify the navigation trajectory calculations. The position and orientation of the GPS antenna is defined as $\boldsymbol{l}_{bs_G}$ and $\boldsymbol{C}_b^{s_G}$, where the subscript bs_G indicates a vector in the b-frame pointing to the GPS antenna s-frame. Each camera has a separate position and orientation. The variables $\boldsymbol{l}_{bs_{C1}}$ and $\boldsymbol{C}_b^{s_{C1}}$ contain the position and orientation for camera 1. For camera 2, $\boldsymbol{l}_{bs_{C2}}$ and $\boldsymbol{C}_b^{s_{C2}}$ contain the position and orientation. The position and orientation of the MS radio is contained in $\boldsymbol{l}_{bs_{MS}}$ and $\boldsymbol{C}_b^{s_{MS}}$

The data from each sensor are stored on laptop computers also located on the sensor platform. After the data collections, the sensor data are transfered to larger,

49
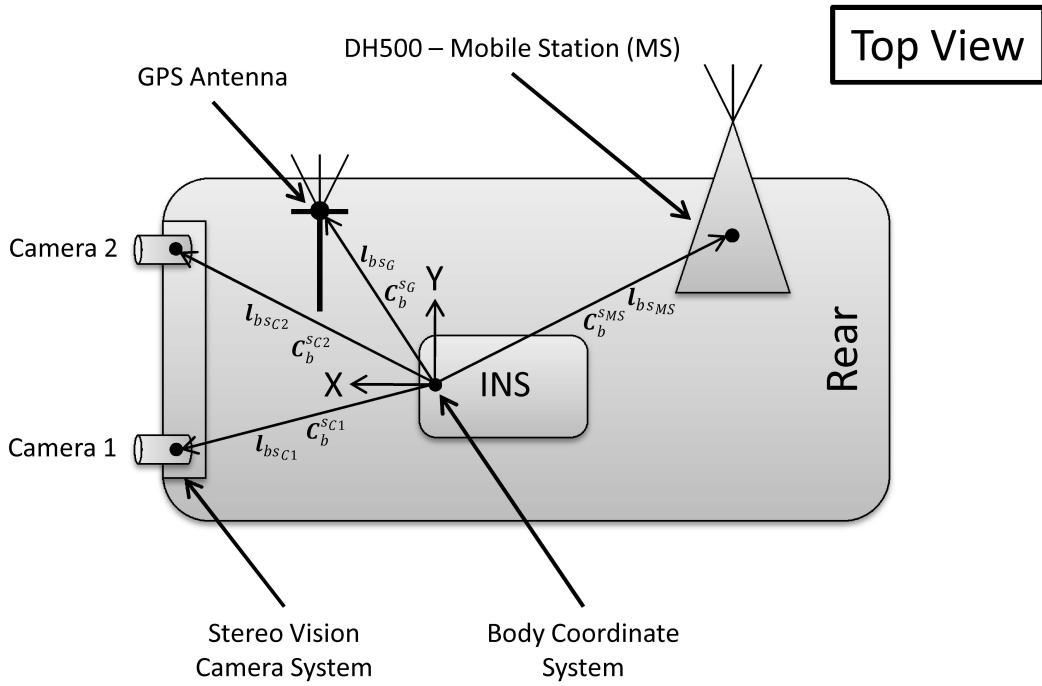
Figure 3.2: Position & Orientation of Mobile Sensors on Vehicle. A location vector $\boldsymbol{l}_b$ and orientation DCM $\boldsymbol{C}_b^s$ is defined for each sensor relative to the b-frame. The INS sensor s-frame origin is defined to be the origin of the b-frame and INS s-frame orientation is defined to align with the b-frame.

more powerful computers to conduct post-processing through the EKF and associated sensor models which are covered in the next section.

Before each data collection, the sensor platform must be configured. The DH500 radio system has two frequency ranges: 400MHz and 900MHz. Observations from initial tests of the DH500 radio system show the 900MHz band provides less noisy slant range measurements. This observation may be due to 400MHz interference in the local area.

The camera system requires the focus of each lens to be set for the focal depth of the features to be tracked in the target environment. The cameras are focused closer for the indoor environment and farther away for the outdoor environment. A camera calibration must be performed when the focus setting on the cameras is changed to capture the shift in non-linear lens distortions.

The tactical-grade HG1700 INS is connected to the SPAN DGPS receiver to aid the GPS position solution [19]. The DGPS system requires the INS be aligned prior to sensor platform movement [18]. The INS-aided DGPS position solution from the SPAN provides position, velocity, and attitude data. This data is used as a "truth" data source for the outdoor data collection to compare against the EKF post-process trajectory.

3.1.2   EKF Implementation.   The data collected from the sensor platform are post-processed through an EKF to obtain the estimation of the navigation system trajectory. The EKF implementation used in this thesis extends the vision-aided navigation (VAN) system developed by Veth [26]. The VAN system consists of tight integration of INS and stereo camera system data. The details and models used to implement the VAN system are contained in [26]. The EKF baro-altitude model used to constrain the vertical navigation channel drift and EKF radio range model used to constrain the drift in the horizontal navigation channels are presented in later subsections.

Equation (3.1) presents the states estimated by the EKF

51

$$\delta\hat{\boldsymbol{x}} = \begin{bmatrix} \delta\boldsymbol{p}^n \\ --- \\ \delta\boldsymbol{v}^n \\ --- \\ \boldsymbol{\psi} \\ --- \\ \boldsymbol{a}^b \\ --- \\ \boldsymbol{g}^b \\ --- \\ h \end{bmatrix}_{16\times 1} \tag{3.1}$$

where $\delta\boldsymbol{p}^n$ and $\delta\boldsymbol{v}^n$ contain the error in position and velocity, $\boldsymbol{\psi}$ contains the attitude of the sensor platform, $\boldsymbol{a}^b$ and $\boldsymbol{g}^b$ contain the bias estimates for the accelerometers and gyroscopes, and h contains the estimate of the baro-altitude aiding bias. The super-script n indicates the n-frame is used as the frame of reference.

3.1.2.1 Baro-Altitude Model. The barometer provides measurements of air pressure which correlate to the altitude of the barometer as presented in Section 2.7. The baro-altitude EKF measurement update model is used to constrain the INS drift present in the vertical navigation channel. Vertical channel information is pulled from the DGPS truth data for the outdoor data collections. For the indoor data collections the height of the sensor platform above the surveyed indoor markers is used for the vertical channel information. The next paragraphs present the EKF baro-altitude model.

The model presented assumes the baro-altitude aiding measures vertical axis position of the sensor platform in the n-frame. The baro-altitude measurements are modeled as the true vertical axis position plus white, Gaussian noise and a time-varying bias. Equation (3.2) presents the model

$$\tilde{p}_d^n(t) = p_d^n(t) + w_B(t) + h(t) \tag{3.2}$$

where $p_d^n(t)$ is the true vertical position, $w_B(t)$ is the white noise of strength σ_B^2, $h(t)$ is the barometer bias estimated by the EKF, and $\tilde{p}_d^n(t)$ is the corrupted vertical axis measurement. For the true vertical position $p_d^n(t)$, the superscript n indicates the n-frame and the subscript d indicates the *down*-axis of the NED n-frame.

The vertical axis measurement $\delta\tilde{p}_d^n(t)$ correlates directly to the $\hat{p}_d^n(t)$ system state estimate error. Equation (3.3) presents the measurement matrix in terms of the EKF system states.

$$H(t_i) = \begin{bmatrix} 0 & 0 & 1 & 0 & \cdots & 0 & 1 \end{bmatrix} \tag{3.3}$$

The final EKF measurement model for baro-altitude aiding is presented in Equation (3.4)

$$\delta\hat{z}(t_i) = \begin{bmatrix} 0 & 0 & 1 & 0 & \cdots & 0 & 1 \end{bmatrix}\delta\hat{\boldsymbol{x}}(t_i^-) + v_b(t_i) \tag{3.4}$$

where $\hat{z}(t_i)$ is the estimated measurement, $\hat{\boldsymbol{x}}(t_i^-)$ is the current EKF state estimate, and $v_b(t_i)$ is the measurement noise strength defined by σ_b^2.

As mentioned in Section 3.1.1, the EKF baro-altitude aiding model is not used to include real barometer information, but to incorporate slightly corrupted truth data to constrain the drift of the vertical navigation axis to sub-meter levels. The uncertainty of the EKF baro-altitude model is set to 0.1 meters. The vertical channel truth data from the DGPS for the outdoor collects and surveyed floor markers for the indoor collects are corrupted with white, Gaussian noise of strength $\sigma_b = 0.1$.

3.1.2.2 DH500 Radio Model. The slant range measurements provided by the DH500 radio system contains information about the position of the sensor platform. This correlates to the position states of the EKF state vector. The range

error is modeled as the true range corrupted with white Gaussian noise. Equation (3.5) presents the model

$$\tilde{r}(t) = r(t) + v_R(t) \tag{3.5}$$

where the slant range provided by the DH500 is $\tilde{r}(t)$, the true slant range is $r(t)$, and the white Gaussian noise source describing the uncertainty of the measurement is $v_R(t)$ with strength σ_R^2. The value chosen for σ_R^2 is determined from the RMS range error collected from the stationary data collections.

The first step is to model the slant range measurement in terms of the EKF position states. Equation (3.6) shows the computation of the true slant ranges

$$\boldsymbol{r}(t) = \begin{bmatrix} r_1(t) \\ r_2(t) \end{bmatrix} = \begin{bmatrix} |\boldsymbol{p}^n(t) + \boldsymbol{l}_{bs_{MS}}^n - \boldsymbol{p}_{BS1}^n| \\ |\boldsymbol{p}^n(t) + \boldsymbol{l}_{bs_{MS}}^n - \boldsymbol{p}_{BS2}^n| \end{bmatrix} \tag{3.6}$$

where $\boldsymbol{p}^n(t)$ is the position of the sensor platform , $\boldsymbol{l}_{bs_{MS}}^n$ is the position of the MS radio on the sensor platform, and $\boldsymbol{p}_{BS1}^n$ and $\boldsymbol{p}_{BS2}^n$ are the positions of the ground radios BS1 and BS2. These truth computations are performed in the n-frame.

The uncertainty of each of the slant range measurements is defined by two independent, white Gaussian noise sources $\boldsymbol{v}_R(t)$. Equation (3.7) presents the vector of noise sources

$$\boldsymbol{v}_R(t) = \begin{bmatrix} v_1(t) \\ v_2(t) \end{bmatrix} \tag{3.7}$$

where the strength of each noise source is defined by σ_{R1}^2 and σ_{R2}^2. These noise sources are set to the same uncertainty for the EKF radio range model.

The measurement model must be linearized for implementation in the EKF. Equation (3.8) presents the matrix of partial derivatives

$$\boldsymbol{H}[\hat{\boldsymbol{x}}(t_i^-), t_i] = \begin{bmatrix} \frac{\partial r_1}{\partial p_n^n} & \frac{\partial r_1}{\partial p_e^n} & \frac{\partial r_1}{\partial p_d^n} & 0 \cdots \\ \frac{\partial r_2}{\partial p_n^n} & \frac{\partial r_2}{\partial p_e^n} & \frac{\partial r_2}{\partial p_d^n} & 0 \cdots \end{bmatrix}_{\hat{\boldsymbol{x}}(t_i^-)} \tag{3.8}$$

where $\frac{\partial r_1}{\partial p_n^n}$ is the partial derivative of the slant range equation between the MS and BS1 with respect to the respect to the *north* (n) axis in the n-frame. The results of the partial derivatives are shown in Equation (3.9) with the denominators k_1 and k_2 shown in Equation (3.10).

$$\boldsymbol{H}[\hat{\boldsymbol{x}}(t_i^-), t_i] = \begin{bmatrix} (\boldsymbol{p}^n(t) + \boldsymbol{l}_{bs_{MS}} - \boldsymbol{p}_{BS1}^n)^T / k_1 & 0 \cdots 0 \\ (\boldsymbol{p}^n(t) + \boldsymbol{l}_{bs_{MS}} - \boldsymbol{p}_{BS2}^n)^T / k_2 & 0 \cdots 0 \end{bmatrix}_{\hat{\boldsymbol{x}}(t_i^-)} \tag{3.9}$$

$$\begin{aligned} k_1 &= |\boldsymbol{p}^n(t) + \boldsymbol{l}_{bs_R} - \boldsymbol{p}_{BS1}^n| \\ k_2 &= |\boldsymbol{p}^n(t) + \boldsymbol{l}_{bs_R} - \boldsymbol{p}_{BS2}^n| \end{aligned} \tag{3.10}$$

Equation (3.11) presents the linearized measurement model

$$\hat{\boldsymbol{z}}(t_i) = \boldsymbol{H}[\hat{\boldsymbol{x}}(t_i^-), t_i]\hat{\boldsymbol{x}}(t_i^-) + \boldsymbol{v}(t_i) \tag{3.11}$$

where the measurement matrix $\boldsymbol{H}[\hat{\boldsymbol{x}}(t_i^-), t_i]$ is re-evaluated about the current state estimate $\hat{\boldsymbol{x}}(t_i^-)$ before each slant range measurement update. This allows non-linearities in the slant range model to be incorporated into the EKF measurement update. The EKF model uncertainty for each of the radio pairs is contained in the measurement noise matrix $\boldsymbol{R}(t_i)$ shown in Equation (3.12).

$$\boldsymbol{R}(t_i) = \begin{bmatrix} \sigma_{R1}^2 & 0 \\ 0 & \sigma_{R2}^2 \end{bmatrix} \tag{3.12}$$

The EKF radio range model presented assumes the error of the slant ranges is zero-mean and white Gaussian in distribution. Analysis presented in Chapter IV reveals the range error has a notable positive bias and the distribution becomes in-

creasingly non-Gaussian as RF interference increases. This violates both EKF radio range model assumptions. To account for the variation in uncertainty of the radio ranges, the residual monitoring technique presented in Section 2.9.1 is applied to the EKF radio range model. A slight improvement is noted in the post-processing trajectory results, but residual monitoring does not account for the non-zero mean of the radio range error.

The residual monitoring method is swapped for a modified implementation of the Sage-Husa adaptive algorithm. Only the measurement-update portion of the Sage Husa algorithm is implemented in the radio range model due to time constraints. As presented in Section 2.9.2, the Sage Husa algorithm estimates the mean of the measurement residual and adjusts the measurement uncertainty $\boldsymbol{R}(t_i)$ as the error in the range measurements change. The Sage-Husa adaptive algorithm and its implementation are covered in Section 2.9.2. The Sage-Husa algorithm must be tuned via its memory factor d.

3.2 Data Collections

Each data collection consists of specific sensor placement and trajectory definition. For stationary data collections, the trajectory consists of a single surveyed location. For moving data collections, the trajectory consists of a predetermined path which the sensor platform follows. The next sections present the data collection setups in the following order: stationary outdoor collection, moving outdoor collection, stationary indoor collections, and moving indoor collections. The stationary data collections proceed the moving data collections to incorporate changes in the EKF radio range model based on the effects of the outdoor and indoor environments on the DH500 radio system performance.

3.2.1 Stationary Outdoor Collect. An outdoor environment with minimal RF interference is chosen to perform the stationary outdoor data collect. Free from obstructions, the DH500 radio system has clear LOS between each radio. This envi-
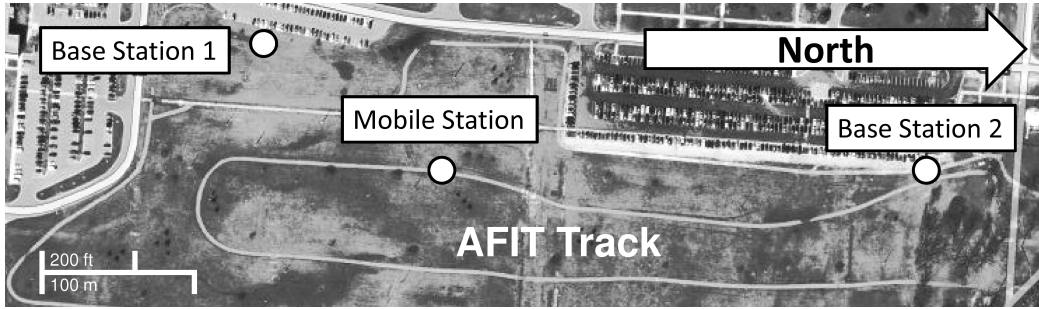
Figure 3.3: Outdoor Stationary Data Collection Setup. The displayed locations of the base stations and mobile station are chosen to provide the clearest LOS and low RF interference between the radios.

ronment allows characterization of the lowest expected radio range error, providing the best expected INS drift constraint capability. Figure 3.3 displays the approximate position of each of the three DH500 radios.

The geometry between the radio positions models a real-world usage application. More ideal radio placement is described by an equilateral triangle. Real-world situations may not always allow for equilateral radio placement. The radio placement produces high position uncertainty in the east-to-west axis. The north-to-south axis has much lower uncertainty due to the wide radio placement.

Once the radios are positioned as approximately shown in Figure 3.3, each radio position is surveyed with the SPAN DGPS receiver. A 10-minute data collection is performed with the laptop computer connected to the radio system providing over 200 data points for each radio pair to characterize the range error of the radios. During post-processing, the true slant range between each radio pair is computed using the DGPS survey data. The slant range measurements collected from the DH500 radio system are subtracted from the true slant ranges to obtain the slant range error. The mean and variance are computed to determine the RMS error of the slant ranges. The RMS error is used to define the uncertainty for the EKF radio range model. To determine whether the distribution of the range error is Gaussian the Chi-Squared statistical test is performed and a multi-bin histogram is generated. Graphs and analysis for the outdoor stationary data collection are presented in Section 4.1.1.
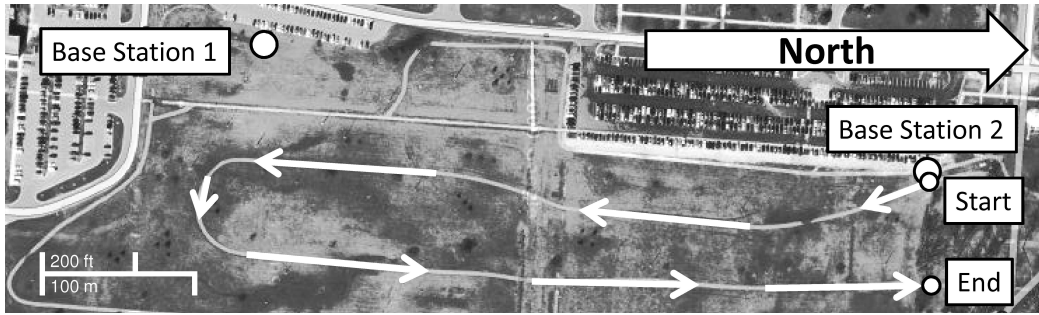
(a) North-South "a"
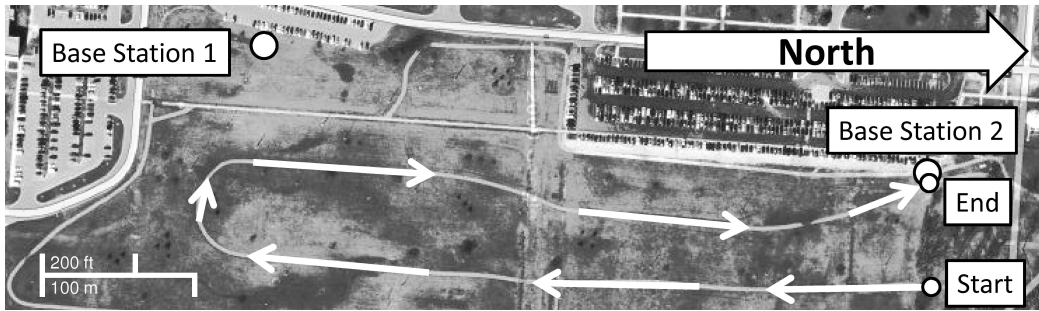
(b) North-South "b"

Figure 3.4: Outdoor Moving Data Collection Setup. The locations of the base stations do not change from the stationary data collection to the moving collection. The sensor platform is moved along the track indicated by the arrows.

3.2.2 Moving Outdoor Collect. To test the INS drift constraint capability of the DH500 radio system, an outdoor moving data collection is performed. The INS, DH500 radio system, stereo-camera image system, and GPS comprise the sensors used for the outdoor moving collect. Prior to the outdoor moving data collections, the SPAN The lenses on the stereo camera system are set to focus on distant objects. Several laptop computers are used to collect data from each of the sensors. Figure 3.4 displays the radio placement and pre-determined trajectory of the sensor platform.

Similar to the outdoor stationary data collection, two of the DH500 radios are positioned at stationary, surveyed locations marked BS1 and BS2. A golf cart is used to transport the sensor platform along the trajectory shown in Figure 3.4 indicated by the white arrows. A total of four data collections are performed. Two data collections follow the trajectory shown in Figure 4(a) are designated with "a." The other two data collections follow the trajectory shown in Figure 4(b) are designated with "b."

58

An incremental approach is taken for post-processing the data. EKF post-processing is conducted first with only INS data. Next, EKF bias estimation is added. To allow the EKF to estimate the bias states, a 2-minute filter alignment is performed with truth data from the SPAN. Next, the radio ranges and corrupted DGPS vertical axis data is added to constrain the drift present in the INS with bias estimation trajectory. The residual monitoring method and Sage-Husa adaptive method are tested separately in the EKF radio range model. This incremental approach ensures each data source is being post-processed correctly before additional data is added. The stereo image data was omitted from post-processing due to a poor camera calibration which was unable to be corrected due to time constraints. Without a good stereo camera calibration, the EKF is not able to properly use the image data due to the lens distortion. Section 4.2 presents the results and analysis for the moving outdoor data collection.

The sensor platform was then placed indoors where RF interference will introduce significant error into the radio range measurements. The post-processing results from the indoor data collections will determine how well the DH500 radio system is able to constrain the INS drift while indoors.

3.2.3 Stationary Indoor Collects. The indoor data collection setup consists of two DH500 radios placed outdoors. The sensor platform consists of the INS, MS radio, and stereo camera system is positioned indoors. Only the radios positioned outside have clear LOS view of each other. The RF signals must now travel through the walls of the building to reach the MS radio located indoors. The building walls reflect the RF signals, generating interference which results in a predominantly positive bias in the range error. The EKF radio model uncertainty must be re-estimated to account for the additional errors now present in the radio range measurements due to increased RF interference. Figure 3.5 illustrates the position of the two DH500 radios placed outside. The positions of the outdoor BS1 and BS2 radios are surveyed with DGPS.

59
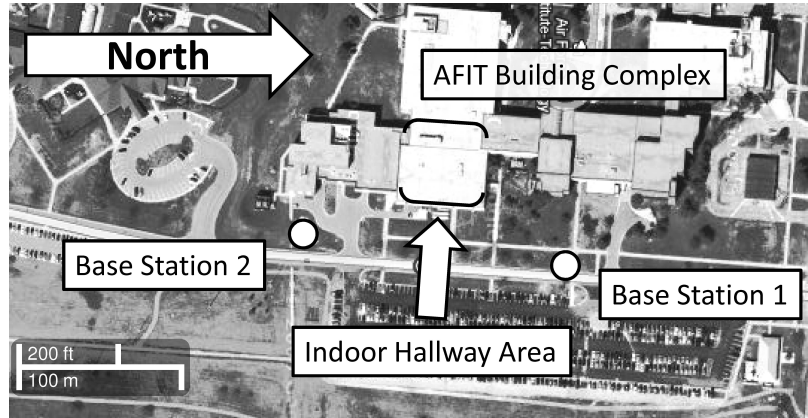
Figure 3.5:   Outdoor Radio Positions for Indoor Data Collections. The position of the outside radios simulate potential locations of radio base stations used in the field. See Figure 3.6 for indoor hallway layout.

Similar to the outdoor data collections, the radio placement is indicative of a real-world application as opposed to the more ideal equilateral placement. This radio placement introduces additional non-idealities into the performance results which are presented in Section 4.1.2 and 4.3.

Figure 3.6 displays the surveyed indoor locations where the third DH500 radio is placed. The static indoor data collections consist of extracting the stationary portions of the indoor moving trajectories presented in the next section. The stationary data sets for the *north* and *south* surveyed point are analyzed in separate groups. The accumulated stationary collection time for each radio pair at the *north* and *south* surveyed points is about eight minutes. This provides over 100 data points for each radio pair. The true slant ranges are computed from the surveyed outdoor radio locations and surveyed indoor points. The true slant range is subtracted from the measured radio ranges obtained from the DH500 radio system to compute the range error. The RMS error calculation from the mean and variance of the range error is used to determine a new uncertainty for the EKF radio range model. Similar to the outdoor stationary data collection, a binned histogram is generated and the Chi Squared test is performed to determine the fit of the range error to the Gaussian distribution. The results from the indoor stationary data collection found in Section 4.1.2.

60
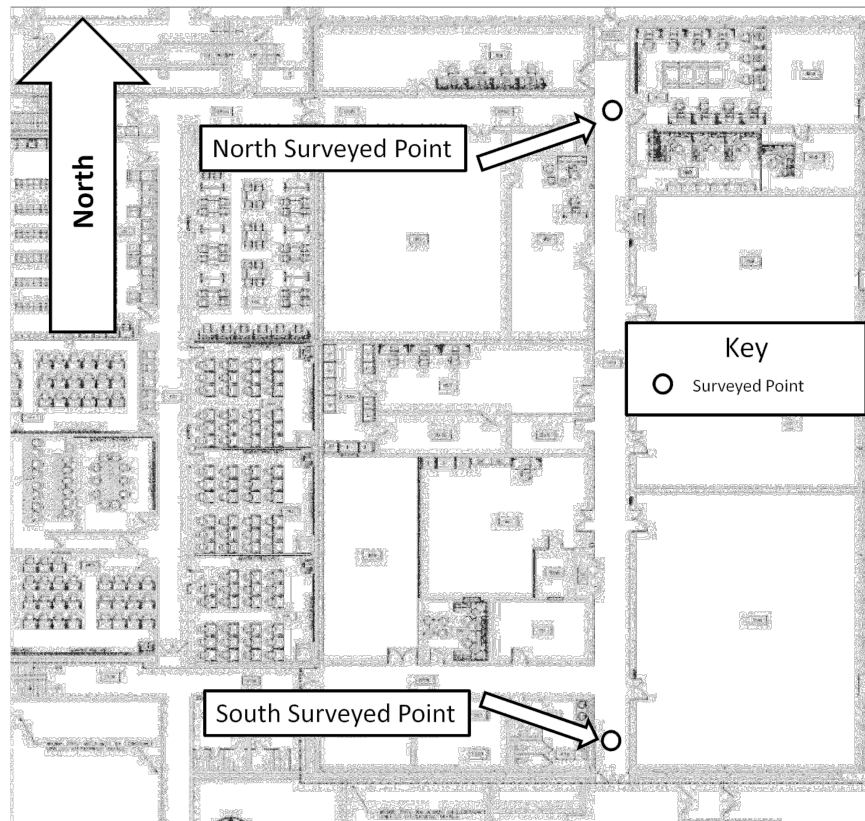
Figure 3.6:   Indoor Hallway Surveyed Locations for Stationary Data Collections. Locations are displayed for *north* and *south* stationary data collections. Note the layers of building walls illustrated by the building layout. These walls attenuate the radio RF signals and reflect the RF signals causing RF interference.

(a) North-South "a"   (b) North-South "b"
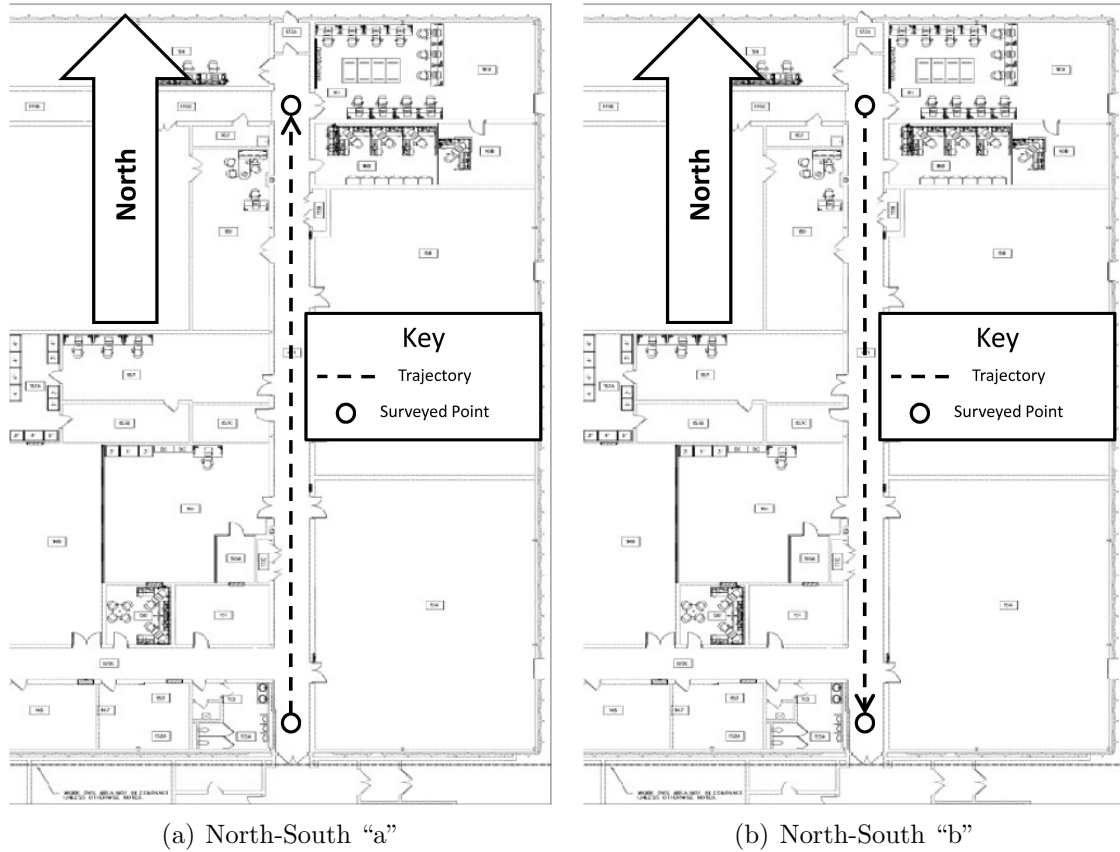
Figure 3.7: North-South Indoor Moving Trajectory Illustration. The surveyed points provide position "truth" data to compare against the EKF post-process indoor trajectory. Note changes in trajectory direction between Figure 3.7 (a) and 3.7 (b) indicated by the black arrow.

3.2.4 Moving Indoor Collects. The results from the stationary indoor data collection show a significant increase in radio range error as will be presented in Section 4.3. This increase in error reduces the ability of the DH500 radio system to constrain the trajectory drift of the INS. Two groups of indoor data collections are performed to evaluate the drift constraint capability of the radio system operating with significant RF interference.

The first group is labeled "North-South." Figure 3.7 presents an overview of for the indoor trajectories contained in the "North-South" group. A total of four separate data collections are performed for the "North-South" group. Data collects

which follow the trajectory direction in Figure 3.7 (a) are designated with "a" and trajectories that follow Figure 3.7 (b) are designated with "b."

Two of the DH500 radios are placed outside as shown previously in Figure 3.5. The indoor sensor platform consists of the INS, the MS DH500 radio, and the stereo camera imaging system. The camera system focus is re-adjusted for the indoor data collections to provide clear focus on objects near the cameras. The indoor trajectory of the sensor platform is illustrated in Figure 3.7. The performance of the sensor platform in this hallway represents the best expected indoor drift-constraint performance of the radio system due to the relatively close proximity to the outdoor radios.

The second indoor data collection consists of moving the sensor platform through the building in a square-shaped trajectory. This data collection is labeled "Square." A variety of walls and doors are brought between the MS indoor radio and the outdoor BS radios. These objects further increase the RF interference. The outdoor radios BS1 and BS2 remain in the same locations as defined in the North-South data collection. The North-South data collection camera focus settings are re-used, negating the need for an additional camera calibration. Figure 3.8 illustrates the square indoor moving trajectory. The sensor platform starts in the Advanced Navigation Technology (ANT) Lab shown in the upper-right hand corner of Figure 3.8 and proceeds clockwise around the square-shaped trajectory. The sensor platform ends back at the start location in the ANT Lab.

EKF post-processing of both the North-South and Square indoor moving data collections proceeds with an incremental approach. First, only the INS data is post-processed. Then EKF bias estimation is enabled. Again, a 2-minute stationary alignment is performed to allow the filter to estimate the bias states. The alignment data is obtained from the SPAN attitude estimate and position is obtained from the starting surveyed floor marker. Next, the radio range and corrupted vertical axis truth data is incorporated. A proper camera calibration is obtained for the indoor lens focus settings. The stereo image data is incorporated last. Analysis of each step of the in-
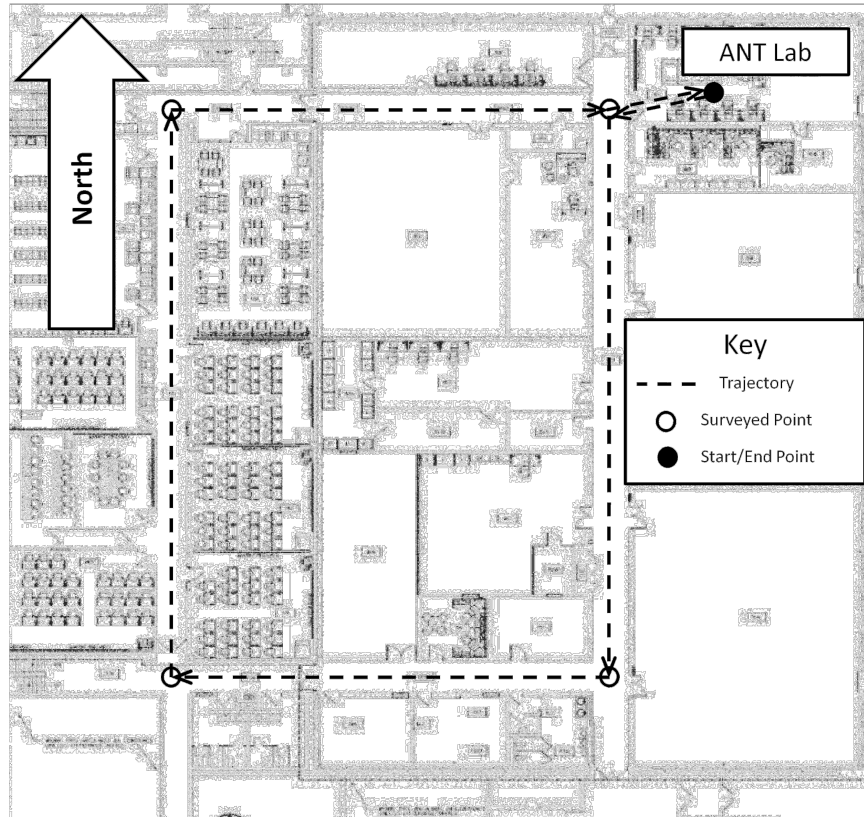
Figure 3.8:   Square Indoor Moving Trajectory Illustration. The square indoor moving trajectory provides variation in RF interference and signal attenuation.

cremental build-up ensures each data set is incorporated correctly and the associated filter parameters are tuned correctly. The Sage-Husa adaptive algorithm is used in the EKF radio range model for all the indoor data collections. Results and analysis for the indoor moving data collections are presented in Section 4.3.

IV. Results

This chapter presents results and analysis for the data collections outlined in Section 3.2. Results from the stationary data collected for both the outdoor and indoor environments are presented in Section 4.1. Then, the results for the outdoor moving data collections are contained in Section 4.2. Section 4.3 contains results for the indoor moving data collections.

4.1   Radio Performance Characterization

This section presents results and analysis for the observed range errors of the DH500 radio system. The purpose of characterization is to measure the uncertainty of the range error. The RMS value of the range error is used as the first value for the radio range model uncertainty. This model uncertainty is then further tuned during residual analysis. Residual analysis will be presented in Sections 4.2 and 4.3 for each data collection environment.

The performance of the radio system is characterized by generating histograms of the range error. The histograms approximate the statistical distribution of the range error. Overlaid on top of the histogram is the plot of a Gaussian distrobution with the same mean and variance as the set of range errors. The Chi-Squared statistical test is applied to each set of range errors for the final determination whether the set of range errors is Gaussian in distribution.

The range measurements between the DH500 radios are referenced in two pairs. Radio pair 1 consists of BS1 and the MS. Radio pair 2 consists of BS2 and the MS. Section 4.1.1 presents the outdoor range characterization. Section 4.1.2 presents the indoor range characterization.

4.1.1   Outdoor Characterization.   The first procedure characterizes the outdoor stationary performance of the DH500 radios. The navigation system is setup as described in Section 3.2.1. Once the position of each radio is surveyed, a 10 minute
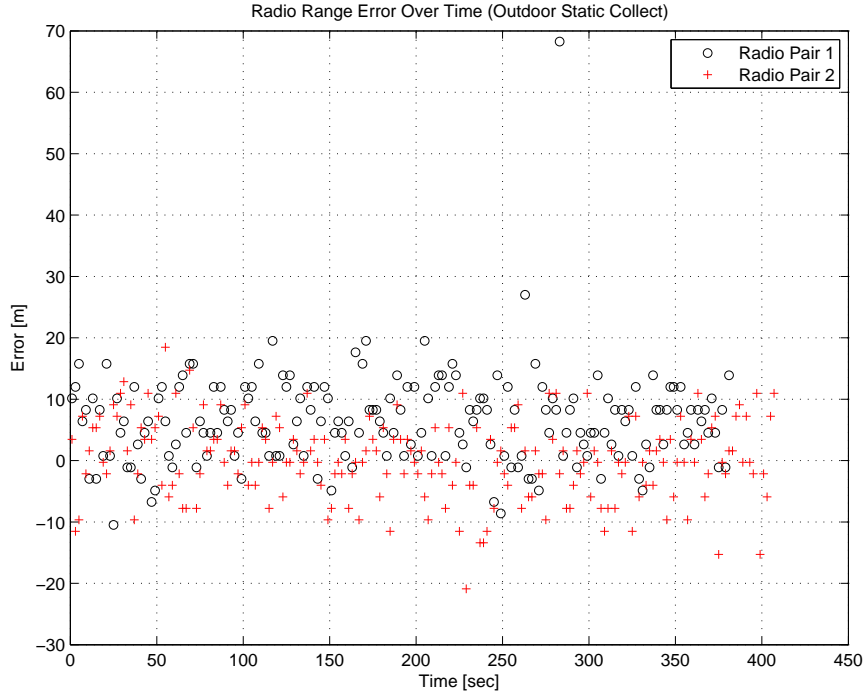
Figure 4.1: Outdoor Range Error Plot. Spread of range errors is due to noise in the range measurement system.

data collection is performed to gather range measurements between each radio pair. The 10 minute data collection provides over 200 range measurements per radio pair.

The raw range errors used in the outdoor characterization are presented in Figure 4.1. The majority of range errors are distributed evenly with a mean of 6.56 meters. The spread of the range errors is due to noise present in the ranging system.

Histograms representing the distribution of radio pairs 1 and 2 are shown in Figures 4.2 and 4.3 respectively. Tables 4.1 and 4.2 present the statistics and Chi Squared GOF results for each set of range error distributions. Analysis of radio pair 1 follows.

Observe the histogram and Gaussian overlay shown in Figure 4.2. Note the long-tailed distribution of the range errors which indicate a non-Gaussian distribution. The observation is confirmed by the Chi Squared GOF test returning a result of *non-Gaussian* presented in Table 4.1. Although only two ranges fall above 25 meter error, the case of extreme outliers must be handled to reduce corruption of the EKF
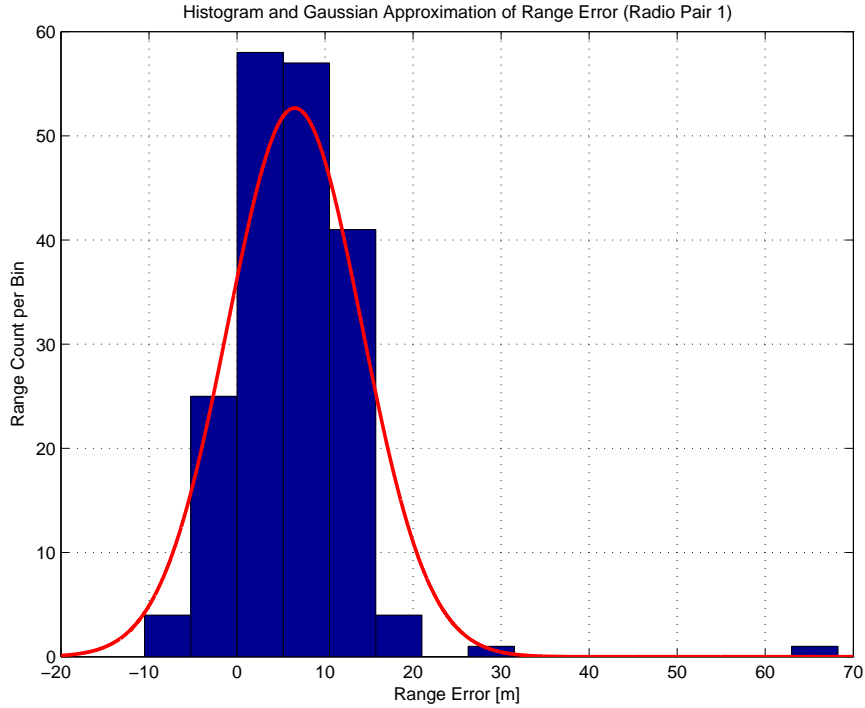
Figure 4.2: Outdoor Range Error Between Radio Pair 1. Note how outliers at 30 and 65 meters create a long-tailed distribution.

estimated trajectory. The mean of the range error data in Table 4.1 presents a bias in the range measurements. Estimation of the range bias within the radio range model is a possible solution to reduce the effects of the bias.

From further experience with the radios it is found that the bias is not constant due to changes in RF interference. The effects of RF interference are present in the outlier range errors shown in Figure 4.2. Next, the distribution of radio pair 2 is presented.

Table 4.1: Statistics for Radio Pair 1 Range Error. The range distribution has a non-zero mean and does not conform to the Gaussian distribution.

Parameter	Value
Mean	6.56 m
Std Dev	7.60 m
RMS Error	10.04 m
Chi Squared Test	Non-Gaussian
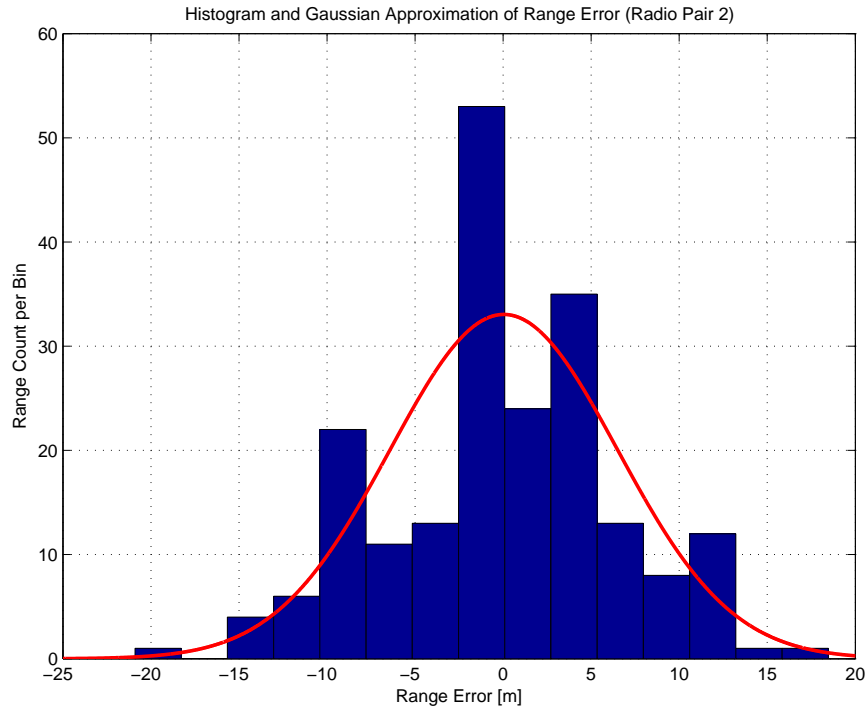
Figure 4.3: Outdoor Range Error Between Radio Pair 2. Note how range error distribution appears to reasonably fit Gaussian overlay.

Figure 4.3 and Table 4.2 present the range error distribution and statistics for radio pair 2. First, note the range error distribution appears to fit the overlaid Gaussian better than radio pair 1. Confirmation of the observation is provided by the result of *Gaussian* from the Chi Squared GOF test. Note also the mean of the distribution is much closer to zero than radio pair 1. The fairly symmetric distribution of range errors around zero meters presents insight into the range error introduced by the radio system itself. RF interference from multipath can add positive range error. Since the range calculation algorithms within the DH500 radio system are proprietary, the exact source of the outlier positive range errors is not known. However, as will be shown for the indoor range error analysis in the next section, excessive RF interference produces predominantly positive range errors for the DH500 radio system. The lack of excessive positive range error indicates a general lack of RF interference for radio pair 2. Figure 4.3 displays the Gaussian-like histogram with a mean of zero and an uncertainty of 6.5 meters.

Table 4.2:   Statistics for Radio Pair 2 Range Error. The range distribution is approximately zero-mean and conforms to the Gaussian distribution.

Parameter	Value
Mean	0.04 m
Std Dev	6.46 m
RMS Error	6.46 m
Chi Squared Test	Gaussian

For the purposes of this thesis, the low RF interference outdoor range characterization presents a lower bound on range errors present in the DH500 radio system. Further analysis of radio range errors is conducted in the next section where results from the stationary indoor range error characterization are presented

4.1.2 Indoor Characterization.   The DH500 radio system is used to aid indoor navigation. This warrants a separate characterization of the range error performance. High RF interference introduced by the indoor environment significantly changes the characteristics of the radio range error.

The graphs that follow show the severe degradation in range measurement performance as the walls and doors of the indoor environment introduce significant RF interference between the radios. The navigation system setup for the stationary indoor data collections is described in Section 3.2.3.

The presentation format of the indoor characterization data follows that of the outdoor characterization. For the indoor analysis, static data collections are performed at two locations within the building. These are differentiated by the labels *north* and *south* in reference to locations in the hallway. First, graphs of the raw range errors between radio pair 1 and 2 are presented. Then histograms of the range error data with overlaid Gaussian approximations are presented and analyzed. Tables with statistics and results of the Chi Squared GOF test for the range error data follow each histogram. Conclusions from the indoor range error analysis are presented at the end of this section.

70
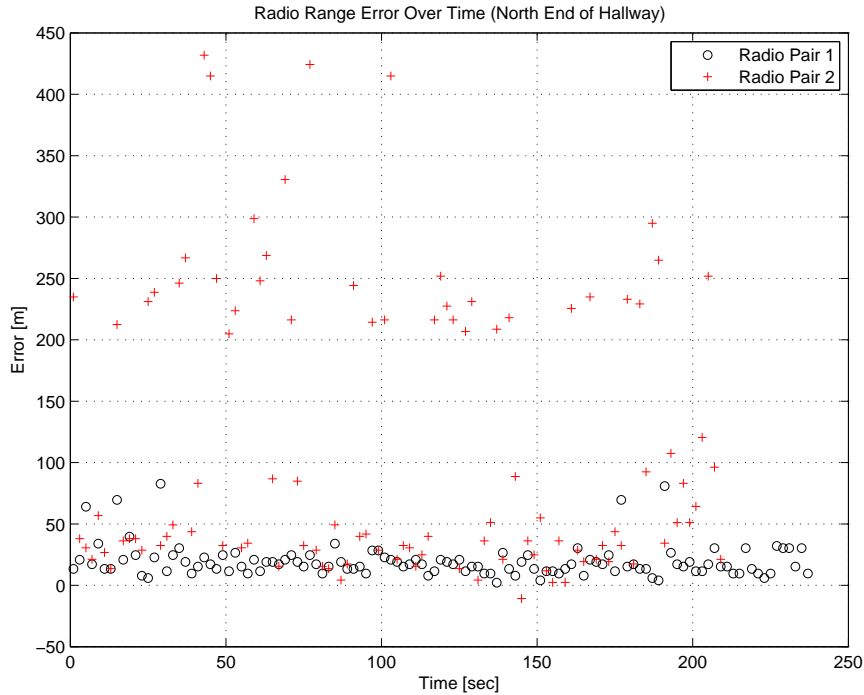
Figure 4.4:   Indoor North Range Error Plot. A large number of extreme outliers exist above 200 meters due to RF channel interference from the building.

Figures 4.4 and 4.5 present the raw range error measurements for the *north* and *south* stationary data sets, respectively. The notable difference when compared with the outdoor data in Figure 4.1 is the large range errors presented by the outliers. This is a prominent display of performance degradation due RF interference.

Figures 4.6 and 4.7 present long-tailed histograms for both radio pairs at the *north* position. The indoor radio MS is located closer to BS1 than BS2. The surveyed distance between MS and BS1 is 76.6 meters and between MS and BS2 is 112.0 meters. The RF channel between radio pair 1 is shorter and, from observation during the data collection, the building presents less interference to the RF channel between these radios. The opposite is true for radio pair 2. Almost the entire width of the building stands between radio pair 2 which provides abundant RF interference. This RF channel difference is apparent in Figures 4.6 and 4.7 by noting the length of the range error histogram tails. The more RF channel interference present, the longer the histogram tail. It is interesting to note the strong presence of range error around

71
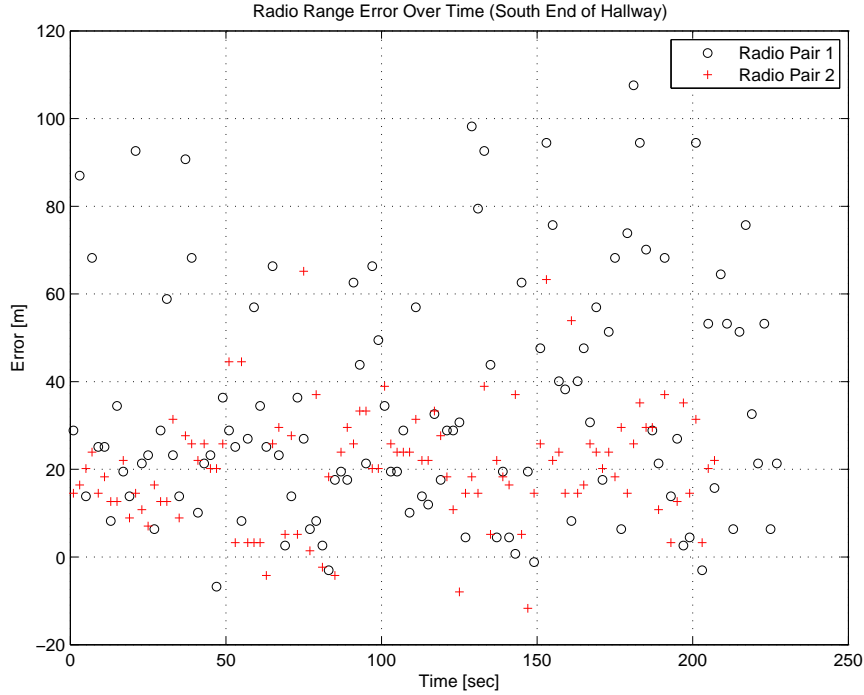
Figure 4.5:   Indoor South Range Error Plot. The ranges are reasonable contained below 100 meters as compared with the extreme outliers shown in Figure 4.4.

225 meters for radio pair 2. This suggests strong RF interference along a trajectory approximately 200 meters longer than the true slant range.

Tables 4.3 and 4.4 present statistics for Figures 4.6 and 4.7 respectively. As noted for the outdoor range error analysis, the bias present in each static collect is different. RF interference introduces the varying range error bias. The RMS error presents a measure of RF interference and uncertainty of the range measurements. The lower level of RF interference present for radio pair 1 radio pair is evident by the lower RMS error of 23.8 meters. Likewise, the 161.1 meter RMS error for radio pair 2 is higher due to significant interference. In both cases, the Chi-Squared test result is *non-Gaussian*. Both radio pairs for the *north* location do not conform to the Gaussian distribution. This means the white, Gaussian noise assumption used in the EKF range update model is not valid.

Figures 4.8 and 4.9 along with Tables 4.5 and 4.6 present the histograms and statistics for both radio pairs at the *south* hallway location. Upon initial inspection

72

Figure 4.6:   Indoor North Range Error Between Radio Pair 1. Note the long tail on the range error distribution due to RF interference.

Figure 4.7:   Indoor North Range Error Between Radio Pair 2. Note the extreme range errors due to RF signal interference.

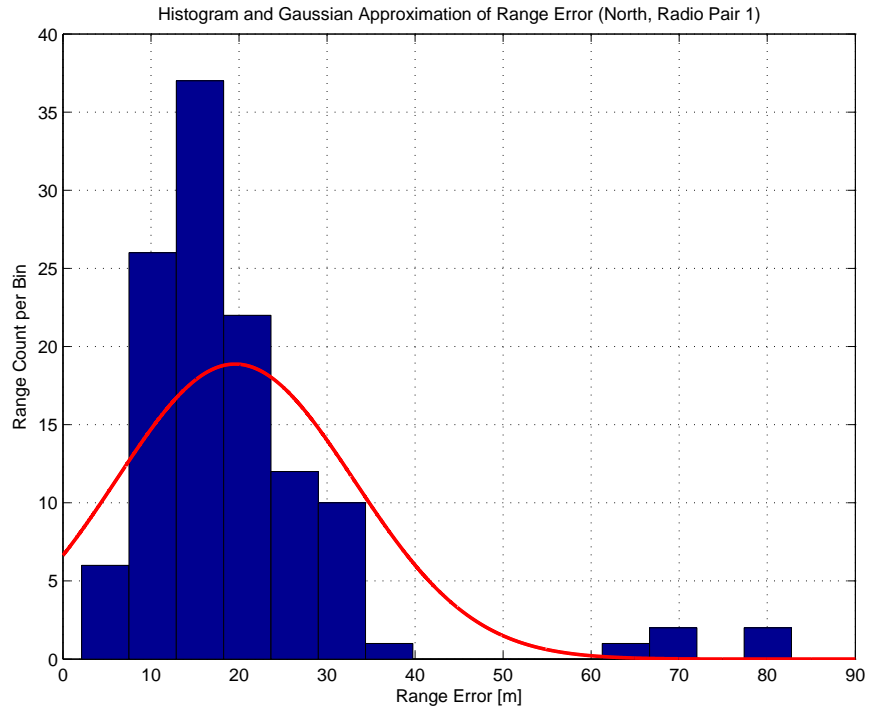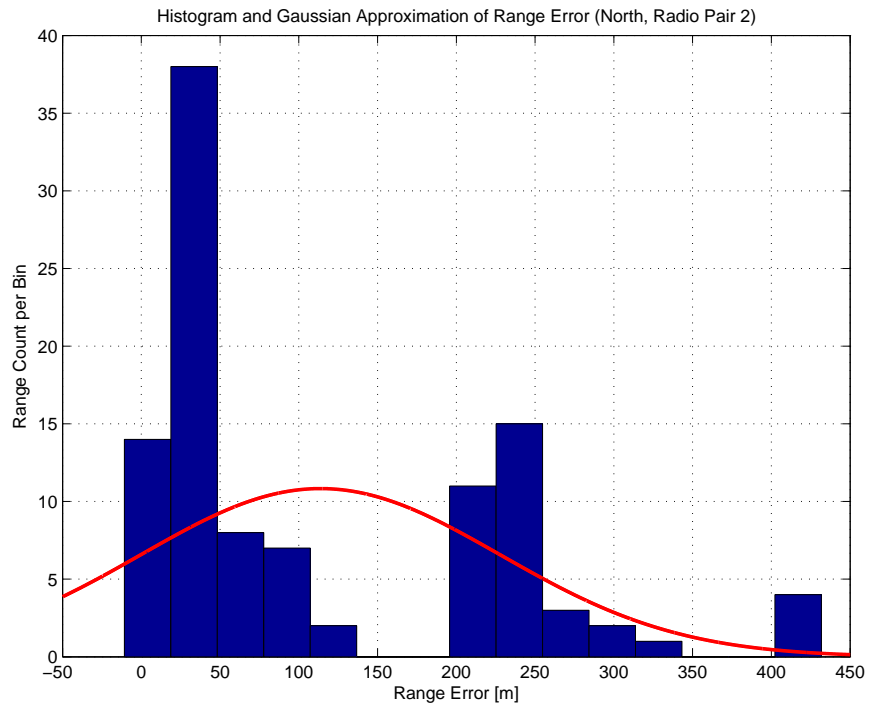Table 4.3:   Statistics for North, Radio Pair 1 Range Error. The range distribution has a positive mean, due to RF interference, and does not conform to the Gaussian distribution.

Parameter	Value
Mean	19.56 m
Std Dev	13.52 m
RMS Error	23.77 m
Chi Squared Test	Non-Gaussian

Table 4.4:   Statistics for North, Radio Pair 2 Range Error. The range distribution has a large positive mean, due to RF interference, and does not conform to the Gaussian distribution.

Parameter	Value
Mean	113.78 m
Std Dev	114.10 m
RMS Error	161.13 m
Chi Squared Test	Non-Gaussian

of both graphs, the spread of the ranges do not exceed 120 meters as was present in Figure 4.7. This indicates less RF interference. The bias of the error is again different for both of the *south* radio pairs. The bias of 20.5 meters and RMS error of 24.4 meters for the *south* radio pair 2 is similar to the *north* radio pair 1 which suggests similar RF interference exists between these radio pairs at their respective locations. A difference from the *north* radio pair 1 is the outcome of the Chi-Square GOF test. The Chi Squared test for *south* radio pair 2 reports the distribution is Gaussian. This indicates that, under certain circumstances, the distribution of range error may be considered a normal distribution. However, the lack of conformity to the normal distribution for a majority of the range error histograms suggests the bulk of range errors do not fit a Gaussian distribution.

Much greater range error is present in the indoor stationary range measurements as compared with the outdoor stationary range measurements. The RF channel obstructions which induce RF interference and signal attenuation, cause a significant
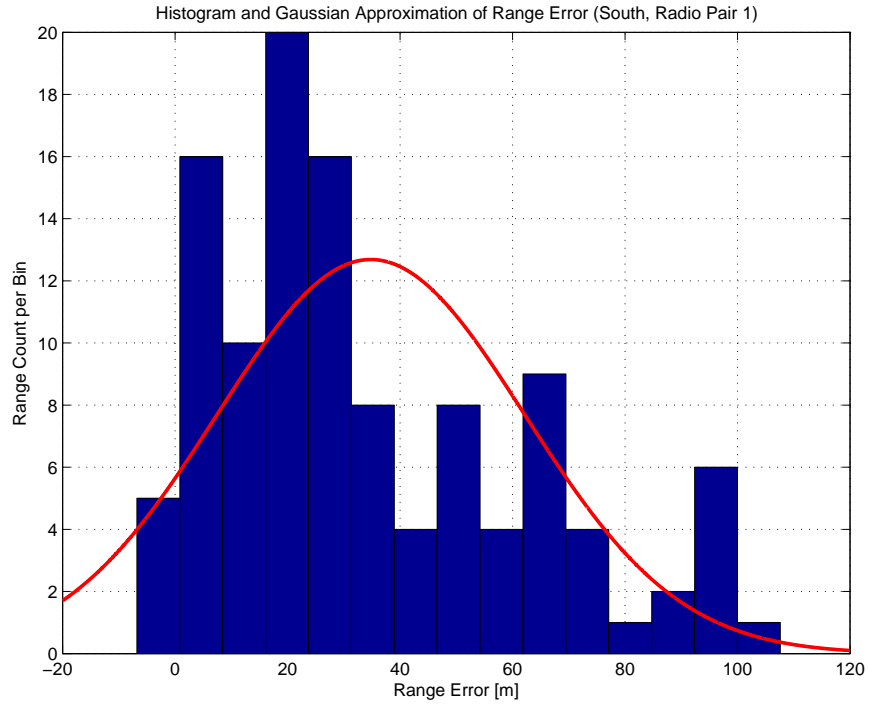
74

Figure 4.8:   Indoor South Range Error Between Radio Pair 1. Note the positive tail on distribution due to RF interference.
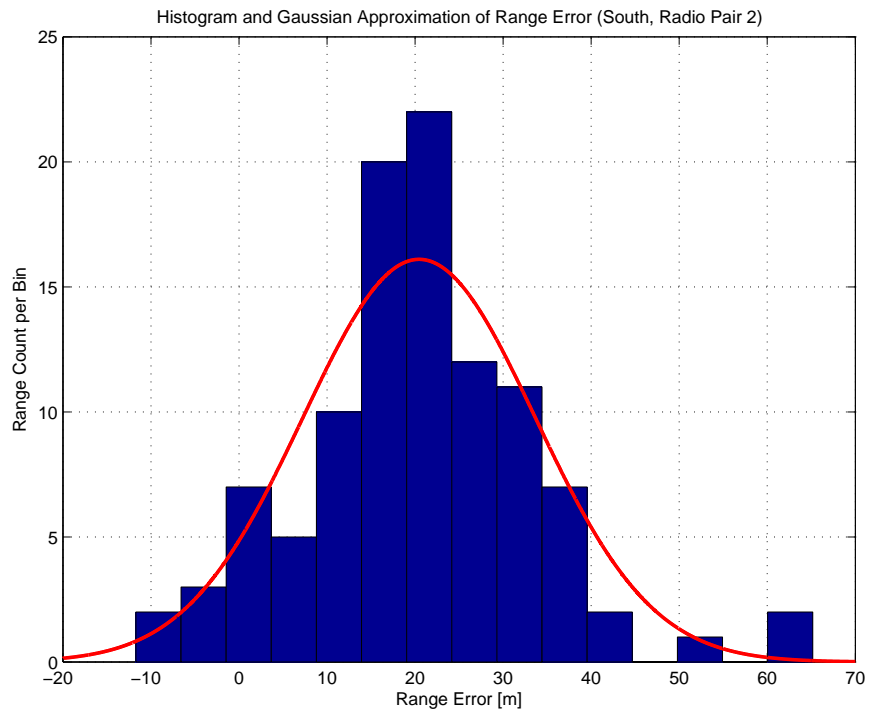

Figure 4.9:   Indoor South Range Error Between Radio Pair 2. Note the close fit of the histogram to the normal distribution overlay.

Table 4.5:   Statistics for South, Radio Pair 1 Range Error. The range distribution has a positive mean, due to RF interference, and does not conform to the Gaussian distribution.

Parameter	Value
Mean	34.80 m
Std Dev	27.34 m
RMS Error	44.26 m
Chi Squared Test	Non-Gaussian

Table 4.6:   Statistics for South, Radio Pair 2 Range Error. The range distribution has a positive mean, due to RF interference, and does not conform to the Gaussian distribution.

Parameter	Value
Mean	20.46 m
Std Dev	13.21 m
RMS Error	24.35 m
Chi Squared Test	Gaussian

increase in range error for the indoor usage of the DH500 radio system. The model of true slant range plus white, Gaussian noise used in the EKF radio range model must be adjusted to properly account for the error in the measured range for both the indoor and outdoor applications.

Possible modifications to the EKF range update algorithm include increasing the noise or uncertainty of the range measurement model. An increase in the range model uncertainty will reduce the effectiveness of all range measurements available to the filter without regard for range measurements with low error. From the histograms presented in the outdoor and indoor range error characterization, some range measurements have relatively low error compared with the rest. It would be preferable to simply remove the erroneous range measurements and reduce the EKF range model uncertainty.

Residual monitoring, presented in Section 2.9.1, allows the rejection of a particular range measurement based on its residual. When the residual exceeds the threshold

the measurement is rejected. A typical threshold is 3-σ, where σ is the standard deviation of the residual uncertainty. This algorithm ceases to work constructively when the internal navigation solution of the navigation system drifts so far that every radio residual measurement error is greater than the threshold, resulting in the rejection of the all range measurements.

A better approach is to vary the range model uncertainty based on the error present in each range measurement. The Sage-Husa adaptive algorithm provides this solution. Range measurements with lower error more strongly correct the EKF position states, while ranges with large error do not significantly corrupt the position estimate. Another benefit is observed when the navigation solution contains large position error. Instead of rejecting all range measurements as with residual monitoring, the Sage-Husa adaptive algorithm includes all the available range measurements to help correct and reduce the navigation system position error. The next two sections present analysis of the moving data set. The RMS range errors presented for the stationary data sets are used to initialize the EKF range model uncertainties in the next sections.

4.2   Outdoor Moving Analysis

The results from the moving outdoor data collections are presented in this section. Setup for the outdoor moving data collections is presented in Section 3.2.2. Four outdoor moving data collections are performed. The four data collections are labeled "moving_1a," "moving_1b," "moving_2a," and "moving_2b." The duration of each collect is laid out in Table 4.7.

Table 4.7:   Total Stationary and Moving time of the Outdoor Moving Data Sets

Data Collection	Total Time
moving_1a	595 s
moving_1b	559 s
moving_2a	551 s
moving_2b	559 s

Post-processing of the four data sets is conducted using a bottom-up tuning approach. First, the four data collections are post-processed using only INS data with all filter bias-estimation disabled. This helps emphasize the impact of the filter bias estimation algorithm which is enabled next. Then, radio range data along with the simulated baro-altitude data is added. Tuning of the EKF radio range model uncertainty is performed at this step. Finally, the results from EKF radio range model with residual monitoring and then the Sage-Husa adaptive algorithm are presented to evaluate the impact of these algorithms on further constraining the INS drift.

Of the four outdoor moving data sets, "moving_1b" and "moving_2b" are chosen to provide the reader detailed examples for each step of the bottom-up tuning approach. Horizontal trajectory comparison for remaining data sets are analyzed together at the end of each subsection to show the variety of results obtained.

During the collection of each of the four data sets, the "true trajectory" of the navigation system is also recorded. This true trajectory consists of the INS-aided DGPS position, velocity, and attitude estimate from the SPAN.

4.2.1 INS Data Only, No Filter Bias Estimation. The first iteration of post-processing uses only INS data. No filter alignment is performed because the filter bias states are disabled for this first iteration. EKF post-processing alignment is separate from the SPAN HG1700 INS alignment procedures conducted as stated in Section 3.1.1. The EKF's bias estimation is also disabled for this first iteration to display the drift present in pure inertial navigation. This strongly motivates the need for drift constraint capability within the navigation system. The following figures present the position and attitude error accumulated by the navigation system.

Figure 4.10 presents the position error graph. The 1-σ filter uncertainty bounds show the EKF's uncertainty for each state. The filter has a very high level of uncertainty in the position states after 500+ seconds of operation. This is typical for a tactical-grade INS system, but provides unusable long-term navigation capability. Next, the attitude errors are evaluated.
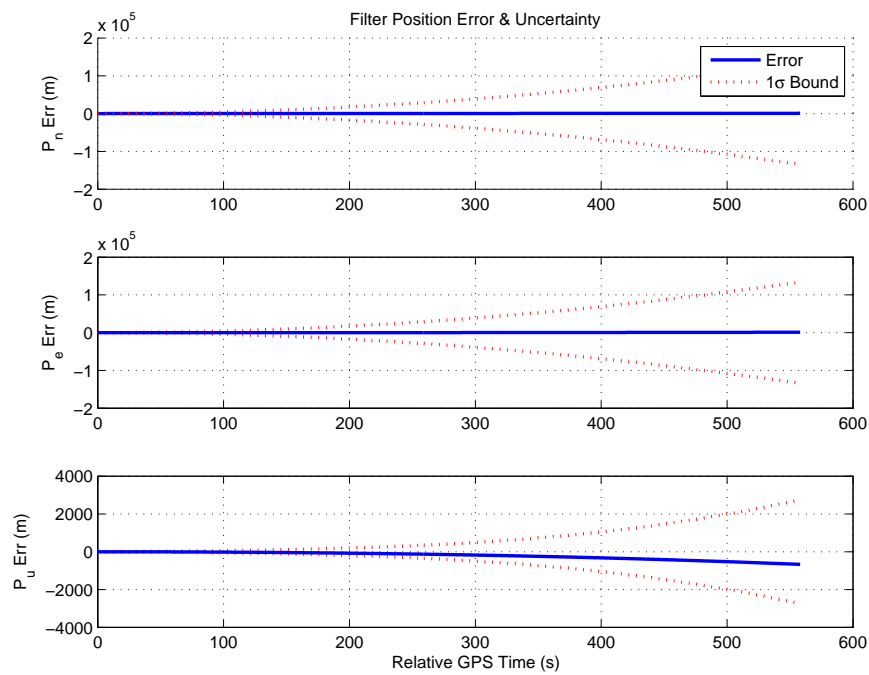
Figure 4.10: Position Error for Data Collect "moving_1b." Only INS data is used in the filter and the bias estimation capability is disabled. Observe the very high filter position uncertainty which exceeds 10,0000 meters. This is typical for a tactical-grade INS, but does not provide usable long-term navigation capability.
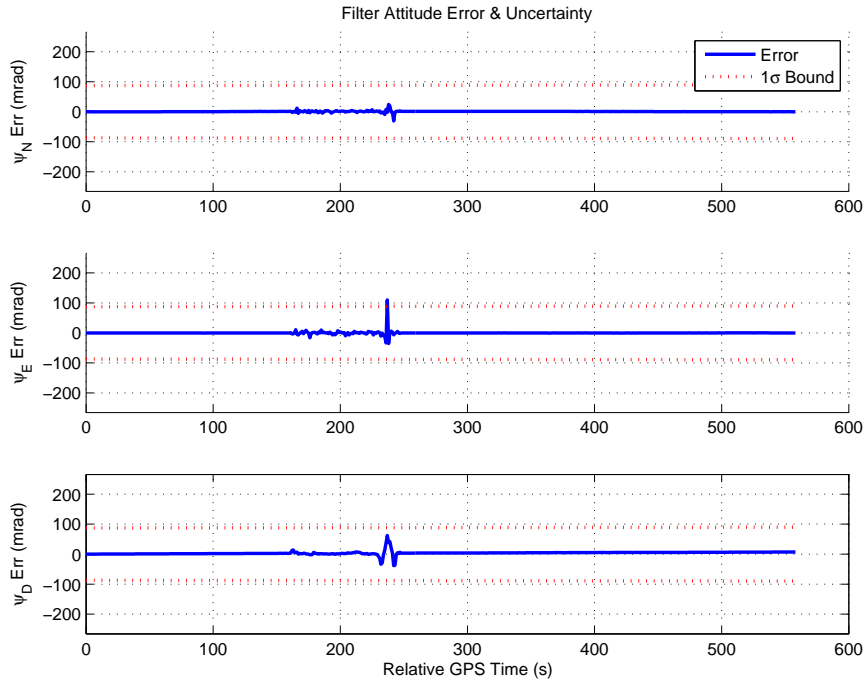
Figure 4.11: Attitude Error for Data Collect "moving_1b." Only INS data is used in the filter and the bias estimation capability is disabled. Note the large attitude uncertainty of 87 mili-radians ($\pm 5.0°$).

Figure 4.11 presents the attitude error graph. As with the position error graph, the filter attitude errors fall well within the 1-σ filter uncertainty bounds. The filter also has a large level of uncertainty for each of the attitude states. The uncertainty of 87 mili-radians correlates to $\pm 5.0°$ of attitude error. This is characteristic of a tactical-rade INS, but presents unusable navigation capability for the purposes of this thesis. The brief increase in attitude error observed between approximately 150 and 250 seconds is an anomaly potentially due to a grounding issue within the navigation system. The time constraints of this thesis prevented the source of this anomaly from being found. This anomaly is found throughout the outdoor moving data collections presented. The effect of position uncertainty on the horizontal trajectory of the navigation system is presented in the next set of graphs.

Figure 4.12 presents the EKF post-processed results for the four outside data runs. Each post-processed trajectory is compared against the true trajectory as provided by the SPAN INS-aided DGPS position solution. Note how the horizontal

(a) Moving 1a   (b) Moving 1b

(c) Moving 2a   (d) Moving 2b
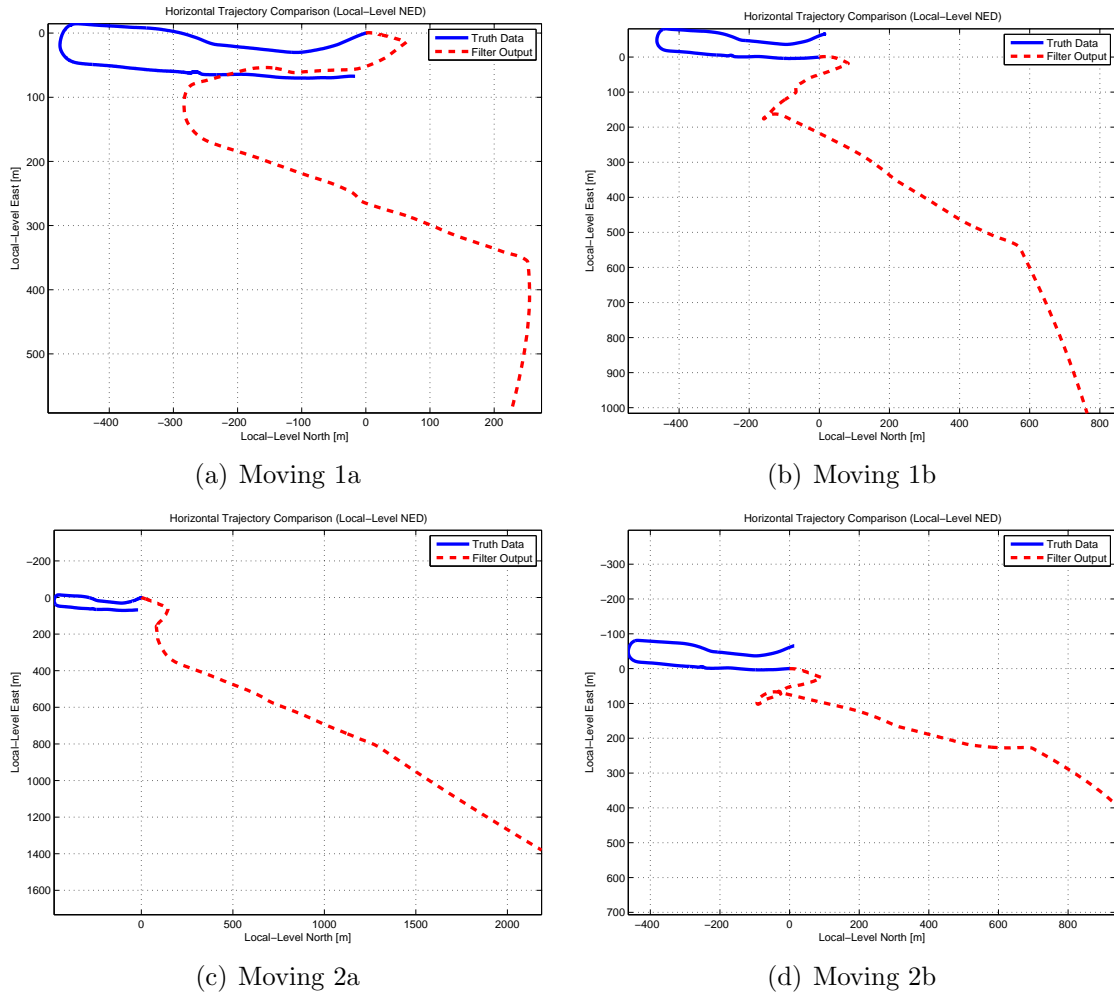
Figure 4.12:   INS Data only Horizontal Trajectory Comparison for the four Outdoor Moving Data Collections. Note the variety in the amount of drift for each data set.

position errors range upwards of 2000 meters for Figure 12(c). The difference between each of the four plots in Figure 4.12 is primarily due to noise as described in Section 2.4.3.

The significant trajectory drift observed in Figure 4.12 strongly motivates the need for navigation sensor with constrained, long-term drift. Before such a sensor is added, EKF bias estimation is enabled to extract the best possible navigation using only INS data.

Figure 4.13: Position Error for Data Collection "moving_1b." The EKF uses only INS data, but with bias estimation enabled. Note the factor of 100 reduction in filter uncertainty for the position stated as compared with Figure 4.10 where bias estimation is disabled.

4.2.2 Enable Filter Bias Estimation. To allow the EKF to properly estimate the bias states for the accelerometers and gyroscopes, a 2-minute station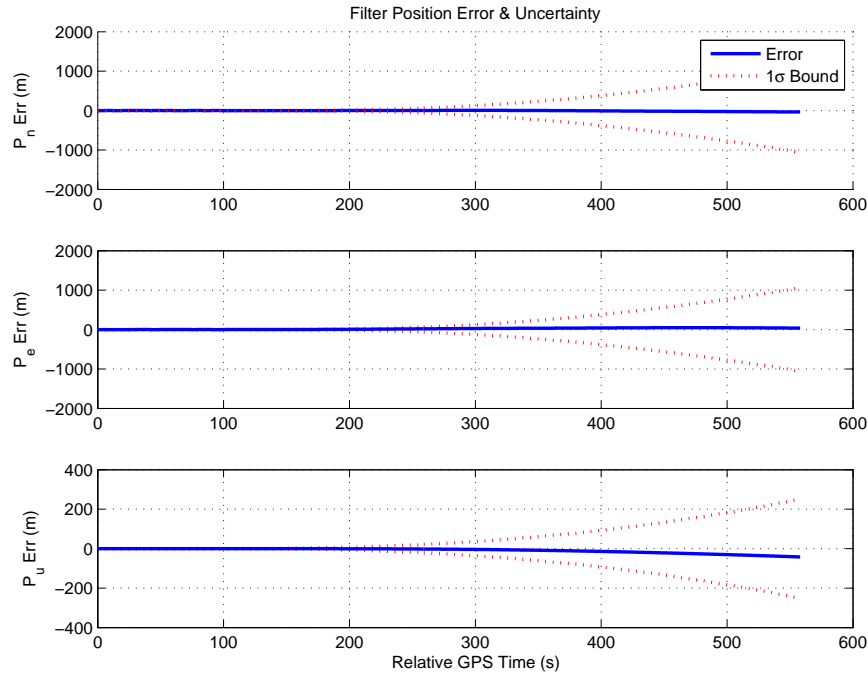ary alignment is performed. This alignment is performed by providing measurement updates to the EKF of position, velocity, and attitude using the INS-aided DGPS truth navigation solution. After the 2-minute alignment, the truth data updates are removed and the EKF continues to estimate the navigation states. Only INS data is used for the following analysis.

Figure 4.13 presents the position error graph. The 1-σ bounds reflect several orders of magnitude reduction in the filter uncertainty afforded by estimation of the INS biases. Note also that the vertical P_u position channel error is also reduced by a factor of 10.

Figure 4.14 presents the attitude error graph. Note how strongly the attitude error is constrained. The filter attitude uncertainty is reduced by a magnitude of 100
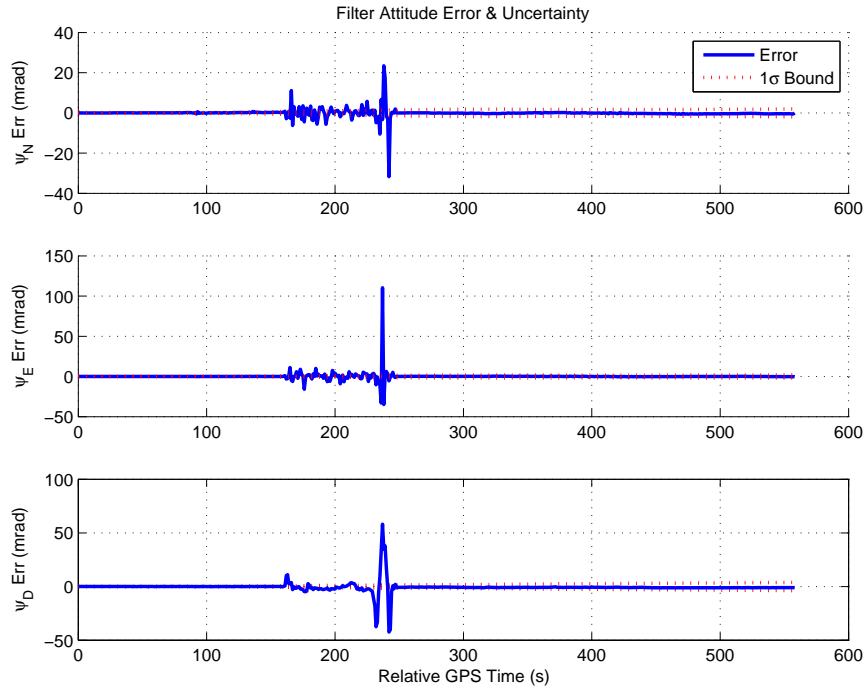
Figure 4.14: Attitude Error for Data Collect "moving_1b." The EKF uses only INS data, but with bias estimation enabled. Note the factor of 100 decrease in filter uncertainty for the attitude states when compared with no bias estimation as presented in Figure 4.11.

as compared with Figure 4.11 in the previous section. The attitude anomaly is much more apparent due to the reduction in scale of the vertical axes. Besides the anomaly, the filter's attitude error remains within the filter's 1-σ uncertainty bounds. The next two graphs present the filter's estimate of the gyro and accelerometer biases.

Figure 4.15 presents the accelerometer bias estimated by the EKF. The 2-minute alignment allows the filter to estimate the accelerometer biases with low uncertainty. From Figure 4.15, the biases estimated are quite small, but the horizontal trajectory comparison graphs presented at the end of this section displays the significant drift reduction afforded by removal of these small biases. The filter uncertainty of the accelerometer biases reached a minimum around the 120 second point where the alignment updates are removed from the filter. The filter's estimation of the biases drifts slightly over the remaining trajectory time. The filter's uncertainty for each accelerometer axis also grows over time. This growth is expected. After the alignment
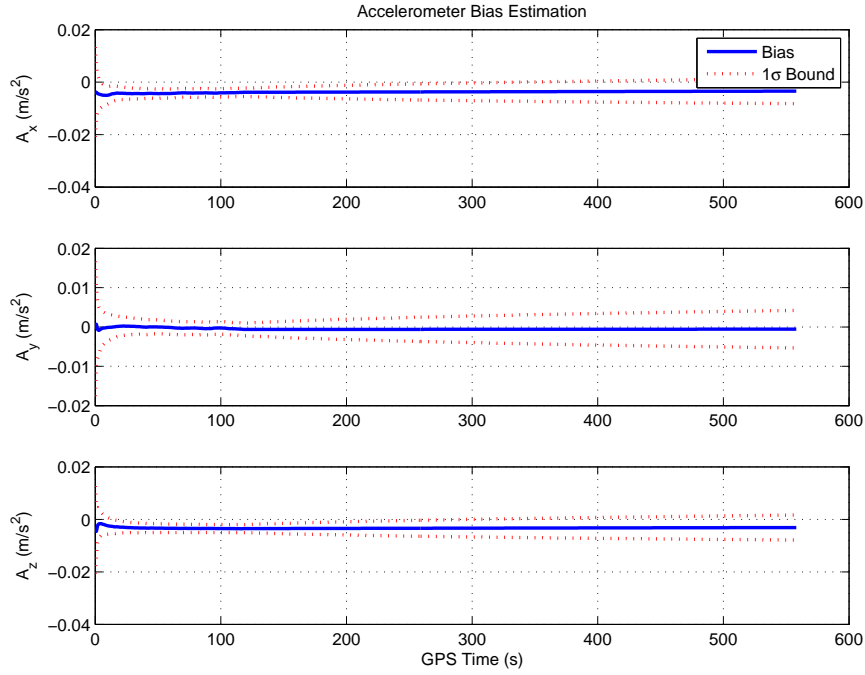
83

Figure 4.15: Accelerometer Bias Estimation for Data Collection "moving_1b." The filter is given only INS data with bias estimation enabled. The low uncertainty of the bias estimate is due to the length of the filter alignment.

updates are removed, the filter is not able to accurately observe the accelerometer biases which results in the increasing uncertainty of the filter's accelerometer bias estimates.

Similarly for the gyroscope bias estimation, as presented in Figure 4.16, the EKF is able to accurately estimate the gyro biases within the 2-minute initial alignment. As observed from Figure 4.16, the gyro biases vary until the 2 minute mark when alignment updates are removed. From this point the filter does not significantly change the gyro bias estimates. A potential pitfall of the gyro bias estimation is the continual decrease of filter uncertainty as is observed for the B_z gyro bias channel. As the filter's uncertainty decreases, the weight placed on the incoming sensor data decreases resulting in potential filter divergence for the particular state. Careful filter tuning helps to alleviate the divergence issue. The next set of plots display the overall strength of EKF bias estimation in reducing trajectory drift.
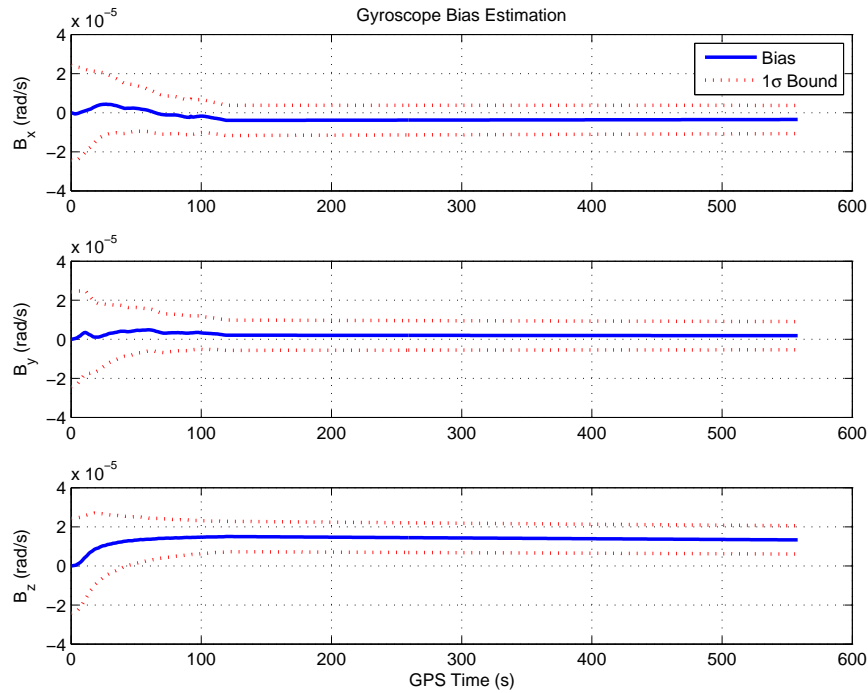
Figure 4.16: Gyroscope Bias Estimation for Data Collection "moving_1b." The filter is given only INS data with bias estimation is enabled. The low uncertainty of the bias estimate is due to the length of the filter alignment.

The effect of EKF bias estimation on each of the four outdoor moving data collections is observed in Figure 4.17. In general, estimation of the accelerometer and gyro biases greatly improves the INS navigation solution. The continued poor results from data collection "moving_2b" are due to attitude anomalies, similar to Figure 4.14, which occur for the duration of the moving portion of the trajectory. The orientation of the INS accelerometers is derived from the gyroscope attitude estimate. Errors in the attitude estimate due to the anomalies cause significant errors in the position estimate.

The navigation system's trajectory drift has been significantly reduced by EKF bias estimation. The next section adds radio range measurements and vertical channel constraint to the EKF post-processing.

4.2.3   Add Vertical Channel Constraint and Range Measurements.   The filter bias estimation added in the previous section resulted in a significant reduction in the

85
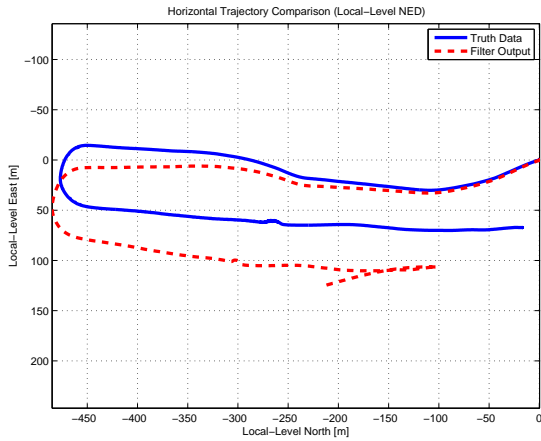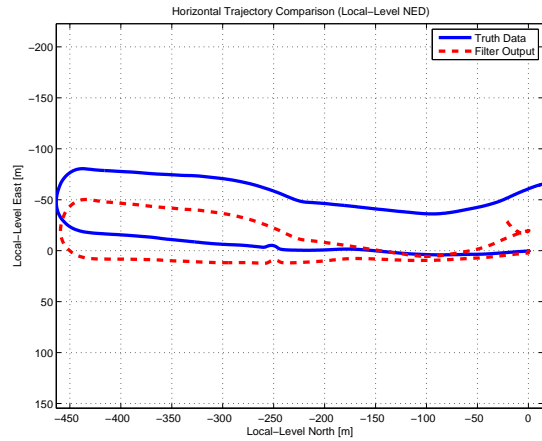
(a) Moving 1a

(b) Moving 1b
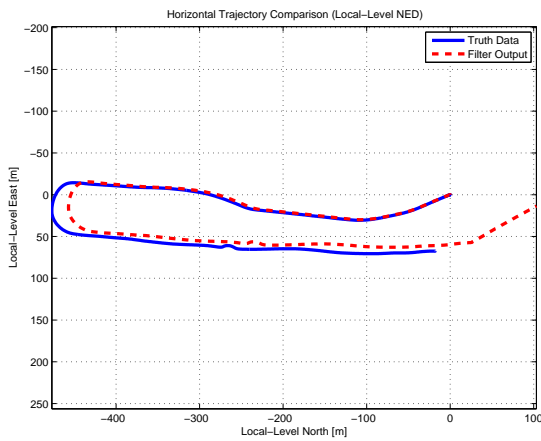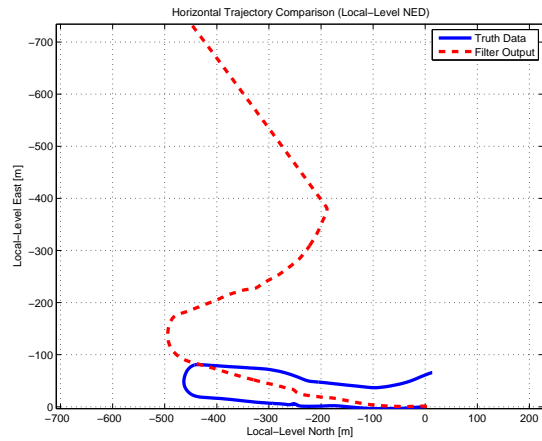
(c) Moving 2a

(d) Moving 2b

Figure 4.17:   INS Data with Bias Estimation Horizontal Trajectory Comparison. Significant reduction in trajectory drift is observed with EKF bias estimation enabled. The significant drift in data collect "moving_2b" results from large attitude anomalies which add to the accumulation of INS attitude error.
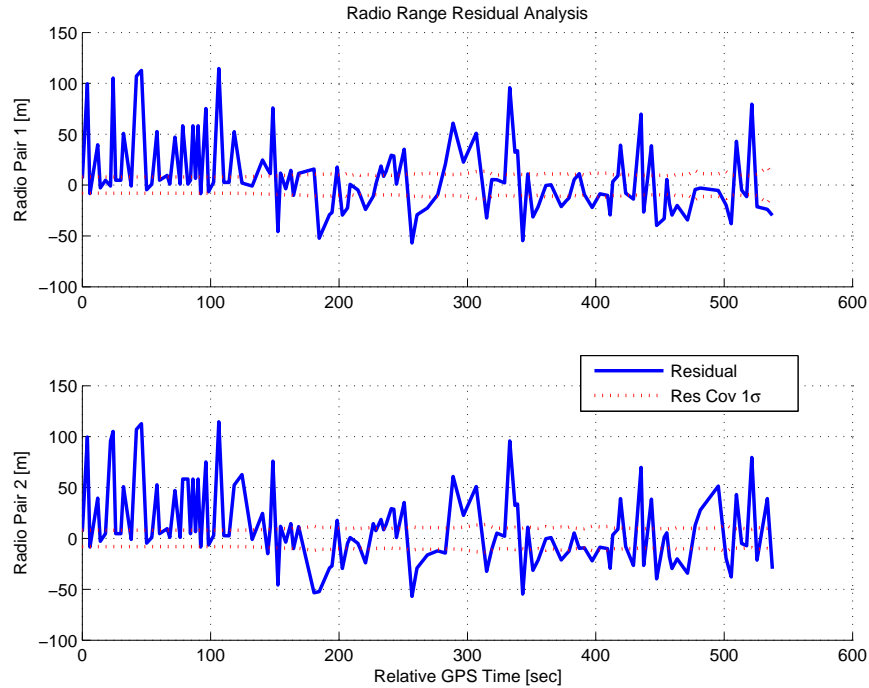
Figure 4.18: Range Residual Analysis for Data Collect "moving_1b." This graphs shows the initial choice of 8 meters for the EKF radio range model uncertainty is too low. The actual uncertainty of the range measurements is higher.

trajectory drift. This section evaluates the addition of vertical channel constraint data and radio range data to the EKF. The post-processing now consists of INS data, vertical constraint data, radio range measurements, and EKF bias estimation. As mentioned in Chapter III, the vertical channel constraint data consists of corrupted vertical channel data from the INS-aided DGPS truth data.

Based on the outdoor stationary data collection presented in Section 4.1.1, an initial EKF radio range model uncertainty of 8 meters is chosen. Figure 4.18 shows the range residual analysis for this model uncertainty value. The range residuals are much larger than the 1-σ standard deviation bounds as indicated by the residual covariance. After analysis of the range residuals for each of the four outdoor moving data collections, the model uncertainty is redefined as 55 meters.

Residual analysis with the update model uncertainty is shown in Figure 4.19. The radio range model uncertainty is now correctly tuned for the outdoor environ-

ment. It will be shown later that this uncertainty must be re-tuned for the indoor environment. The filter now has an accurate range model as observed by 70-80% of range residuals now falling within the 1-σ residual covariance bounds.

The effect of the range measurements and vertical channel constraint data as viewed from the error in the filter position states is shown in Figure 4.20. Note the 2-minute filter alignment procedure which greately constrains the position states. Observe the constrained vertical channel P_u which results from incorporating slighly corrupted INS-aided DGPS vertical channel measurements into the EKF. Also observe the constraint on the horizontal navigation channels P_n and P_e. This displays the effect of the EKF radio range model on the filter uncertainty and the effect of the range measurements on the filter position error. Both the uncertainty and position error are constrained as defined by the radio range model. The position estimation errors committed by the EKF match the filter's uncertainty. This indicates the filter is tuned correctly.

Note the higher overall uncertainty shown for the P_e east-axis in Figure 4.20. The increased uncertainty is due to the geometry of the radio positions. Given the radio positions described in Section 3.2.2, the radio system provides much stronger observation of the north-axis movement of the sensor platform then the east-axis movement. This is reflected in the increased Kalman filter state uncertainty for the P_e east-axis. The next set of plots show the drift constraint capability of the radio range measurements.

Figure 4.21 displays the effect of adding the radio range measurements and vertical channel constraint data to the EKF post-processing. Overall, the radio range data provides significant trajectory drift constraint. The most notable example is in Figure 4.21 (d) which has large trajectory drift due to significant attitude error anomalies. The radio range data helps constrain the trajectory to within 20-50 meters of the trajectory truth data.
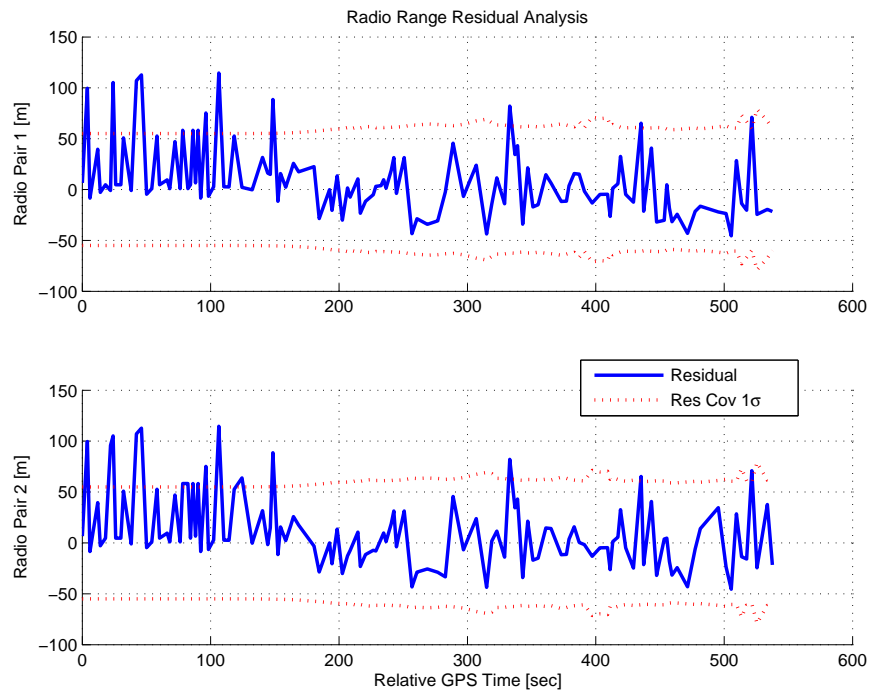
Figure 4.19: Range Residual Analysis for Data Collect "moving_1b." Re-tuned
EKF radio range model with uncertainty defined as 55 meters. The updated model
uncertainty now fits the actual range measurement data as is shown by 70-80% of the
range residuals falling within the 1-σ residual covariance bounds.
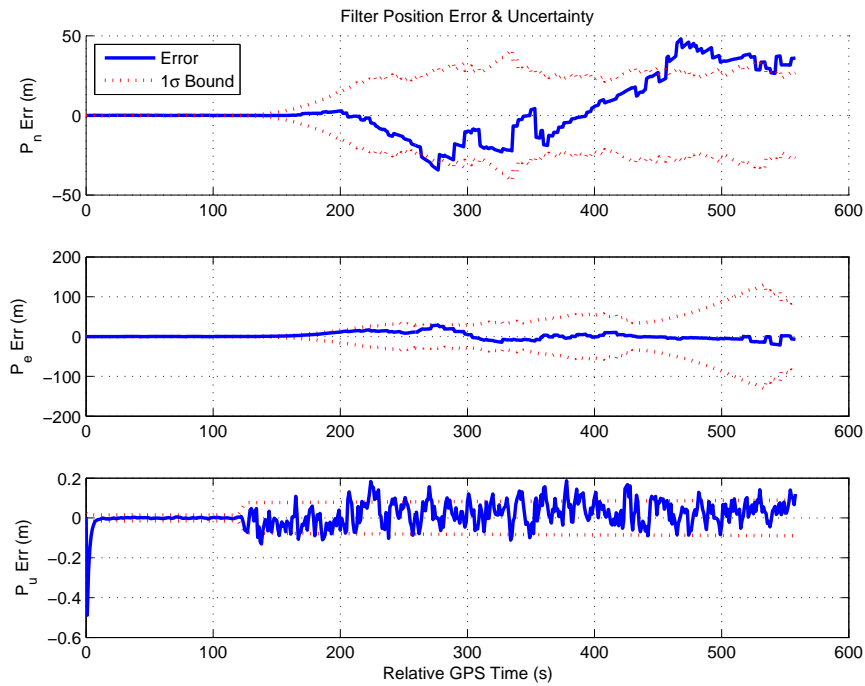
Figure 4.20: Position Error for Data Collect "moving_1b." The EKF utilizes bias estimation with INS, radio range, and vertical channel constraint data. The radio model uncertainty has been re-tuned to 55 meters. Note the constrained uncertainty for the filter position states. Also, note the filter position errors do not significantly exceed the 1-σ filter uncertainty bounds, indicating a correctly tuned filter.
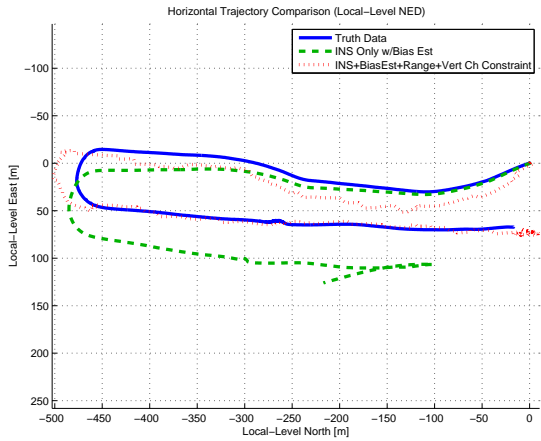
(a) Moving 1a
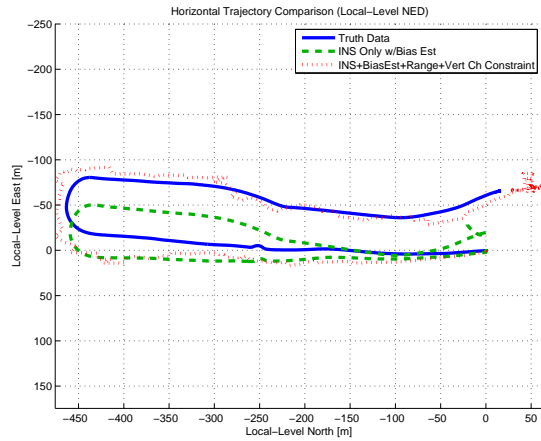
(b) Moving 1b
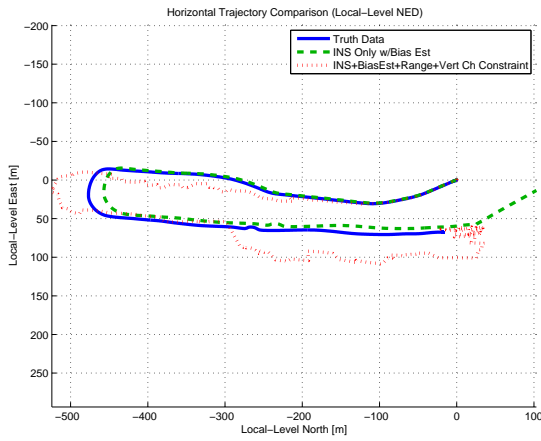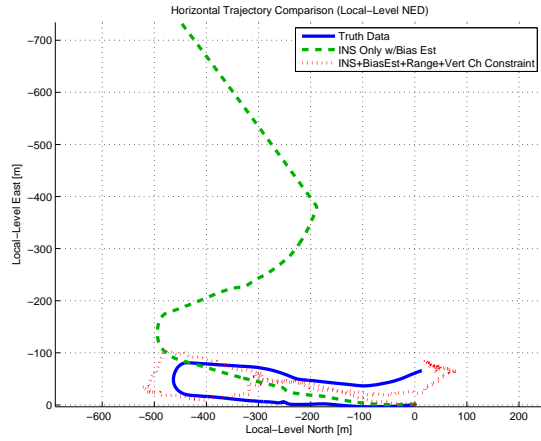
(c) Moving 2a

(d) Moving 2b

Figure 4.21:   Horizontal Trajectory Comparison. Range measurements and vertical channel constraint data are added to the INS data with EKF bias estimation enabled. Overall, the additional data provides notable trajectory drift constraint.

Better trajectory drift constraint performance is observed for Figures 4.21 (a) and 4.21 (b). This is largely due to the fewer attitude error anomalies. The trajectory error is constrained well within 15-50 meter bounds.

The radio range measurements actually corrupt the INS+Bias trajectory as shown in Figure 4.21 (c). The INS-only with filter bias estimation trajectory has very low drift. The INS+Bias trajectory drifts most significantly at the end of the trajectory where the INS-only trajectory drifts to about 100 meters north of the true end of the trajectory. The very low INS-only drift is due to good initial filter alignment. The notable error added from the range measurements is due to the tuning of the INS model and range model uncertainties. The filter position uncertainty increases over time with only INS data as shown previously in Figure 4.10 and 4.13. Bias estimation helps to reduce the magnitude of the growth in filter position uncertainty, but bias estimation does not constrain the long-term increase of this uncertainty. The large filter uncertainty allows the range measurements to corrupt the horizontal position states.

Observing the four horizontal trajectory comparison plots, the very low drift observed in Figure 4.21 (c) is not particularly common. The Figures 4.21 (a) and 4.21 (b) show INS-only drift consistent with a tactical-grade INS. The significant INS+Bias drift shown in Figure 4.21 (d) is due largely to poor initial filter alignment. A potential source of the poor initial alignment comes from slight movement of navigation system during the alignment procedure.

Now that the outdoor drift-constraint capability of the DH500 radio system has been demonstrated, two algorithms are applied to the EKF range measurement update algorithm to further constrain the trajectory drift. The next section presents results obtained from residual monitoring and the Sage-Husa adaptive algorithm.

4.2.4   Residual Monitoring and Sage-Husa.   The analysis of residual monitoring and the Sage-Husa adaptive algorithm are presented in this section. The inclusion of range measurements and vertical channel constraint data in the previous

section showed improvement for a majority of the outdoor data runs. The trajectory corruption noted in Figure 4.21 (c) is due to the filter alignment as discussed in the previous section. To help reduce the trajectory corruption and further constrain trajectory drift, the EKF radio range model is modified to include first, residual monitoring (Section 2.9.1) and then the Sage-Huse adaptive algorithm (Section 2.9.2). These algorithms are implemented separately. The section continues with analysis of the residual monitoring technique.

4.2.4.1 Residual Monitoring. Of the four outdoor moving data collections, data set "moving_2b" is the only one which residual monitoring significantly impacts. Data set "moving_2b" contains residual covariances which exceed the 3-σ threshold. The range residuals for the other three data sets remain below the 3-σ threshold. Figure 4.22 displays the range residuals for "moving_2b" before residual monitoring is applied. Note the large residuals that occur for the second radio pair towards the beginning of the data run. These large residuals indicate that these range measurements do not conform to the EKF range model. The horizontal trajectory comparison graph shown at the end of this section displays the additional trajectory error caused by these erroneous range measurements. Residual monitoring rejects such measurements, eliminating their negative impact on the horizontal trajectory.

Once residual monitoring is applied, the erroneous range measurements are rejected. Figure 4.23 presents the range residuals for data set "moving_2b" after the residual monitoring algorithm is applied. The erroneous range measurements are now rejected and are not used to update the filter position state estimates. Note that erroneous range measurements do not occur for the first radio pair, but the residuals have changed slightly. This change is due to the variation in vehicle state estimation by the EKF due to the removal of erroneous range measurements in the second radio pair. Residual monitoring is swapped for the Sage-Husa algorithm for the next portion of analysis.
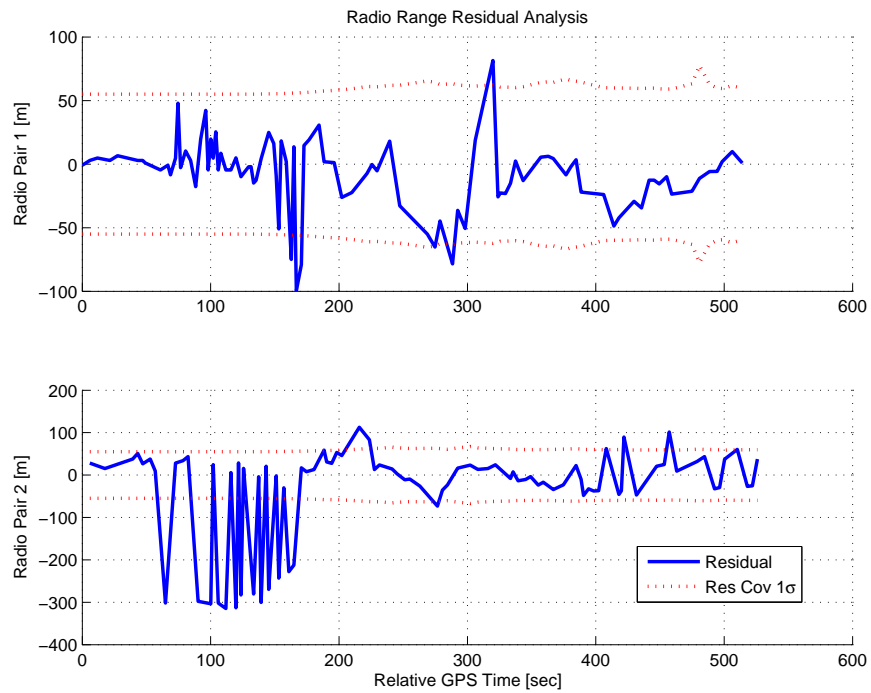
Figure 4.22: Range Residual Analysis for Data Collect "moving_2b." This graph shows the range residuals before residual monitoring is applied. Note the large negative range residuals which occur towards the beginning of the trajectory for radio pair 2.
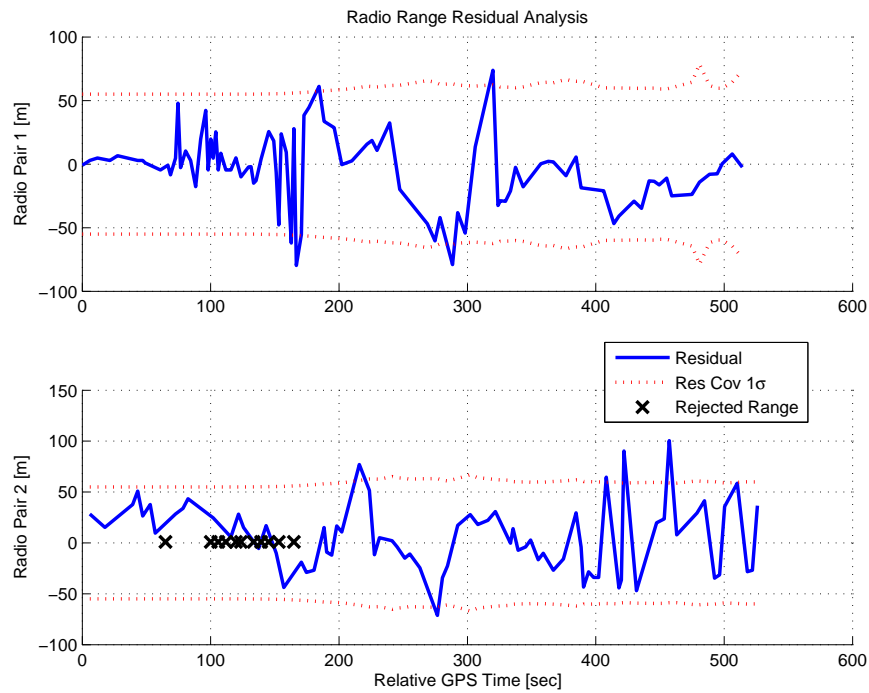
Figure 4.23: Range Residual Analysis for Data Collection "moving_2b." The graph shows the range residuals that are rejected by the residual monitoring algorithm. These residuals exceeded the 3-σ threshold and are not use to update the EKF's position states.

4.2.4.2 Sage-Husa. The Sage-Husa adaptive algorithm requires tuning of the memory factor d. As discussed in Section 2.9.2, larger memory factors place more weight on the current parameter estimate and less weight on the time-average history of the parameter. The performance of the Sage-Husa algorithm is dependent on both the memory factor d and the uncertainty of the measurements in each data set.

Figure 4.24 presents the average RMS trajectory error of each outdoor moving data set for a range of Sage-Husa memory factors. Differences in the error for each range measurement and the amount of trajectory drift present in the INS account for the variety of trajectory errors. Sage-Husa memory factors above 0.10 allowed the range model uncertainty estimate to become negative for certain data runs causing EKF instability. A memory factor of 0.005 is chosen for the four outdoor moving data sets as a compromise to obtain RMS trajectory error below that of the standard range update algorithm. While this tuning methodology provided a decrease in overall trajectory error for all four of the the outdoor moving data sets, a more robust tuning strategy would tune off of a subset of the outdoor data sets and then evaluate this memory factor on the remaining data sets. The Sage-Husa algorithm is potentially over-tuned from the tuning methodology applied.

Figure 4.25 presents the estimated value of the mean and variance for the EKF radio range model noise. The estimated mean directly correlates to the bias in the range measurements. The estimated variance directly correlates with the EKF radio range model uncertainty and is presented with 1-σ standard deviation bounds. The range residuals are also included in the plot to provide a reference for changes in the estimated mean and variance.

The mean and variance are initialized at zero and $(55\text{m})^2$ respectively. Once the EKF begins post-processing, the Sage-Husa algorithm uses the range residuals to provide an estimate of the bias and model uncertainty. For radio pair 1, the estimated EKF range model uncertainty decreases over the entire length of the run. This is due
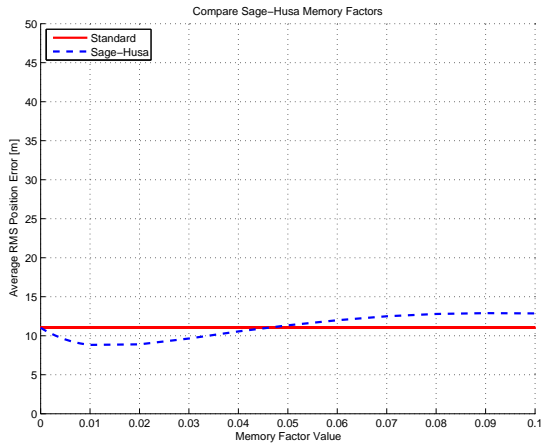
(a) Moving 1a
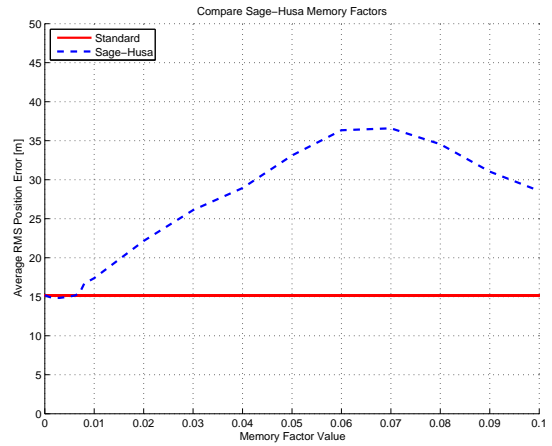
(b) Moving 1b
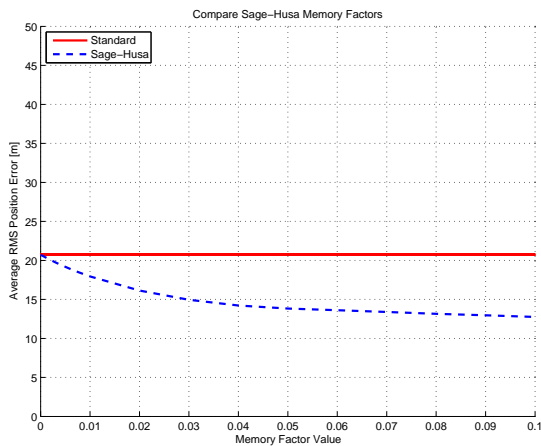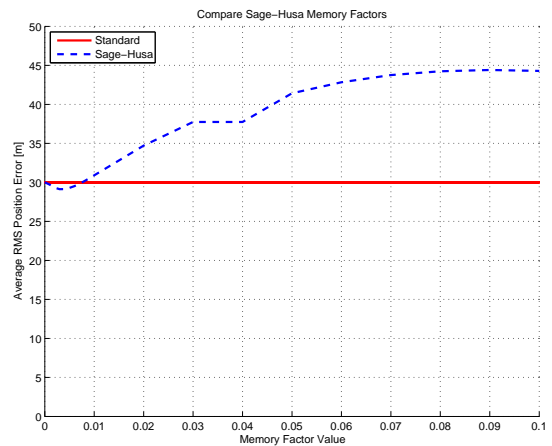
(c) Moving 2a

(d) Moving 2b

Figure 4.24: Average RMS Trajectory Error for a Range of Sage-Husa Memory Factors. Note how each data set responds differently to the same range of memory factors. Average RMS trajectory error for the standard EKF range update algorithm is shown for comparison.

97
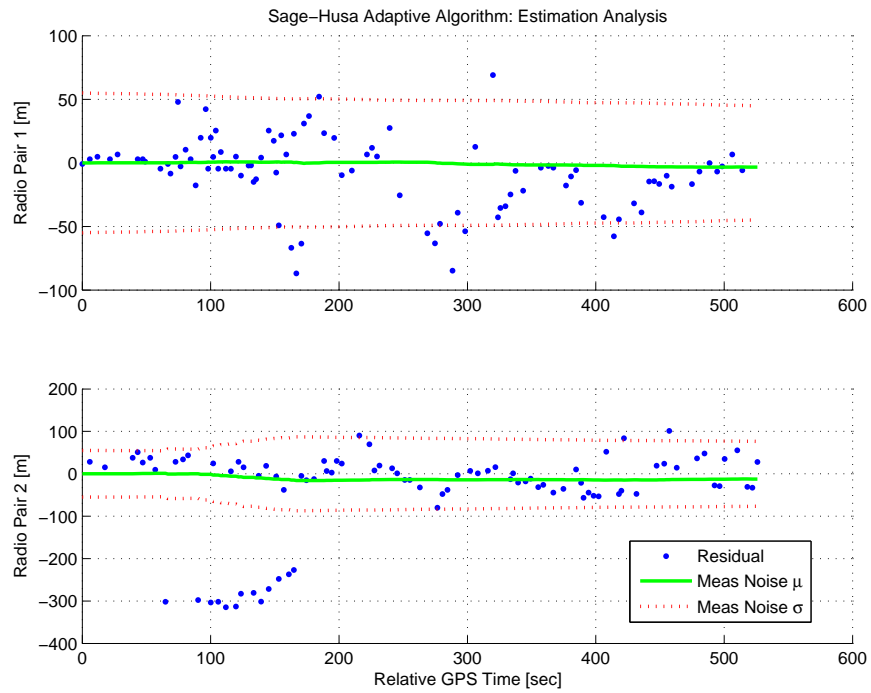
Figure 4.25: Sage-Husa Estimate Analysis for Data Collection "moving_2b." Note how the measurement noise variance, or model uncertainty, adjusts to account for changes in the residual distribution. The measurement noise mean, or range bias, slowly tracks with the average range residual value providing an estimate of the bias in the range measurements.

to the range measurements for this particular data set having an average uncertainty lower than the 55 meters defined the the EKF radio range model. The measurement bias trends slightly upward in the middle of the data set and then downward towards the end of the data set. Overall the bias remains right around zero. This is expected due to the minimal RF interference present in the outdoor environment.

For radio pair 2, the large negative range residuals at the beginning of the trajectory cause the estimated uncertainty for this radio pair to strongly increase. The increase in model uncertainty causes the EKF to place less weight on the range measurements, reducing the effect of poor range measurements on the estimated trajectory. The bias estimation becomes negative to try to account for the large negative error in the initial residuals. The remainder of the range residuals are distributed fairly evenly around the zero residual horizontal axis. The approximate zero-mean distribution of these residuals and the low memory factor of 0.005 causes the bias estimation to remaining negative for the remainder of the trajectory. The estimate of the model uncertainty for radio pair 2 decreases over the latter portion of the data run due to the range residuals clustering around the zero-residual horizontal axis.

The measurement bias and model uncertainty estimated by the Sage-Husa algorithm are used to correct the range measurements provided to the EKF. Figure 4.26 presents the post-processed trajectory results for the basic EKF radio range update algorithm, labeled "Standard", the residual monitoring algorithm, labeled "Residual Mon", and the Sage-Husa adaptive algorithm. Analysis continues with discussion of residual monitoring results.

As stated previously in this section, residual monitoring only effected the "moving_2b" data collection due to large range residuals. The range residuals for the remaining data collections do not exceed the threshold, which resulted in no change in the constraint of trajectory drift. This is observed by the complete overlap of the standard and residual monitoring plots shown in Figures 4.26 (a), 4.26 (b), and 4.26 (c). Residual monitoring did have an effect of reducing the range measurement
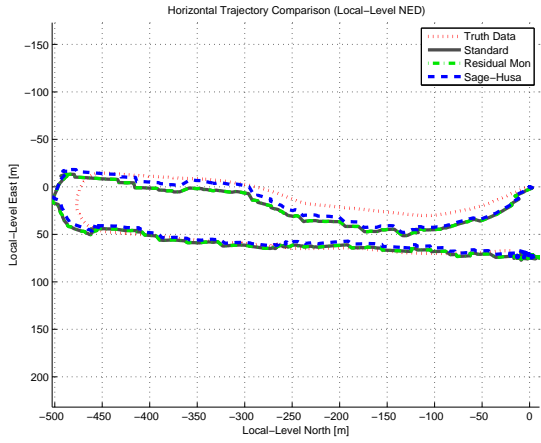
(a) Moving 1a
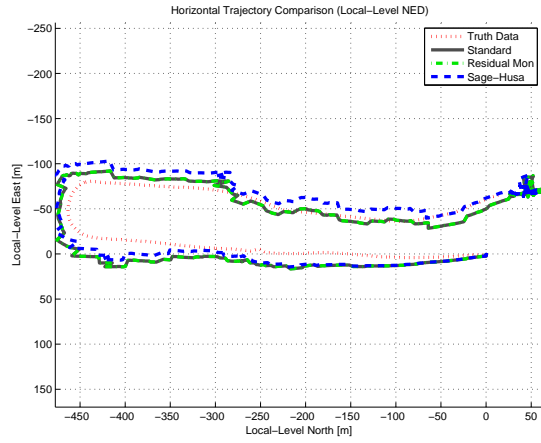
(b) Moving 1b
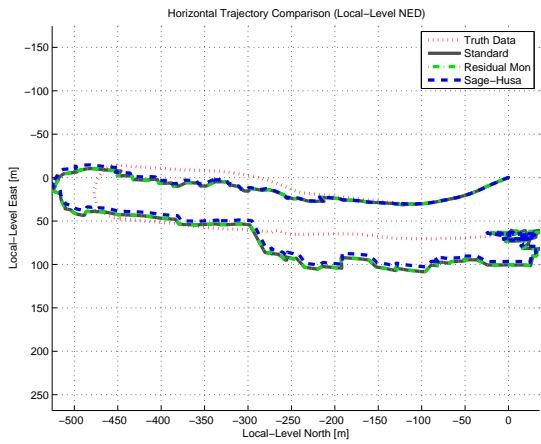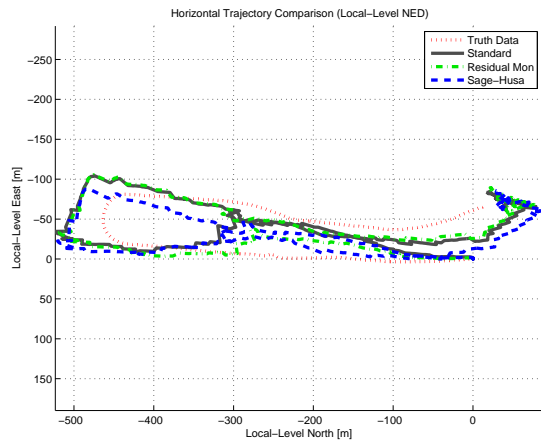
(c) Moving 2a

(d) Moving 2b

Figure 4.26:   Residual Monitoring and Sage-Husa Horizontal Trajectory Comparison. Residual monitoring only impacts data set "moving_2b" due to the large range residuals. The Sage-Husa adaptive algorithm has a variety of results dependent on the amount of INS drift and quality of range measurements.

trajectory corruption on the fourth data collection, shown in Figure 4.26 (d). This is evident by the residual monitoring plot remaining closer to the "Truth Data" than the basic EKF range update algorithm shown in the "Standard" plot. The next paragraph details the effect of the Sage-Husa algorithm.

The Sage-Husa algorithm provides a variety of results. The memory factor of 0.005 is applied to the post-processing of each of the four data collections. In Figure 4.26 (a), Sage-Husa provides a slight improvement in drift constraint during the moving portion of the trajectory. This is evident overall by the Sage-Husa plot following the truth data more closely than the standard or residual monitoring plots. The Sage-Husa algorithm appears to further corrupt the trajectories viewed in Figures 4.26 (b) and 4.26 (c). This is due to slightly incorrect estimation of the bias of the range measurements and uncertainty of the range model. The significant trajectory corruption viewed in Figure 4.26 (d) is due to the large negative range bias estimated at the beginning of the trajectory from the large negative range residuals. Figure 4.26 (d) displays a weakness of the Sage-Husa algorithm, where the negative bias estimated towards the beginning of the trajectory, as depicted in Figure 4.25, is not corrected to prevent corruption of the remaining trajectory.

The results of residual monitoring and the Sage-Husa adaptive algorithm display pros and cons for each method. Residual monitoring proves to be effective at further reducing trajectory drift and corruption by rejecting range residuals which fall outside the 3-σ threshold. However, when all residuals remain under the threshold, residual monitoring has no effect beyond the basic EKF range update algorithm. The Sage-Husa algorithm is shown to provide a variety of results. Depending on the selected memory factor and particular data set, a reduction or increase in trajectory drift is observed. A significant contribution from the Sage-Husa algorithm is run-time estimation of the range model uncertainty which allows the filter to account for variations in the uncertainty of the incoming range measurements.

This concludes analysis of the outdoor data collections. Lack of proper camera calibration due to time constraints renders the outdoor collected imagery unusable in the EKF. Proper camera calibration is obtained for the indoor data collections which allows the indoor imagery to be included in EKF post-processing. The observations and analysis presented for the outdoor data sets are used to refine and tune the navigation system for the indoor data collections. The next section presents observations and analysis for the indoor moving data collections.

4.3 Indoor Moving Analysis

This section presents results and analysis for the moving data collections performed indoors. Setup for the two groups of indoor collections is presented in Section 3.2.4. Results from residual monitoring and the Sage-Husa adaptive algorithm are presented in Section 4.3.1. Analysis of the trajectory estimate with data from the stereo imaging system are presented in Section 4.3.2.

Four data collections are performed for each of the two indoor data collect groups. The first group is labeled north-south (NS) and the second group is labeled square (SQR) due to the square-shape of the trajectory. Trajectories for the NS data sets with the "a" designation begin at the upper, or north, surveyed marker. NS trajectories with the "b" designation begin at the lower, or south, surveyed marker. The length of each indoor moving data collection is contained in Table 4.8.

Table 4.8:   Total Stationary and Moving time of the Indoor Moving Data Sets

Data Collection	Total Time
NS_1a	317 s
NS_1b	305 s
NS_2a	301 s
NS_2b	318 s
SQR_1	440 s
SQR_2	444 s
SQR_3	439 s
SQR_4	440 s

The analysis of the outdoor data sets in Section 4.2 provides a post-processing baseline for the indoor data sets. This base-line consists of INS data, filter bias estimation enabled, 2-minute filter alignment, range measurements, and vertical channel constraint data. This base EKF setup is referenced in the following plots with the label "Standard." The vertical channel constraint data is generated from the altitude of the indoor surveyed marker at each trajectory starting position.

The alignment data consists of the starting trajectory position as defined by the indoor surveyed marker, the velocity is defined as zero, and the attitude is taken from the SPAN. As presented in Section 3.1, the SPAN is primarily an INS-aided DGPS navigation system, but when GPS is not available the SPAN continues to estimate the attitude of the navigation system based off of the HG1700 INS measurements. It is important to note that the HG1700 measurements used by the SPAN to estimate the attitude are the same INS measurements used by the EKF navigation system developed in this thesis. However, the SPAN uses additional algorithms, not discussed in this thesis, to help correct and remove the INS drift. This does not constitute a "truth" data source, but provides a refined estimate of the navigation system attitude. Next, range residual analysis is summarized for the indoor data collections.

The average standard deviation of the indoor stationary data collections, presented Section 4.1.2, is 63 meters. This value is used as the initial radio range model uncertainty. Residual analysis is performed for all eight of the indoor data collections. The radio range model uncertainty is adjusted to 120 meters based on the results from all eight data sets. This value reflects the increase in range measurement error due to RF interference. The indoor results continue with residual monitoring and the Sage-Husa algorithm discussed in the next section.

4.3.1 Residual Monitoring and Sage-Husa. Residual monitoring and the Sage-Husa adaptive algorithm have a variety of effects on the outdoor moving data results in Section 4.2.4. Reduction in the trajectory drift from either algorithm was

shown to be dependent on the uncertainty of the range measurements and the drift already present in the INS data.

This section presents analysis and results from residual monitoring and the Sage-Husa algorithm for both groups of indoor data collections. Truth trajectory data is not available for the indoor moving data set due to a lack of GPS satellite visibility.

As mentioned in Section 4.2.4.2, the Sage-Husa algorithm performance is sensitive to the memory factor d and the uncertainty of the measurement in each data set. Due to the increased uncertainty for the indoor range measurements, the Sage-Husa memory factor is re-tuned for indoor use.

To tune the Sage-Husa memory factor for all of the indoor moving data sets, the resulting post-processed trajectories for a range of memory factors are overlaid on the indoor hallway map. From visual inspection, the best memory factor is chosen based on the reduction of trajectory drift and alignment of the post-processed trajectory end point with the true end point. The memory factors ranged as high as 0.4 and as low as 0.07 with the majority of values clustering around 0.1. The memory factors above 0.1 did not produce negative range model uncertainty estimates due to the large initial range model uncertainty of 120 meters. The value of 0.09 is chosen as a compromise between the eight indoor moving data runs. This value provides a reduction in trajectory error for each indoor moving data set. As mentioned in Section 4.2.4.2 for the outdoor moving data set, tuning the Sage-Husa algorithm over the entire indoor data set provided positive results for these data sets. The more robust tuning strategy would tune off of a subset of the outdoor data sets and then evaluate this memory factor on the remaining data sets. The Sage-Husa algorithm is potentially over-tuned for the indoor data sets based on the tuning methodology applied in this thesis.

The results and analysis are divided into two sections. Section 4.3.1.1 covers the NS data sets and Section 4.3.1.2 covers the SQR data sets.

4.3.1.1 NS Data Sets. Figure 4.27 presents horizontal trajectory comparison for the indoor moving NS data set. The results from the base post-processing setup, residual monitoring, and Sage-Husa adaptive algorithm are contained in Figure 4.27.

The first observation is the large drift present even with the vertical channel constraint and range measurements. A significant source of error is the initial attitude estimate provided by the SPAN. If the initial attitude estimate is incorrect, the filter will estimate incorrect biases which adds additional error to the entire trajectory.

Residual monitoring does not provide further drift constraint due to the high range model uncertainty. The range residuals do not exceed the 3-σ threshold which allows all of the range measurements to effect the trajectory.

The Sage-Husa algorithm provides a more notable reduction in trajectory drift. During the moving portions of the trajectory, the range measurement uncertainty increases due to changing RF interference conditions. As the navigation system travels along the reference paths shown in each figure, the various building walls and doors interfere with the RF signals. During the stationary portions of the trajectory, at the very beginning and end, changes in RF interference are significantly reduced. The Sage-Husa algorithm is able to reduce the range model uncertainty as it estimates the range bias error, providing stronger position updates to the EKF. This results in the constraint of the horizontal trajectory drift shown most notably in Figures 4.27 (a) and 4.27 (c).

It is also observed that less RF interference is present at the south end of the hallway (bottom of the graphs) as compared with the north end of the hallway (top of the graphs). The Sage-Husa algorithm reduces the EKF range model uncertainty where there is lower RF interference. The higher RF interference experienced at the north end of the hallway results in the larger Sage-Husa uncertainty and horizontal trajectory drift observed in Figures 4.27 (b) and 4.27 (c).

(a) North-South 1a (b) North-South 1b

(c) North-South 2a (d) North-South 2b

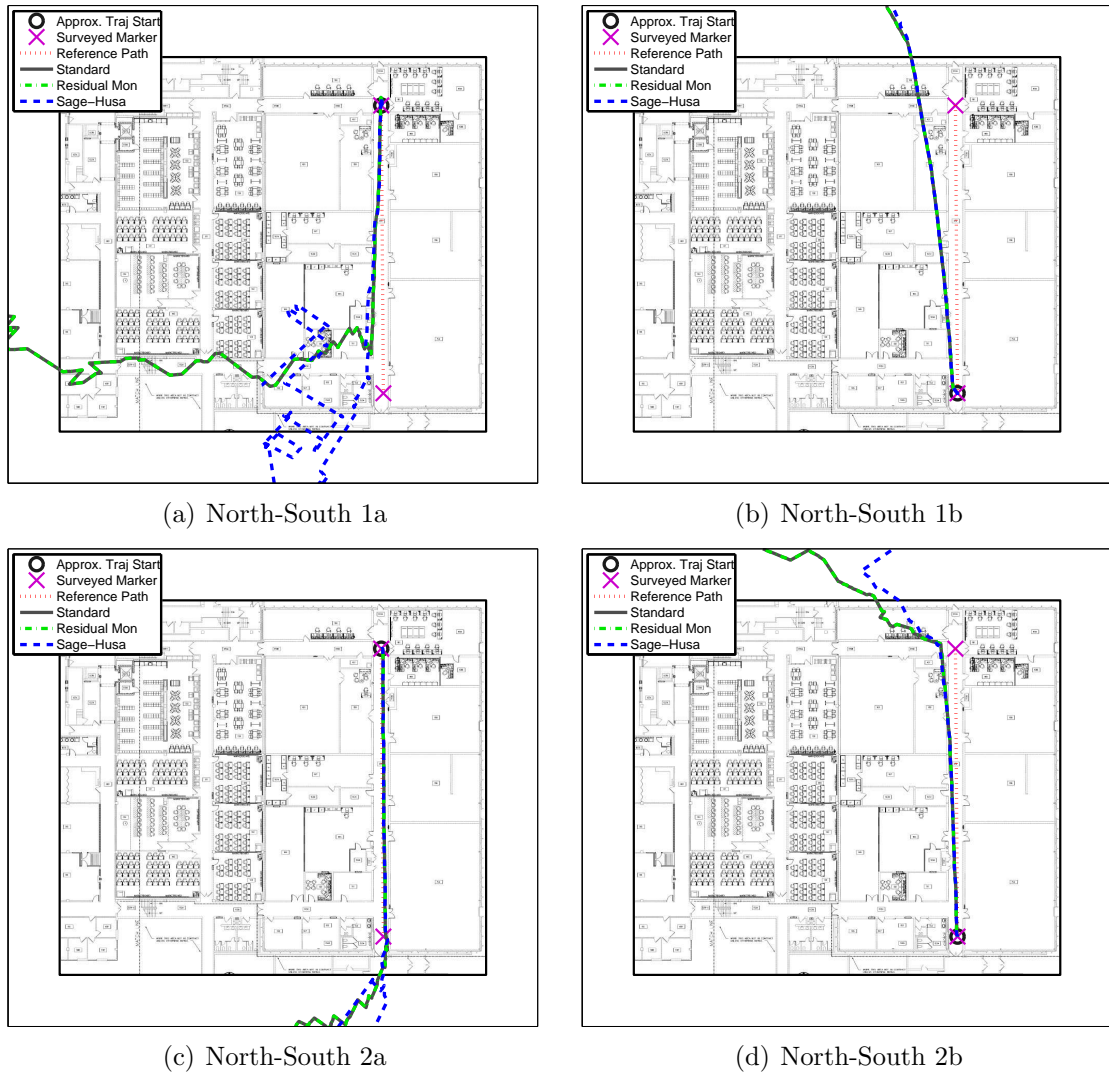Figure 4.27:   Residual Monitoring and Sage-Husa Horizontal Trajectory Comparison for North-South Indoor Data Sets. Residual monitoring does not provide additional drift constraint due to the high range model uncertainty. Sage-Husa provides a reduction in drift by reducing the range model uncertainty for range measurements with reduced RF interference as shown in Figures 4.27 (a) and 4.27 (c).
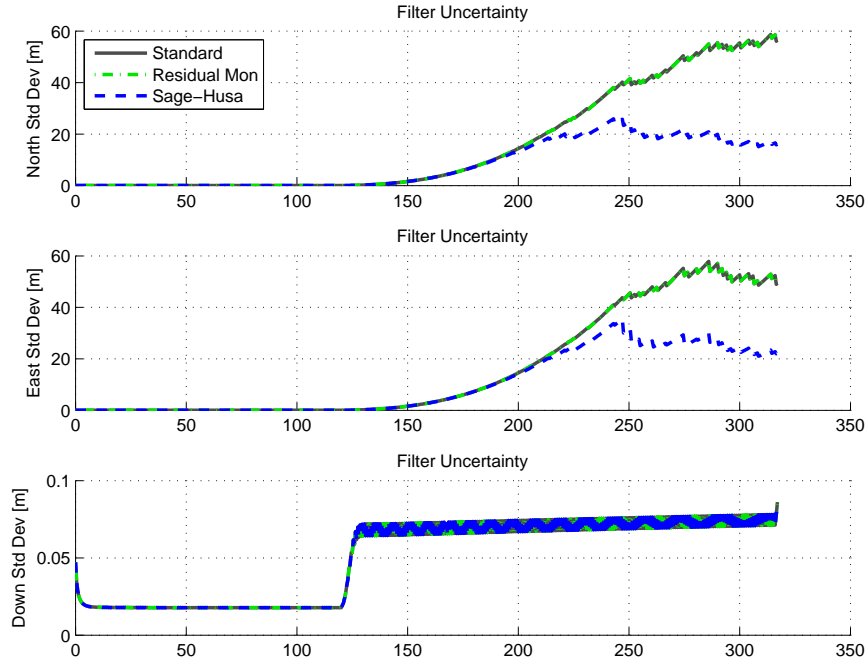
Figure 4.28: Filter Position States Uncertainty Comparison for Indoor Moving Data Set "North-South 1a." Notice that the filter uncertainty for the *north* and *east* axes is similar for each set of algorithms.

Analysis of the filter uncertainty for each of the NS data sets reveals the radio geometry does not strongly effect the Kalman filter uncertainty in the position states for the NS data sets. The large range uncertainty and short length of the trajectory minimizes the effect of poor geometry. Figure 4.28 presents the filter uncertainty for indoor moving data set "North-South 1a." The filter uncertainty for the horizontal *north* and *east* axes show similar uncertainties for each set of algorithms.

4.3.1.2 SQR Data Sets. Figure 4.29 contains results for the SQR group of indoor moving data collections. The effects of residual monitoring and the Sage-Husa adaptive algorithm on the SQR moving data sets are discussed in this section.

Large trajectory drift is noted in all four of the SQR data sets. The combination of attitude errors present for the initial filter alignment, the increased length of the SQR data collections as compared with the NS data sets, and increased RF inter-

107

(a) Square 1

(b) Square 2

(c) Square 3

(d) Square 4

Figure 4.29:   Residual Monitoring and Sage-Husa Horizontal Trajectory Comparison for Square Data Sets. Residual monitoring provides some drift constrai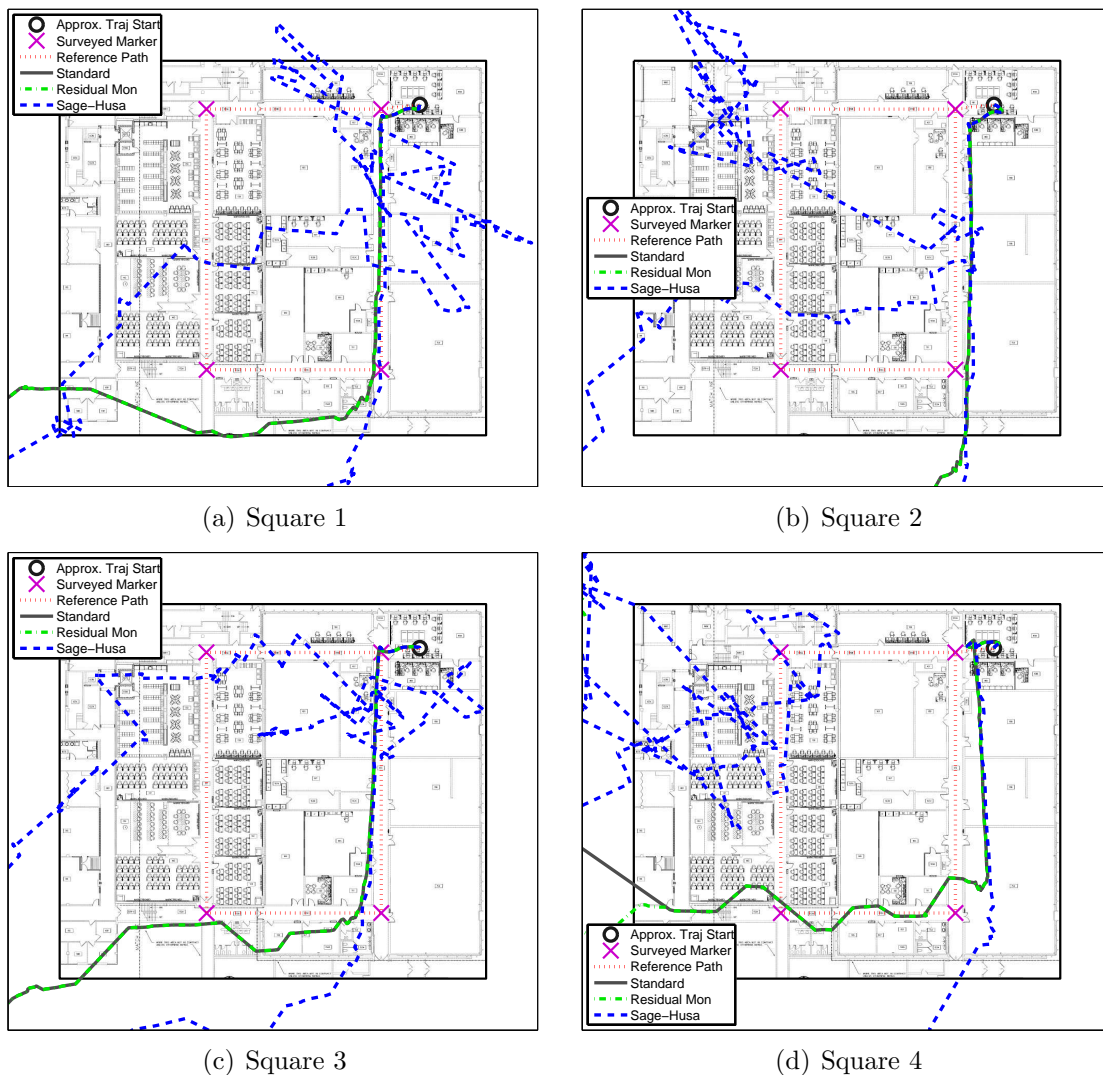nt in Figure 4.29 (d), but does not affect the remaining data sets due to the high range model uncertainty. Sage-Husa provides significant drift constraint, allowing range measurements with low RF interference to more strongly correct the filter position estimate.

ference all contribute to the trajectory drift. The increase in RF interference comes from the additional layers of building wall and doors which come between the DH500 radios as the navigation system moves along the reference path.

Residual monitoring has a notable effect on Figure 4.29 (d). Several of the range residual exceed the 3-σ threshold and are rejected. This results in a temporary reduction in trajectory drift. However, the residual monitoring trajectory in Figure 4.29 (d) still drifts significantly. Residual monitoring does not affect the trajectory drift in Figures 4.29 (a), 4.29 (b), and 4.29 (c) due to the range residual not exceeding the 3-σ threshold.

The Sage-Husa adaptive algorithm significantly reduces the trajectory drift for all four of the SQR data sets. As the RF interference increases during the middle portion of the trajectory, Sage-Husa increases range model uncertainty, causing the EKF to significantly reduce the weight placed on these high RF interference range measurements. This reduces the position error contributed by the range measurements. Towards the end of the trajectory, as RF interference decreases, the Sage-Husa estimate of the range model uncertainty also decreases. This allows the range measurements with lower RF interference to more strongly update the filter position estimate, helping to reduce the trajectory drift.

Figure 4.30 presents the Sage-Husa analysis for indoor moving data collection "Square 3" as shown in Figure 4.29 (c). Note how the filter uncertainty, or measurement noise variance, increases as the RF interference increases. Also note how the range bias, or measurement noise mean, tracks with the positive mean of the range bias. This estimated bias is subtracted from the range residual before updating the EKF position states. The Sage-Husa adaptive algorithm significantly reduces the trajectory drift providing a more accurate position estimate.

The longer and more complex "Square" trajectory introduces more variation to the Kalman filter position uncertainty. Figure 4.31 presents the Kalman filter position uncertainty for the "Square 1" data set. For the standard and residual monitoring

109

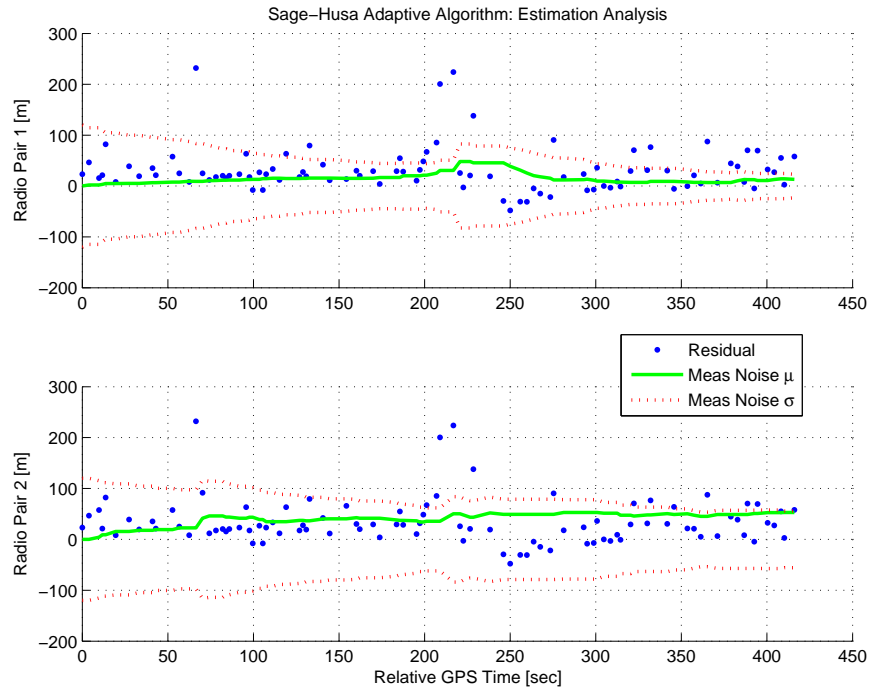Figure 4.30: Sage-Husa Estimate Analysis for Data Collection "Square 3." The range model uncertainty estimate, measurement noise variance, reduces the effect of very poor range measurements through the increase of the model uncertainty. Less RF interference is present towards the end of the trajectory and the significant reduction in model uncertainty allows these range measurements to strongly constrain the trajectory drift.
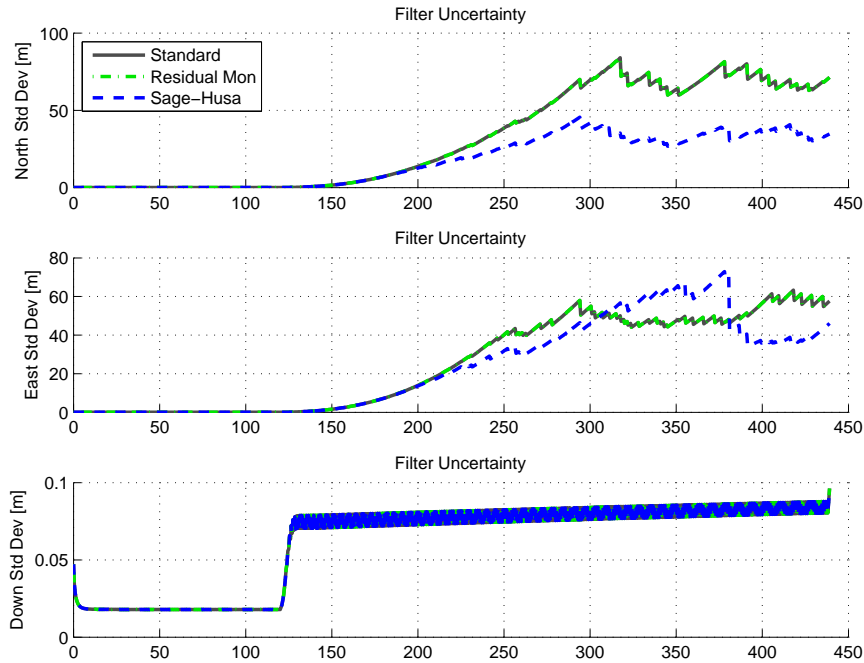
Figure 4.31:   Filter Position States Uncertainty Comparison for Indoor Moving Data Set "Square 1." Notice that the filter uncertainty for the *north* and *east* axes varies based on the algorithms employed. The *north* axis uncertainty is larger than the *east* axis for residual monitoring and the standard algorithm.

algorithms, the *north* axis uncertainty is generally larger that the respective *east* axis. The geometry of the radio positions is a primary source of this difference. Spacing the outdoor radios further apart, placing the northern base station further north and the southern base station further south, would improve the geometry when the indoor sensor suite moves furthest away from the outdoor radios. Notice also that addition of the Sage-Husa algorithm significantly changes the Kalman filter position uncertainties for the *north* and *east* axes. With the Sage-Husa algorithm, the range residual covariance value is more dependent on the current uncertainty of the incoming range measurements than the radio system geometry.

The results presented for both the NS group and SQR group contain significant trajectory error when compared to their respective reference paths. The INS drift is constrained with the range measurements and Sage-Husa adaptive algorithm, but precision navigation within the building is not possible with the remaining trajectory

drift. Results and analysis using imagery from the stereo camera system are presented in the next section.

4.3.2   Stereo Image Aiding.   Image-aiding provides position, velocity and attitude information based on image features tracked within view of the stereo camera system. This section presents post-processed results with the addition of image-aiding to the EKF setup. Each of the eight indoor moving data sets is post-processed with INS data, bias estimation, 2-minute stationary alignment data, vertical channel constraint data, range measurements, and stereo-camera imagery. The Sage-Husa algorithm is also included in the EKF radio range model due to the additional trajectory drift reduction afforded by its estimation of the range bias and model uncertainty.

The EKF post-processing setup contains three parameters that tune the image-aiding algorithm. The minimum feature scale is set to zero to accept all available image features found by the camera system. To increase the efficiency of the EKF algorithm, the maximum number of tracked image features is limited to 10. Image features are dropped when the tracked feature moves out of the camera's view. The number of additional features added to fill empty tracking slots is set to five to reduce the image feature turn-over rate of the image-aiding algorithm. Reducing this turn-over rate provides more stable feature tracking which helps improve the position, velocity, and attitude updates generated by the image-aiding system.

Section 4.3.2.1 contains observations and analysis for the NS data sets. Results and observations for the SQR data set are presented in Section 4.3.2.2.

4.3.2.1   NS Data Sets.   Figure 4.32 presents results for the NS group of the indoor moving data collections. Analysis and observations for the addition of image-aiding from the stereo camera system are presented next.

The addition of image-aiding to EKF post-processing produces a variety of results. Figures 4.32 (a) and 4.32 (d) show the addition of further drift to the post-processed trajectory. The poor availablity of features present in the building hallway

112

(a) North-South 1a

(b) North-South 1b

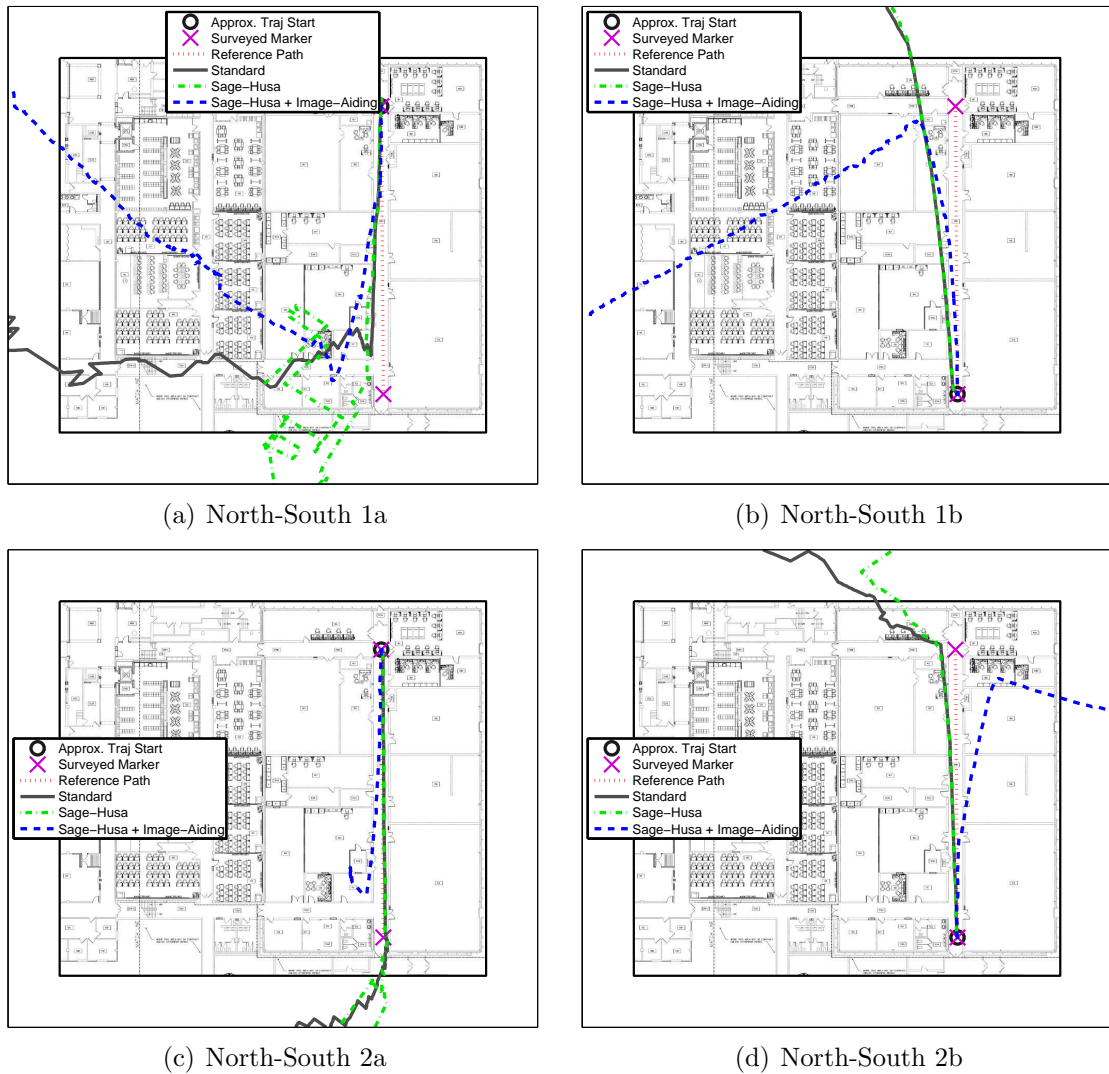(c) North-South 2a

(d) North-South 2b

Figure 4.32:   Image-Aiding Horizontal Trajectory Comparison for North-South data sets. The addition of image-aiding provides additional variety in both the reduction of and addition to existing trajectory drift. The sparse, flat hallways provide a minimal number of image features for the image-aiding system to track resulting in overall poor performance.

contribute significantly to the increase in drift. Sometimes the image-aided system is able to lock-on the the available features and provide filter updates as is evident in the reduction of drift shown in Figures 4.32 (b) and 4.32 (c) and other times the system incorrectly tracks image features adding significant additional position error as shown in Figures 4.32 (a) and 4.32 (d).

Another source of image-aiding error is objects temporarily obstructing the camera's view of the hallway. Obstruction occurs when a person walks into the camera's view. This occurred to various degrees in each of the indoor data sets. Other obstructions may consist of the blockage of one or both cameras due to an obstacle in the hallway. Whenever a feature moves out of the camera's view or is blocked from the camera's view, the image-aiding system stops tracking the feature. Fewer tracked features results in reduced accuracy in the position, velocity, and attitude updates provided to the EKF by the image-aiding system.

4.3.2.2   SQR Data Sets.   Figure 4.33 displays the results for the SQR group of indoor moving data collections. The outcome of adding image-aiding to EKF post-processing is discussed in this section.

The SQR trajectory introduces 90° turns around the hallway corners into the reference path. After each corner is rounded, the navigation system is stationary for 10-15 seconds to let the image-aiding system observe the new hallway to find new features to track. As is presented in Figure 4.33 a wide variety of results are obtained.

The image-aiding system retains features that move out of the camera's view or are block from view for several seconds. This is done to facilitate smooth features tracking. When a hallway corner is rounded, the image-aiding system ends up dropping all existing tracked features. This process of dropping and reacquiring new features is a significant source of image-aiding error. Figures 4.33 (a), 4.33 (b), and 4.33 (c) present image-aided trajectories that display the effect of rounding a hallway corner, where the image-aiding system is unable to acquire good new features to track.

114

(a) Square 1

(b) Square 2

(c) Square 3
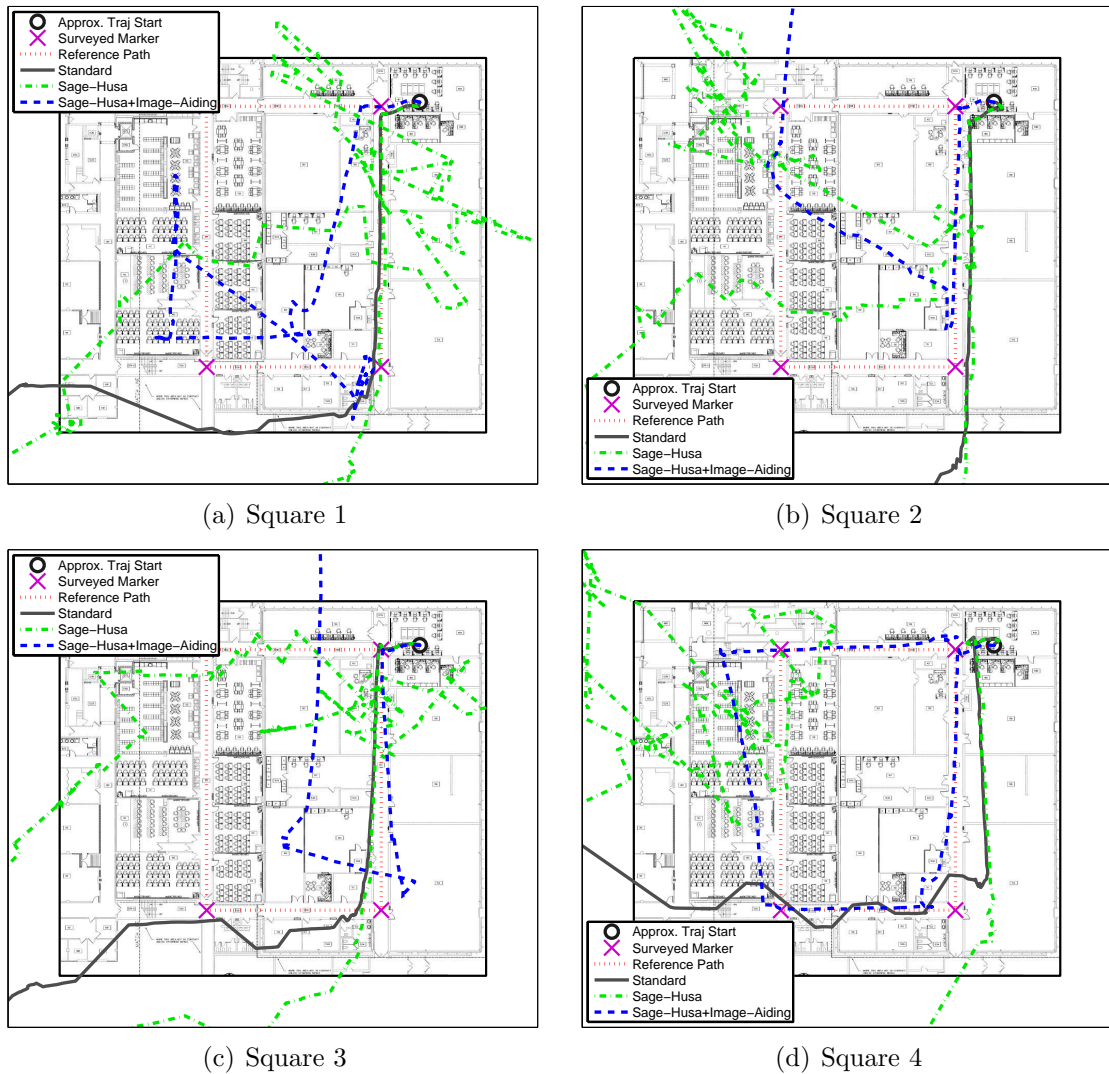
(d) Square 4

Figure 4.33:   Image-Aiding Horizontal Trajectory Comparison for the SQR Data Set. The results from image-aiding are varied. Rounding hallway corners during the trajectory present a significant source of image-aiding error. Camera view obstructions such as people and objects in the hallways cause further image-aiding errors which results in a reduction of trajectory drift.

The best image-aiding results obtained for this thesis are shown in Figure 4.33 (d). Several factors contributed to the significant trajectory drift constraint displayed in this plot. The image-aiding system was able to acquire and track sufficient image features to provide accurate position, velocity, and attitude updates to the EKF. Also, a lack of camera obstructions was present in this data set. Very few people blocked the camera's view during the entirety of the "Square 4" data collection.

Analysis of image-aiding performance for both the "North-South" and "Square" data sets without range measurements showed almost identical performance to the range and image-aided trajectories shown in Figures 4.32 and 4.33. This indicates the range measurements do not significantly effect the post-processed trajectory when the image-aiding system is enabled.

The results presented in this chapter for both the indoor and outdoor data collections display a wide variety of results. Constraint of trajectory drift is shown most clearly by the Sage-Husa adaptive method and selected image-aided data sets. The final evaluation of the algorithms and aiding techniques utilized in this navigation system are presented in the next chapter.

V. Conclusions and Future Work

This chapter presents the conclusions of this thesis and recommendations for future work. Section 5.1 presents an evaluation of the various algorithms and aiding techniques used in the navigation system. Improvements for the navigation system and recommendations for next steps in research are presented in Section 5.2. Section 5.3 contains the summary for this thesis.

5.1 Conclusions

Analysis of the navigation system began with characterization of the outdoor stationary radio performance presented in Section 4.1.1. As expected, the range error histograms displayed a very low number of outliers, which was due to very low RF interference. The predominant outdoor range error source was noise present in the radio ranging system. This noise was shown to be Gaussian. The average RMS range error of 8 meters was used for the first EKF radio range model uncertainty.

Next, the navigation system was tested by performing several outdoor, moving data collections. During filter tuning, the EKF range model uncertainty was adjusted to 55 meters. The results show the range measurements provide significant trajectory drift constraint. Position errors upwards of 1000 meters with INS-only navigation were reduced to 25-50 meters when the range measurements were applied along with filter bias estimation. In-depth results are presented in Section 4.2.

Residual monitoring was added to the EKF range update algorithm to help improve the drift constraint provided by the range measurements. The results in Section 4.2.4 showed this algorithm improved the average RMS trajectory error by 5 meters for data sets with large range outliers.

The Sage-Husa adaptive algorithm was tested next, with results also contained in Section 4.2.4. After tuning, the Sage-Husa algorithm was shown to provide an additional 0.5 to 2 meters reduction in the average trajectory error for each data collection.

The navigation system was then moved indoors to test the range drift constraint capability in an environment with high RF interference . A stationary range performance characterization was performed for the indoor setup. The range error histograms, presented in Section 4.1.2, show significant range error from the RF interference. The average RMS error of 63 meters is used to set EKF range model uncertainty for the indoor, moving data collections.

The navigation system was then tested by performing several indoor, moving data collections. The results are presented in Section 4.3. During the moving data collects, RF interference changes. This results in a large variation in the range error. The range model uncertainty was adjusted to 120 meters to account for this variation. The radio range measurements provided trajectory drift constraint, but at a reduced level. This was expected because of the increased RF interference.

Next, the Sage-Husa adaptive algorithm was tested on the indoor, moving data sets, with results presented in Section 4.3.1. After tuning Sage-Husa for the indoor data sets, decreases in trajectory drift upwards of 100 meters were observed.

Finally, the image-aiding system was incorporated into the previous set of sensors. When the image-aiding system found good features, the trajectory constraint between 3 to 12 meters was observed. In-depth results are presented in Section 4.3.2.

Overall, the radio range measurements constrained the inertial sensor drift. The addition of Sage-Husa provided further reduction in trajectory error. The image-aiding system showed the strongest drift constraint performance when good image features were found. The next section discusses areas of future work to further improve the navigation system presented in this thesis.

5.2 Future Work

This section discusses four areas of future work which would provide further advancement of the navigation capability presented in this thesis. The first area is the estimation of errors due to RF interference. A strong potential source of RF

interference for the DH500 radio system is RF multipath. There exist in $[2, 3, 7, 12]$ several scatter models and algorithms to account for multipath effects. The results contained in $[2,3]$ show the scatterer models to be robust in several different scatterer environment models providing notable reduction in multipath position error. These multipath estimators were not implemented in this thesis due to time constraints.

The second area is implementation of a real baro-altimeter. The simulated baro-altimeter used in this thesis to constrain the vertical navigation drift required GPS or surveyed markers. The choice to simulate the baro-altimeter data was made to simplify the navigation system to focus on implementation of the radio ranging system. A real baro-altimeter would permit the navigation system to estimate the altitude regardless of the environment. Tracking altitude changes between building floors is just one example of the expanded flexibility a real baro-altimeter would provide.

The third area of further research is implementation of an unscented Kalman filter instead of the EKF. Implementation of the unscented Kalman filter would not require linearization of the vehicle and sensor model as is required for the EKF. The linearization process removes non-linearities in the vehicle and sensor which introduces model error into the filter. Direct implementation of the non-linear models allows the unscented Kalman filter to provide a more accurate estimate of the system states.

Fourth, the Sage-Husa adaptive algorithm showed significant promise in trajectory drift reduction. However, the dual memory factor tuning performed in this thesis to accommodate the low and high RF interference environments requires the user to switch between factors depending on the environment. This can be improved by determining a single Sage-Husa memory factor that provides drift reduction for both the outdoor and indoor environments.

5.3 Closing

The navigation system developed in this thesis has been shown to provide notable INS drift constraint through the use of the DH500 radio system. The addition of the Sage-Husa adaptive algorithm and image-aiding system provided additional sources of drift constraint. Shown to work in environments with both high and low RF interference, this research presents a viable navigation system that enables precision navigation for the warfighter in GPS-denied environments.

Bibliography

1. *Department Of Defense World Geodetic System 1984: Its Definition And Relationships With Local Geodetic Systems*. Technical report, National Imagery And Mapping Agency, January 2004.

2. Al-Jazzar, S. and Jr. Caffery, J. "ML And Bayesian TOA Location Estimators For NLOS Environments". *Vehicular Technology Conference, 2002. Proceedings. VTC 2002-Fall. 2002 IEEE 56th*, volume 2, 1178 – 1181. 2002. ISSN 1090-3038.

3. Al-Jazzar, S., Jr. Caffery, J., and H.-R. You. "A Scattering Model Based Approach To NLOS Mitigation In TOA Location Systems". *Vehicular Technology Conference, 2002. VTC Spring 2002. IEEE 55th*, volume 2, 861 – 865. 2002.

4. Amendolare, V., D. Cyganski, R.J. Duckworth, S. Makarov, J. Coyne, H. Daempfling, and B. Woodacre. "WPI Precision Personnel Locator System: Inertial Navigation Supplementation". *Position, Location and Navigation Symposium, 2008 IEEE/ION*, 350 –357. 5-8 2008.

5. Amendolare, V., D. Cyganski, R.J. Duckworth, S. Makarov, J. Coyne, H. Daempfling, B. Woodacre, W. Michalson, J. Orr, S. Kulkarni, and H. Parikh. "WPI Precision Personnel Locator System - Indoor Location Demonstrations and RF Design Improvements". *ION-AM Conference*. April 2007.

6. Amendolare, V., D. Cyganski, R.J. Duckworth, S. Makarov, Michalson W., J. Orr, J. Coyne, J. Daempfling, H. Farmer, D. Holl, S. Kulkarni, H. Parikh, and B. Woodacre. "WPI Precision Personnel Locator System". *ION-NTM: Urban And Indoor Navigation Technology*, 350 –357. January 2007.

7. Chen, Bor-Sen, Chang-Yi Yang, Feng-Ko Liao, and Jung-Feng Liao. "Mobile Location Estimator In A Rough Wireless Environment Using Extended Kalman-Based IMM And Data Fusion". *Vehicular Technology, IEEE Transactions On*, 58(3):1157 –1169, March 2009. ISSN 0018-9545.

8. Ernsberger, Maj. Patric J. *Performance Enhacements of Ranging Radio Aided Navigation*. Master's Thesis, Air Force Institude Of Technology, March 2009.

9. Fisher, Capt Kenneth. *The Navigation Potential Of Signals Of Opportunity-Based Time Difference Of Arrival Measurements*. Ph.D. Dissertation, Air Force Institute Of Technology, May 2005.

10. Fontana, R.J., E. Richley, and J. Barney. "Commercialization Of An Ultra Wideband Precision Asset Location System". *Ultra Wideband Systems And Technologies, 2003 IEEE Conference On*, 369 – 373. November 2003.

11. Kim, J. and S. Sukkarieh. "A Baro-Altimeter Augmented INS/GPS Navigation System For An Uninhabited Aerial Vehicle". *International Symposium On Satellite Navigation Technology*. SATNAV, July 2003.

12. Le, Bao Long, K. Ahmed, and H. Tsuji. "Mobile Location Estimator With NLOS Mitigation Using Kalman Filtering". *Wireless Communications And Networking, 2003. WCNC 2003. 2003 IEEE*, volume 3, 1969 –1973. 20-20 2003. ISSN 1525-3511.

13. Leon-Carcia, Alberto. *Probability, Statistics, And Random Processes For Electrical Engineering*. Pearson Prentice Hall, 3rd edition, 2008.

14. Liu, Hui, H. Darabi, P. Banerjee, and Jing Liu. "Survey Of Wireless Indoor Positioning Techniques And Systems". *Systems, Man, And Cybernetics, Part C: Applications And Reviews, IEEE Transactions On*, 37(6):1067 –1080, November 2007. ISSN 1094-6977.

15. Maybeck, Peter S. *Stochastic Models, Estimation And Control*, volume 2. Academic Press, 1982.

16. Maybeck, Peter S. *Stochastic Models, Estimation, And Control*, volume 1. Navtech Book And Software Store, 1994.

17. Moghaddamjoo, A. and R.L. Kirlin. "Robust Adaptive Kalman Filtering With Unknown Inputs". *Acoustics, Speech And Signal Processing, IEEE Transactions On*, 37(8):1166 –1175, August 1989. ISSN 0096-3518.

18. Novatel. *SPAN-SE User Manual*, rev 5 edition.

19. NovAtel. *Honeywell HG1700 Datasheet*. NovAtel Inc., 2010. URL `novatel.com`.

20. Qi, Honghui and J.B. Moore. "Direct Kalman Filtering Approach For GPS/INS Integration". *Aerospace And Electronic Systems, IEEE Transactions On*, 38(2):687 –693, April 2002. ISSN 0018-9251.

21. Qi, Yihong, H. Suda, and H. Kobayashi. "On Time-Of-Arrival Positioning In A Multipath Environment". volume 5, 3540 – 3544. September 2004. ISSN 1090-3038.

22. Sage, Andrew P. and Gary W. Husa. "Algorithms For Sequential Adaptive Estimation Of Prior Statistics". *Adaptive Processes (8th) Decision And Control, 1969 IEEE Symposium On*, volume 8, 61. November 1969.

23. Schwartz, Gen. Norton. "Opening Keynote Address". *38th IFPA-Fletch Conference On National Security Strategy And Policy*, 19. January 2010.

24. Tanigawa, M., H. Luinge, L. Schipper, and P. Slycke. "Drift-Free Dynamic Height Sensor Using MEMS IMU Aided By MEMS Pressure Sensor". 191 –196. March 2008.

25. Titterton, David and John Weston. *Strapdown Inertial Navigation Technology*. Institute Of Electrical Engineers, 2004.

26. Veth, Lt Col Michael. *Fusion of Imagery And Inertial Sensors For Navigation*. Ph.D. Dissertation, Air Force Institute Of Technology, September 2006.

27. Wylie, M.P. and J. Holtzman. "The non-line of sight problem in mobile location estimation". *Universal Personal Communications, 1996. Record., 1996 5th IEEE International Conference on*, volume 2, 827 –831 vol.2. 29 1996.

28. Zhao, Lin, Chen Huang, Xinzhe Wang, and Zhonghua Su. "Research On Satellite Attitude Determination With Adaptive Filter". *Information And Automation (ICIA), 2010 IEEE International Conference On*, 1045 –1048. June 2010.

REPORT DOCUMENTATION PAGE

1. REPORT DATE *(DD–MM–YYYY)*	2. REPORT TYPE	3. DATES COVERED *(From — To)*
24–03–2011	Master's Thesis	Sept 2009 — Mar 2011

4. TITLE AND SUBTITLE

Non-GPS Navigation Using Vision-Aiding
and
Active Radio Range Measurements

5a. CONTRACT NUMBER

5b. GRANT NUMBER

5c. PROGRAM ELEMENT NUMBER

6. AUTHOR(S)

Erich Lichtfuss, 2d Lt, USAF

5d. PROJECT NUMBER

JON 11-702

5e. TASK NUMBER

5f. WORK UNIT NUMBER

7. PERFORMING ORGANIZATION NAME(S) AND ADDRESS(ES)

Air Force Institute of Technology
Graduate School of Engineering and Management (AFIT/EN)
2950 Hobson Way
WPAFB OH 45433-7765

8. PERFORMING ORGANIZATION REPORT NUMBER

AFIT/GE/ENG/11-23

9. SPONSORING / MONITORING AGENCY NAME(S) AND ADDRESS(ES)

Raytheon (De Mai)
1801 Hughes Drive
Fullerton, CA 92834
(714–446–3140; de.mai@raytheon.com)

10. SPONSOR/MONITOR'S ACRONYM(S)

Raytheon

11. SPONSOR/MONITOR'S REPORT NUMBER(S)

12. DISTRIBUTION / AVAILABILITY STATEMENT

13. SUPPLEMENTARY NOTES

14. ABSTRACT

The military depends on the Global Positioning System (GPS) for a wide array of advanced weaponry guidance and precision navigation systems. Lack of GPS access makes precision navigation very difficult. Inclusion of inertial sensors in existing navigation systems provides short-term precision navigation, but drifts significantly over long-term navigation. This thesis is motivated by the need for inertial sensor drift-constraint in degraded and denied GPS environments. The navigation system developed consists of inertial sensors, a simulated barometer, three Raytheon DH500 radios, and a stereo-camera image-aiding system. The Raytheon DH500 is a combat comm radio which also provides range measurements between radios. The measurements from each sensor are fused together with an extended Kalman filter to estimate the navigation trajectory. Residual monitoring and the Sage-Husa adaptive algorithm are individually tested in the Kalman filter range update algorithm to help improve the radio range positioning performance. The navigation system is shown to provide long-term inertial sensor drift-constraint with position errors as low as 3 meters.

15. SUBJECT TERMS

radio ranging, vision-aiding, non-GPS precision navigation, extended Kalman filter, adaptive Kalman filter

16. SECURITY CLASSIFICATION OF:			17. LIMITATION OF ABSTRACT	18. NUMBER OF PAGES	19a. NAME OF RESPONSIBLE PERSON
a. REPORT	b. ABSTRACT	c. THIS PAGE			Michael Veth, Lt Col, USAF (ENG)
U	U	U	UU	142	**19b. TELEPHONE NUMBER** *(include area code)* (850) 882–4667; Michael.Veth@eglin.af.edu